THE UNIVERSITY *of* EDINBURGH

Using Models of the Earth's Atmosphere to Assess Exoplanet Habitability

Jack S. Yates

Thesis submitted for the degree of Doctor of Philosophy

School of GeoSciences

The University of Edinburgh

2018

Author's Declaration

I declare that this thesis has been composed solely by myself and that it has not been submitted, either in whole or in part, in any previous application for a degree. Except where otherwise acknowledged, the work presented is entirely my own.

Jack Yates

2018

Abstract

Recent advances in telescope technology have allowed us to detect planets and bodies that have the potential to be habitable. Habitability can be defined in a number of ways, but most commonly it is defined by the availability of liquid water. There are a vast number of factors that determine whether or not liquid water is present in an atmosphere or on a surface, and due to the limited observational data, our understanding of the role of each of these factors is poor, especially as we move further through the parameter space away from the Earth.

Until data from the next generation of telescopes are available, attempts to constrain atmospheric habitability have to utilise computer modelling. Modelling has a long history in habitability studies, particularly with regards to the inner and outer boundaries of the circumstellar habitable zone (CHZ). Early models were 1-dimensional (1D), but in the last decade the balance has shifted towards 3-dimensional (3D) global circulation models (GCMs) that describe the air flow in a planetary atmosphere in a much more sophisticated way. In part this was due to the recognition of the importance of 3D processes like clouds and convection in the global energy balance, and in part due to the increasing prioritisation of planets that are dissimilar to Earth, such as M-dwarf planets, which show features such as tidal-locking and atmospheric jets that result in less spatial uniformity through the atmosphere, limiting the applicability of 1D models.

As of this writing our current best hopes for habitability are M-dwarf planets such as the TRAPPIST planets and Proxima Centauri b that orbit in the habitable zone, with rocky compositions. M-dwarf planets were previously overlooked as candidate habitable planets in favour of G-star planets like the Earth. However, some researchers now favour M-dwarfs in light of modern GCM results, observational biases and planetary population statistics, demonstrating that we must be careful not to define habitability in a way that is too Earth-centric.

In this thesis we expand on knowledge of habitability through models that are informed by Earth science, but that do not necessarily describe Earth-like environments. In Chapter 2, we consider an environment that has not been studied through the lens of habitability before: ultra-cool Y dwarf atmospheres. In the atmospheres of these bodies it is thought that there may be liquid water clouds and temperatures and pressures similar to those on the Earth's surface. However, as there is no surface it is important that any potential organisms are able to remain above the hot lower atmosphere and

the cold upper atmosphere; we compare with the Earth's atmosphere, where microbes are able to stay in the atmosphere for weeks, even metabolising in clouds. We study this environment through a simple radiative or convective atmosphere paired with a model informed by nutrient-phytoplankton-zooplankton models from the Earth's ocean. We find that organisms similar in size to microbes can remain aloft in this environment due to upward convective winds.

In Chapter 3, contrasting with the simple approach in the previous chapter, we describe the development of a highly-sophisticated, fully online, 3D photochemical model of an exoplanet atmosphere. We apply this model to a tidally-locked M-dwarf aqua planet with an Earth-like atmosphere, nominally Proxima Centauri b, to evaluate the impacts of the differing stellar energy spectrum and dramatically different global circulation on an ozone layer described through the Chapman mechanism and the hydrogen oxide catalytic cycle. We find that the ozone layer is unlike that seen in the Earth's atmosphere. The lack of UV photons from our quiescent M-dwarf results in very long chemical lifetimes, which means that the atmospheric transport becomes the dominant factor in the structure of the ozone layer. We see an accumulation of ozone in the night-side cold traps (or gyres) at low altitudes where transport is slow and lifetimes are long, resulting in a dramatic day-night contrast in ozone columns. Total ozone column is much smaller on an M-dwarf planet compared with the Earth, by around a factor of 10, owing to top-of-atmosphere UV flux.

In Chapter 4, we develop on the results of Chapter 3 by altering certain parameters in the model and examining the effect on the climate. We find that dramatic changes occur when switching off the chemistry scheme and reverting to a prescribed Earth ozone layer. Specifically we find that the temperatures on the night side of the planet change by more than 50 K, accompanied by dramatic changes in the pole temperatures. In addition the cold traps move towards the equator and eastwards. These changes are caused by the smaller ozone columns that result from the interactive chemistry, which severely reduce night side atmosphere opacity. This opacity controls the night side cooling rate which in turn controls the atmospheric circulation through the day-to-night temperature contrast. We find that similar effects occur when switching off the hydrogen oxide catalytic loss cycle, though to a lesser extent.

Furthermore, we examine the effects of electromagnetic flares on the chemistry, which do not seem to impact ozone columns, in agreement with previous works. Finally we demonstrate the changes in atmospheric ozone and climate in a 3:2 resonant orbit and with an Earth-like orbit and top-of-atmosphere flux. In sum, our results with this model show that the climate is highly sensitive to the ozone columns, and demonstrate the importance of fully-coupled 3D photochemical models, which have been used very rarely in exoplanet atmosphere modelling.

Lay summary

When observing the Earth from space, it is immediately obvious that it has both liquid water and life. The two are thought to be connected; experiments and theory suggest that life cannot occur without water. Within the the Solar System, only Earth is at the right distance from the Sun to have oceans on its surface. The other planets are all either too close and hot or too far away and cold.

For all of human history we have been incapable of determining whether or not there is liquid water and/or life outside of the Solar System. Improvements in telescope technology over the last few years have allowed us to detect planets that seem to receive similar amounts of heat from their stars as Earth, meaning that they could have liquid water at their surfaces and therefore at least some possibility of life. However, we know next to nothing about these planets because we can only measure their most basic parameters, such as their overall size, which means that it is extremely difficult to determine whether or not they could have liquid water. In the coming decade, further technological advances should allow us to measure properties such as the planet's atmospheric composition, which will give us a much clearer picture of whether or not there are other planets with water and life.

In the mean time, to attempt to gain some understanding of these planets, we run computer simulations of planetary atmospheres covering the entire range of possibilities of atmospheric composition, planetary size, amount of heating from the star, the length of the planet's day, the amount of water on the surface, the properties of the star and a host of other factors, feeding into the simulations the small amount of information that is currently available. These simulations help to clarify when and where life might be possible and when and where we might be able to detect it.

In this thesis I have applied theories and observations from the Earth to try to estimate whether or not we might find life outside of the Solar System, with a particular focus on computer simulations of atmospheres. In Chapter 2, I apply theories that describe the populations of plankton in the ocean to ultra-cool brown dwarf atmospheres. Brown dwarfs are similar to planets but larger, and more similar to Jupiter than Earth. In the atmospheres of these cool brown dwarfs there are thought to be liquid water clouds, and atmospheric temperatures and pressures are similar to those at the Earth's surface. These atmospheres look like they could support life; however, there is no planetary surface, which presents a challenge for any organisms that might

live in these atmospheres – at low altitudes the atmosphere is too hot and at high altitudes the atmosphere is too cold, meaning that organisms must place themselves in the temperate region in between. In the Earth's oceans, plankton populations behave similarly; they float up and down towards the ocean surface, depending on their size. I use a simple model of the brown dwarf atmosphere coupled with this plankton description to show that small organisms similar to microbes could maintain a population in the temperate region of the brown dwarf atmosphere.

In Chapter 3, I develop a much more sophisticated computer model of an Earth-like planet's atmosphere to understand how ozone behaves under differing orbital conditions. Earth's ozone layer is what protects the surface from extremely high levels of ultraviolet radiation; without it humans would almost certainly not be here. Furthermore, the behaviour of atmospheric ozone has major impacts on the planetary climate, affecting temperatures and therefore liquid water. This model represents one of the most complex atmospheric chemistry simulations of a planet outside of the solar system so far.

I use this model to show that a planet orbiting a much closer to a star that is much cooler than the Sun can still have an ozone layer, despite significant changes in the radiation from the star. Furthermore, when the planet is so close to the star, its day-night rotation can synchronise to the planetary orbit, resulting in a permanent night side that never faces the star. The model shows that in this scenario the ozone layer is very different between the day and night sides, with ozone accumulating on the night side of the planet, which has important implications for the surface temperatures on the planet and future telescope observations that attempt to detect ozone. The model suggests that a planet similar to the simulated one could have liquid water.

Finally in Chapter 4 I use the same atmospheric chemistry model to investigate how changes in the planetary parameters affect the ozone layer and how the complexity of the atmospheric chemistry affects the model results. My results indicate that previous simulations may have underestimated the importance of atmospheric chemistry, as small changes in the atmospheric composition seem to have disproportionately large effects on the planetary atmosphere and surface. I also show that short-term increases in radiation from the star have minimal impact on atmospheric ozone and finally I show that changing the planet's orbit to a non-synchronised rotation results in changes in the atmospheric ozone layer and a warmer surface, and simulate a planet more similar to Earth to clarify the differences between planets that orbit Sun-like stars and cold stars.

Contents

List of Figures

List of Tables

CHAPTER 1

Introduction

1.1 Exoplanets

1.1.1 Brief history of exoplanets

The search for life beyond Earth has taken a new direction in the last few years. In addition to the search for life within the solar system and the search for extraterrestrial intelligence which have been ongoing for decades, we are now detecting Earth-sized extrasolar planets (exoplanets) that receive a similar amount of stellar irradiation to the Earth. This places them in the circumstellar habitable zone (CHZ), the region where liquid water may be present on the planetary surface (Kasting, 1988; Kasting et al., 1993). These exoplanets may represent the best prospects to date for life beyond Earth.

The journey to the detection of these planets has been a short one in scientific terms. The first confirmed exoplanets were discovered in the early nineties by Wolszczan and Frail (1992), by the detection of irregularities in the timing of pulsar pulses. The first detections of planets around main-sequence stars came in 1995 (Mayor and Queloz, 1995). In the 2000s, automated surveys revolutionised the field, yielding vast quantities of planet detections, typified by the Kepler mission (a recent review provided in Borucki, 2016). To date thousands of exoplanets have been discovered (e.g. Morton et al., 2016; Thompson et al., 2018), with a broad range of properties. There are many systems that are radically different from our own solar system: planets on orbits only a few hours long (e.g. Charpinet et al., 2011); planetary systems that are extremely compact, such as Kepler-11, with 6 planets at orbital separations smaller than that of Mercury (Lissauer et al., 2011); circumbinary planets with two stars (Welsh and Orosz, 2017).

Beyond basic orbital parameters, improvements in telescope and detector technology have made characterisation of (giant) exoplanets through transmission and emission spectroscopy and direct imaging a reality. The first detection of an exoplanet atmosphere was achieved with transmission spectroscopy by Charbonneau et al. (2002), who detected the absorption by the sodium doublet in the atmosphere of the planet HD 209458b. Some of the most impressive detections of exoplanet atmospheres are catalogued in Burrows (2014) and Seager (2014).

Characterisation of small exoplanets is not possible with current instrumentation. However, our capability to characterise exoplanets is set to increase in the coming decade as new instruments come online. At the time of this writing, we are on the cusp of being able to characterise some habitable planets, with the upcoming launch of the James Webb Space Telescope and other space telescopes built for exoplanet characterisation and the construction of the next generation of extremely large ground-based telescopes (see Kaltenegger, 2017; Fujii et al., 2018, for review of characterisation

prospects, with a focus on habitability). Our understanding of exoplanet formation, atmospheric compositions and planetary science will likely change rapidly as the first results are returned from these instruments.

1.1.2 Habitability of exoplanets

Amongst such a broad spectrum of planets, we search preferentially for those that are deemed to be habitable, with a view to eventually determining whether or not there is life elsewhere in the galaxy. To look for a habitable planet, we must first identify what it is to be "habitable"; this requires speculation as to what extraterrestrial life might actually look like. We can extrapolate only from what we know about life on Earth and what we know about the laws of physics. Our expectations for the conditions necessary to develop or harbour life are therefore derived from observations on biochemistry and the limiting conditions for organisms on Earth. McKay (2014) lists four requirements for life:

1. the presence of liquid water,
2. the availability of energy,
3. the availability of carbon,
4. the availability of the elements hydrogen, nitrogen, oxygen, phosphorus, sulphur (known along with carbon as CHNOPS) – the most common elements in molecules important for Earth life.

From an astronomical perspective, availability of liquid water on a planet is the first one that we attempt to constrain with our limited observational information, giving rise to the concept of the 'circumstellar habitable zone' (CHZ), the region around a star within which a planet could potentially maintain some liquid water at its surface or within its atmosphere (Kasting, 1988; Kasting et al., 1993; Kaltenegger, 2017). A planet in the habitable zone does not necessarily have liquid water – only the *potential* for it.

Taking this conservative definition of planetary habitability – liquid water at the surface or in the atmosphere – there is a very large range of properties that can affect habitability within the bounds of the habitable zone. Figure 1.1 provides a summary of these. Fully describing the interaction of these parameters is an impossible task; the interplay is so complicated that we can only isolate and study a small number of parameters at a time.

Typically, exoplanet habitability in the context of liquid water has been assessed through atmospheric modelling (Schwieterman et al., 2018). With most of the factors

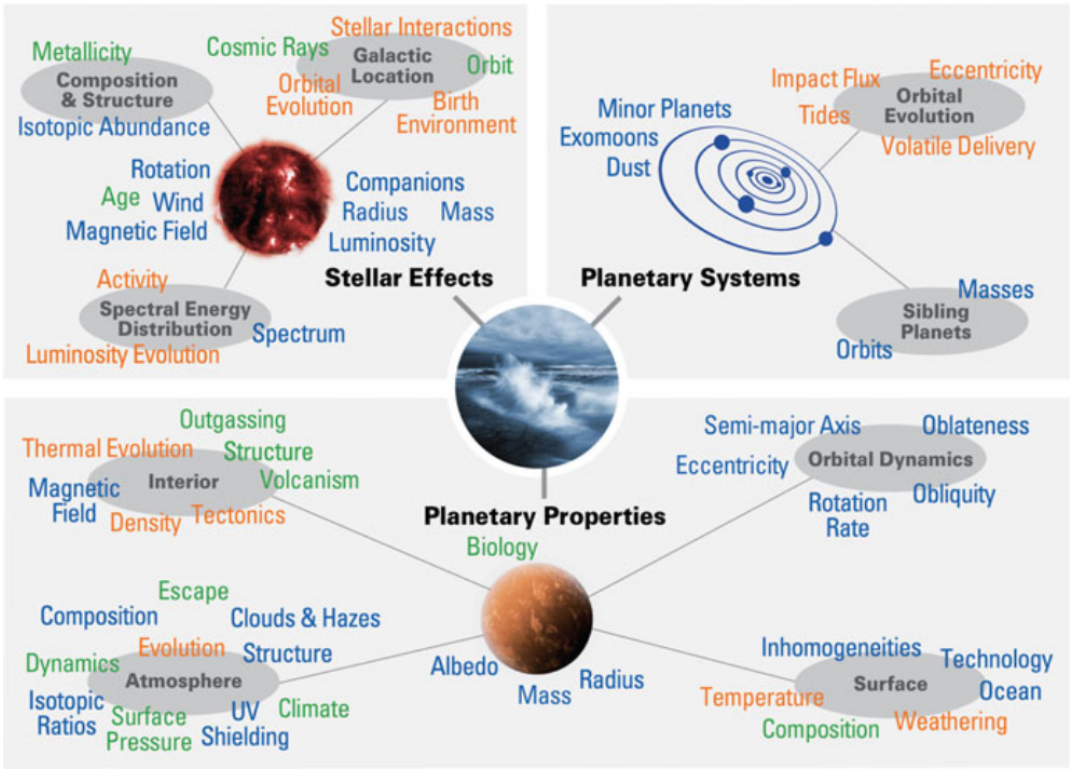

Figure 1.1: A summary of factors affecting planetary habitability. Blue and green text indicates factors that may one day be observed whilst orange denotes properties that can only be assessed through modelling. Taken from Meadows and Barnes (2018).

in Figure 1.1 being completely unknown for a typical planet, we generally focus on the interaction between the planetary atmosphere and the incoming stellar radiation. The nature of the planetary atmosphere is therefore critical for determination of planetary habitability (Seager, 2013).

However, even if this parameter space is pared down to only the factors affecting the planetary atmosphere, there are a great number of topics that are yet to be explored. Chemistry in particular is mostly ignored in atmospheric simulations in favour of static chemical compositions that represent maximum and minimum greenhouse effects in line with historical definitions such as those in Kasting et al. (1993). However, atmospheric chemistry impacts many of the factors that determine habitability – for example, the composition, dynamics, UV shielding and clouds and hazes. Each of these processes feeds back into the climate in complex ways that cannot always be parameterised. A chemically consistent model is needed to provide a physically realistic description of all of these processes at the same time.

There is a rich history of the assessment of exoplanet habitability through modelling of the boundaries of the circumstellar habitable zone. In the past, 1-dimensional models have been used (Schwieterman et al., 2018), but more recently the value of 3-dimension global circulation models has been recognised (e.g. Abe et al., 2011; Leconte et al., 2013; Yang et al., 2013; Yang et al., 2014; Godolt et al., 2015; Kaspi and Showman, 2015; Paradise and Menou, 2017; Wolf et al., 2017). These models are much more advanced than the 1D models used in the past, and are more capable of describing important 3D climatological process like clouds, precipitation and convection. However, the chemistry models used in exoplanet atmosphere simulations are still usually 1-dimensional, even if paired with 3D dynamics models (e.g. Segura et al., 2003; Zahnle et al., 2009; Hu et al., 2012; Miller-Ricci Kempton et al., 2012; Moses, 2014; Venot and Agúndez, 2015; Mendonça et al., 2018).

Recent detections of planets that appear to be in the habitable zone have necessitated simulations of specific habitable zone planets (e.g. simulations of Proxima Centauri b: Boutle et al., 2017; Turbet et al., 2017; Meadows et al., 2018). Perhaps the most evocative of the detected potentially habitable planets are those orbiting TRAPPIST 1 – a system of 7 planets, all approximately Earth sized, with 3 planets or more in the circumstellar habitable zone, orbiting so close together that they would appear larger than the Moon from the planetary surfaces (Gillon et al., 2017) – or Proxima Centauri b – an Earth-sized planet in the habitable zone of the nearest star to the Sun, only 1.3 pc away (Anglada-Escudé et al., 2016).

For planets with known properties the process of assessment of planetary habitability is different. Here, the inclusion of feedback mechanisms will alter the habitable zone for the specific composition in question. In these cases it is of

critical importance that the feedbacks are simulated accurately; a model with a fixed composition might imply the planet is habitable whereas a model with online chemistry spirals out of control due to feedbacks. Thus, to assess the habitability of a specific planet with a given composition we must use the most accurate simulations possible.

Liquid water may also exist outside of the CHZ. It is conceivable that there are 'atmospheric[1] habitable zones' with condensed liquid water in atmospheres above an inhabitable surface, or indeed no surface at all in the case of brown dwarfs or gas giants (Sagan and Salpeter, 1976; Cockell, 1999; Dartnell et al., 2015), or that life may exist in subsurface lakes or oceans (Fortes, 2000; Greenberg et al., 2000; Chyba and Phillips, 2001; Parkinson et al., 2008), such as those on Ganymede, Enceladus and Europa and perhaps other solar system bodies (Postberg et al., 2011; Schmidt et al., 2011; Vance et al., 2014; Saur et al., 2015; Thomas et al., 2016). It is also possible for an uninhabitable planet to host a habitable moon; a large moon like Titan orbiting a gas giant exoplanet in the habitable zone may also be habitable (Kaltenegger, 2017). No exomoons have been detected as of this writing, but instruments are reaching the (expected) required sensitivities (Heller, 2017).

Many alternative types of life have been proposed. This includes alternative biochemistries (for example, life that uses hydrocarbons in place of water and life that uses silicon in place of carbon) and alternative habitats (for example, the aforementioned subsurface oceans and gas giant atmospheres, planetary satellites or moons, bodies with liquid hydrocarbons such as Titan, Venus- or Mars-like planets, so-called 'Dune' planets and water planets) (see Irwin, 2018, and references therein).

1.1.3 Brown Dwarfs

Recent discoveries of extremely cool brown dwarfs, known as Y-dwarfs, present one such non-terrestrial environment where liquid water may be present (Morley et al., 2014b). Brown dwarfs are objects intermediate between stars and planets (Hayashi and Nakano, 1963; Kumar, 1963)[2]. Brown dwarfs have significant hydrogen/helium atmospheres and have masses between those of the giant gas planets ($\sim 13 M_{\rm J}$ according to the IAU definition) and about 75 $M_{\rm J}$[3], where hydrogen fusion begins. The line between brown dwarfs and large gas giants is not currently well-defined, and several methods have been proposed to distinguish between the two. One common definition is that objects that fuse deuterium (requiring masses greater than about 13 $M_{\rm J} \approx 4000\ M_\oplus$) are brown

[1] Or aerial.

[2] At this time they were known as black dwarfs.

[3] $M_{\rm J}$ is a Jupiter mass, with 1 $M_{\rm J} = 1.9 \times 10^{27}$ kg $\approx 320\ M_\oplus$, where $M_\oplus$ is an Earth mass or 6.0×10^{23} kg.

dwarfs, whilst smaller objects are called gas giants.

The first brown dwarfs (Teide 1 and GI 229B) were discovered in 1995 (Nakajima et al., 1995; Rebolo et al., 1996), although they were predicted to exist many years before this (see for example Hayashi and Nakano, 1963; Kumar, 1963). Improving technology has allowed us to detect colder and dimmer brown dwarfs, down to the Y dwarfs (described below) with infrared magnitudes[4] greater than 20 (Cushing et al., 2011; Kirkpatrick et al., 2012).

Many brown dwarfs are so-called 'free-floating' brown dwarfs (perhaps even more numerous than main-sequence stars; Clanton and Gaudi, 2016). Free-floating brown dwarfs are often easier to detect than companions to stars, as the signal from the brown dwarf is not washed out by an extremely bright star. Brown dwarfs cannot fuse hydrogen, so they gradually cool after formation (Kumar, 1963). They are classed by features in their spectra, by way of an extension of the OBAFGKM scale that is used for normal stars. There are four classes of brown dwarfs, which are (generally) decreasingly hot: class M (which also includes very small stars), class L, class T and class Y (Kirkpatrick et al., 1999; Cushing et al., 2011). Only a small number of Y dwarfs have been discovered, due to their inherent faintness (Cushing et al., 2011; Kirkpatrick et al., 2012). They are the coldest known brown dwarfs, and generally have temperatures below 500 K – some lower than 300 K (approximately room temperature on Earth) (Beamín et al., 2014; Faherty et al., 2014; Kopytova et al., 2014; Luhman, 2014) – and show evidence of water clouds in their atmospheres (Morley et al., 2014b).

[4]Magnitudes are an archaic astronomical measure of brightness. The scale is logarithmic with a difference of 5 magnitudes equating to a factor of 100 in brightness. Smaller (or more negative) magnitudes are brighter. Vega is usually used as a 0-point, thus the Sun has a magnitude of -27, Venus has a magnitude of -5, naked-eye stars have magnitudes up to 6 and Pluto has a magnitude of 14. The largest ground-based telescopes can detect objects up to 27 mag and Hubble can detect objects up to 32 mag.

1.2 Global circulation models

Global circulation models (GCMs) at their most fundamental are simulations of the movement of air in the atmosphere of a planet, essentially attempting to solve a set of thermodynamics and fluid mechanics equations over time. By and large these models use a uniform 3D grid extending between a lower and upper boundary (for example, the surface of a terrestrial planet might be a lower boundary), though there are also wave-based models (Silberman, 1954), non-rectangular grids (Sadourny et al., 1968) and models with nested grids (where one part of the grid is higher resolution than the rest of the grid, often used for weather prediction; Hill, 1968). Time in the model is discretised using timesteps. The timestep and grid resolution must be carefully chosen, as a compromise between accurately capturing physical processes and being prohibitively expensive in CPU time to run.

GCMs have been used in the study of the Earth for decades. Early models had their roots in numerical weather prediction, becoming viable with the proliferation of computers. The first true global climate model used a 17×16 grid with 2 vertical layers and a timestep of 1 day during the 130-day spin up, reduced to 2 hours after this (Phillips, 1956). By comparison, an unexceptional modern model run might use a grid on the order of $200 \times 100 \times 40$ (the latter being the vertical dimension) with a timestep under 30 minutes, and can quite easily run on a personal laptop, albeit at fairly low resolution. In addition to weather forecasting, modern models are used to look at how the climate system behaves and how it might change in future, especially in the context of human activity. ("Climate" refers to the long-term average, over a period decades, in contrast to "weather" which is short term, though there is not necessarily a clear line between the two, particularly with modern models that can acceptably simulate both.)

As computational power has increased, more physical processes have been coupled into the models (in tandem with increasing resolution). The first developments were the coupling of the ocean, which has its own circulation, to the atmosphere (Manabe and Bryan, 1969), but advanced modern models incorporate features like a dynamic land surface, chemistry, aerosols, complex weather (precipitation, clouds, lightning, etc.), biology (perhaps including human activity) in an attempt to simulate all climatically-relevant parts of the Earth as a system. These models are known as Earth system models (ESMs) (Flato, 2011).

The physical processes simulated in an ESM are called feedbacks, as they are intricately and fundamentally linked with the climate; for example, clouds reflect shortwave radiation back into space, which affects heating at the surface, which in turn affects evaporation of water, feeding back into cloud formation. Much like an astronomer, an Earth scientist cannot conduct an experiment with the Earth system,

meaning that the magnitude and relative importance of the various climate feedback systems cannot be measured except through simulations. These feedbacks are a major source of uncertainty in climate models (Flato, 2011).

Atmospheric chemistry is one such feedback process, and simulation of chemistry is a useful feature of GCMs. One example of this is the action taken regarding the ozone hole, in which GCMs were instrumental (e.g. WMO, 2007). Atmospheric transport of chemicals like chloroflourocarbons, solar radiation, meteorological features such as polar stratospheric clouds and other parts of the system interact in unpredictable ways. The complexity of this system meant that scientists did not foresee the rapid depletion of ozone at the poles that occurred at the end of the 20th century. On the Earth, ozone plays an important role in shielding the surface from UV, and ozone depletion therefore has immediate health impacts for humans; more generally, it is intrinsically linked with stratospheric temperatures and thus climate change, global circulation and weather. It is thought that the Montreal Protocol, which phased out ozone-depleting substances, has mitigated warming on the order of 1°C at the poles (McKenzie et al., 2011).

Shortly after the first GCMs for Earth appeared, models were built to study the atmosphere of extra-terrestrial planets. Simulations of Mars were conducted beginning in 1969 (Leovy and Mintz, 1969), and have been useful in understanding its potential for habitability and unique features such as the importance of dust in the circulation (Haberle et al., 1982). Venus has a particularly interesting atmosphere, with a strong super-rotating jet and high pressures and temperatures, perhaps having formed in a state not dissimilar to Earth's; it has been studied with GCMs since the 70s (Chalikov et al., 1971; Kálnay de Rivas, 1975; Young and Pollack, 1977). Studies of the other Solar System planets were conducted around the same time, including comparative experimental studies of Earth-like planets (e.g. Williams and Holloway, 1982).

More recently, the discovery of exoplanets has spawned a whole new field, with a number of highly advanced GCMs being developed to study the atmospheres of planets ranging from hot Jupiters to tidally-locked M-dwarfs. We discuss some highlights of exoplanet atmosphere modelling in the previous sections and in section 3.1.

In the cases of the Solar System planets, it is worth remembering that data from probes and landers were becoming available around the same time (in many cases the models helped to inform mission parameters in terms of expected wind speeds, temperatures, etc.). For some time, computational power limited what could be accurately simulated; scientists could not casually run a 3D simulation of a planetary atmosphere and hope to get useful results. This is significantly different to modern-day exoplanet simulations, where computer time is cheap and but observational data are lacking. This paradigm leads to a more speculative, predictive approach.

1.3 Aims and thesis outline

The factors determining habitability are not well constrained. There are two approaches that can help to resolve this problem. Firstly, we must continue to make assessments of habitability to the best of our knowledge. This includes both the evaluation of new environments (that have not yet been examined in the context of habitability) and the further exploration of the habitability parameter space (examining habitability over a range of plausible parameters, especially the interplay between these parameters, and examining the effects of a perturbation on an environment that is thought to be habitable or uninhabitable already).

Secondly, we must continually reevaluate our assumptions about habitability and its assessment, to check that they are still accurate. For example, as little as a decade ago M-dwarf planets were not considered to be strong contenders for habitability, partly because it was thought by some that tidally-locked atmospheres might collapse on the night side and boil off on the day side due to the extreme heating and cooling (Tarter et al., 2007). However, studies with GCMs showed that heat transport on a tidally locked planet is highly efficient, resulting in much more balanced day and night side temperatures than initially expected from simple 1D simulations (Joshi et al., 1997; Showman et al., 2009). Re-examination of the global circulation regime with more sophisticated tools, along with new knowledge about the vast number of M dwarfs and habitable-zone terrestrial M-dwarf planets (compared with Sun-like stars), have now led some researchers to conclude that M-dwarf planets may actually be *more* favourable for life than G-star planets[5] (Shields et al., 2016). It is thus important to review our perceptions about habitability and correct them when necessary.

The aim of this thesis is to further our understanding of habitability through these approaches. We pay particular regard to the use of models and knowledge of the Earth's atmosphere. Exoplanet atmospheres have, until the last decade, been modelled in a basic fashion using 1D models and in almost all cases ignoring atmospheric chemistry feedbacks. Often this is appropriate; most known planets are so different from Earth that sophisticated models become pointless due to the major uncertainties in composition and atmospheric dynamics, and many celestial bodies are so uniform that there are almost no spatial variations around the sphere, meaning that 1D models perform just as well as 2D or 3D. However, as our capacity to detect Earth-like planets increases and we enter the era of the Earth analogue, knowledge of the Earth system becomes more important.

We therefore identify areas in the body of knowledge where we can use techniques

[5]There are still major uncertainties regarding M-dwarf planet habitability, especially with regards to stellar activity.

and knowledge from the Earth science community to enact the two approaches described above to constrain habitability.

In Chapter 2, we evaluate the habitability of recently-discovered cool brown dwarf atmospheres that have not yet been considered from an astrobiological perspective. Informed by the Earth's atmosphere, where organisms can spend significant amounts of time suspended in the atmosphere, perhaps even metabolically active, and where liquid water clouds are present at temperatures well below 273 K, we discuss the possibility of organisms living in the atmosphere of a cool brown dwarf. The organisms are hypothesised to float and sink in an atmospheric habitable zone between the cold upper atmosphere and the hot lower atmosphere, in a region where it may be possible to have liquid water clouds and a pressure similar to that at Earth's surface. We use a simple model with convective upward winds to show that organisms could persist in this environment for some time.

In Chapter 3, we continue to explore the habitability parameter space for tidally-locked M-dwarf planets. We have developed a model of a simple online atmospheric photochemistry scheme for an Earth-like exoplanet atmosphere. This scheme is a severely pared down version of the United Kingdom Chemistry & Aerosols model, which is a part of the Met Office Unified Model, that is intended to describe an ozone layer. We apply this model to a tidally-locked M-dwarf planet, nominally Proxima Centauri b, building on earlier work using the Unified Model for a similar simulation without chemistry. We focus specifically on the ozone layer and show that it differs significantly from an Earth-like ozone layer (often assumed in models) in a few key ways.

In Chapter 4 we expand upon the work of Chapter 3 by changing some key features of the model to cover more of the habitability parameter space. Furthermore, our results challenge the assumptions that atmospheric chemistry plays a minimal role in the climate of these planets and that photochemistry can be adequately described by 1D models. Specifically, we undertake some experiments to gauge the impact of the chemistry scheme on the model output, as well as looking at different orbits and examining the effects of an electromagnetic stellar flare on the atmosphere. We find that our model is very sensitive to atmospheric ozone due to the interaction between dynamics and radiative heating, and that output from the model differs in a few important ways when the ozone is included in a chemistry scheme rather than prescribed. Our results demonstrate the importance of 3D models with full online photochemistry, which are rarely ever used in exoplanet simulations.

Finally, Chapter 5 provides a review of the work presented herein and a further discussion.

CHAPTER 2

Habitability of Cool Brown Dwarf Atmospheres

ABSTRACT

We use a simple organism lifecycle model to explore the viability of an atmospheric habitable zone (AHZ), with temperatures that could support Earth-centric life, which sits above an environment that does not support life. To illustrate our model we use a cool Y dwarf atmosphere, such as WISE J085510.83–0714442.5 whose 4.5–5.2 micron spectrum shows absorption features consistent with water vapour and clouds. We allow organisms to adapt to their atmospheric environment (described by temperature, convection, and gravity) by adopting different growth strategies that maximize their chance of survival and proliferation. We assume a constant upward vertical velocity (caused by convection) through the AHZ. We found that the organism growth strategy is most sensitive to the magnitude of the atmospheric convection. Stronger convection supports the evolution of more massive organisms. For a purely radiative environment we find that evolved organisms have a mass that is an order of magnitude smaller than terrestrial microbes, thereby defining a dynamical constraint on the dimensions of life that an AHZ can support. Based on a previously defined statistical approach we infer that there are of order 10^9 cool Y brown dwarfs in the Milky Way, and likely a few tens of these objects are within ten parsecs of Earth. Our work also has implications for exploring life in the atmospheres of temperate gas giants. Consideration of the habitable volumes in planetary atmospheres significantly increases the volume of habitable space in the galaxy.

Author Contributions: This work has been published in the *Astrophysical Journal*; see Yates et al. (2017). I wrote the paper, developed the model and did the analysis. Paul Palmer, Beth Biller and Charles Cockell contributed some text to the Introduction and Discussion and editing suggestions.

2.1 Introduction

The recent discoveries of Earth-like planets orbiting their host stars outside our solar system are beginning to challenge our understanding of planetary formation and the development of extra-terrestrial life. A common definition of whether a planet is capable of supporting life is whether the effective surface temperature can sustain liquid water at its surface, which reflects several factors including the evolution of the planet and star, and the distance between them (Kasting et al., 1993). Here, drawing on our knowledge of Earth and inspired by previous theoretical work for the Jovian atmosphere we argue that an atmosphere sitting above a potentially uninhabitable planetary surface may be cool enough to sustain life. By doing this we define an atmospheric habitable zone (AHZ).

The Earth's atmosphere contains a large number of aerosolised microbes with concentrations ranging from 10^3 m^{-3} to more than 10^6 m^{-3} of air, of which approximately 20% are larger than 0.5 μm (Bowers et al., 2012). The atmospheric residence time of these organisms is highly uncertain but there is a growing body of works that show that some organisms are metabolically active, particularly in clouds (Lighthart and Shaffer, 1995; Lighthart, 1997; Fuzzi et al., 1997; Sattler et al., 2001; Côté et al., 2008; Womack et al., 2010; Gandolfi et al., 2013). Other solar system planets have been postulated to have a habitable atmosphere. The Venusian surface temperature ($\sim$738 K) is too high to sustain liquid water, so based on Earth-centric definitions it is uninhabitable. At the cloud deck at $\sim$55 km, where atmospheric temperatures are close to those at Earth's surface, liquid water is more readily available and conditions are more amenable to sustaining life (Cockell, 1999; Schulze-Makuch et al., 2004; Dartnell et al., 2015). The Jovian atmosphere has also been considered to be potentially habitable. Sagan and Salpeter (1976) described a microbial ecosystem that could optimise a survival strategy to take advantage of their physical environment.

To illustrate the idea of the AHZ we focus on cool, free-floating Y-class brown dwarfs (Kirkpatrick et al., 2012), thereby avoiding complications associated with any stellar effects on an atmosphere or on inhabiting organisms (e.g. radiation, stellar particles, and electromagnetic interactions). The coolest known brown dwarf WISE J085510.83 − 071442.5 (henceforth W0855-0714) has a mass $M_{\rm BD} = 6.5 \pm 3.5 M_{\rm Jup}$, a radius $R_{\rm BD} = R_{\rm Jup}, 6.99 \times 10^4$ km, and an effective temperature $T_{\rm eff} \approx 250$ K (Beamín et al., 2014; Faherty et al., 2014; Kopytova et al., 2014; Luhman, 2014). We expect that the upper atmosphere of cool objects similar to WISE0855-0714 will have values for temperature and pressure similar to Earth's lower atmosphere, and models and the latest spectra have suggested that liquid water in clouds may also be present (Faherty et al., 2014; Morley et al., 2014a; Morley et al., 2014b; Skemer et al., 2016). Observed

spectra for cool brown dwarfs are consistent with significant dust loading in the upper atmosphere (Tsuji, 2005; Witte et al., 2011). These aerosols can provide charged surfaces on which prebiotic molecules, necessary for life, could form (Stark et al., 2014). Prebiotic molecules could also be delivered to the brown dwarf atmosphere via dust from the interstellar medium (Muñoz Caro et al., 2002). Based on current understanding, M/L/T brown dwarf atmospheres also contain most of the elements that are thought to be necessary for life: C (in CH_4, CO, CO_2), H (CH_4, H_2, H_2O, NH_3, NH_4SH), N (N_2, NH_3), O (CO_2, CO, OH), and S (NH_4SH, Na_2S) (for example, see Allard et al., 2012; Cushing et al., 2005; Cushing et al., 2006; Cushing et al., 2008; Cushing et al., 2011; Kirkpatrick et al., 2012).

We develop the idea of a cool brown dwarf atmospheric sustaining life in its atmosphere by using a simple 1-D model to describe the evolution of a microbial ecosystem, following Sagan and Salpeter, 1976, that is subject to convection and gravitational settling. The simplicity of our approach allows us to develop a probabilistic understanding of the survival of individual organisms under different environmental conditions.

In the next section we describe our numerical models. In section 2.3 we present analytical and numerical results, including a small number of sensitivity experiments that test our prior assumptions. We discuss our results in a broader astrobiological context and conclude the chapter in section 2.4.

2.2 Model description

We develop a simple atmospheric model that retains a sufficient level of detail to describe the atmospheric environment that drives variations in the lifecycle of the organism population. The organism model draws from nutrient-phytoplankton models used to described ocean biology on Earth (e.g., Franks, 2002), but we allow organisms to determine an evolutionary growth strategy that is best suited to the atmospheric environment.

2.2.1 Brown dwarf atmosphere

As described above, our illustrative calculations are based loosely on the object W0855-0714 (Luhman, 2014). We are interested in the region of the atmosphere that has temperatures in the range 258 K $< T <$ 395 K, which represent the lower and upper limits for life on Earth (McKay, 2014). We define the AHZ as the atmospheric region(s) that fall between those limits.

For our work, we define a $T-P$ profile based on the 200 K, $\log g = 5.0$ profile from the 1D model of Morley et al. (2014b), assuming an atmosphere composed of 85% H_2 and 15% He. We assume these gases exhibit near-ideal behaviour so we can calculate density using the ideal gas law and altitudes can be calculated from scale heights. We define altitude at the bottom of the AHZ as 0 km, and the P-T profile places upper edge of the AHZ at $\sim$ 105 km. We calculate the luminosity of the object using the Stefan-Boltzmann law and $T_{\rm eff} \sim 250K$ (Luhman, 2014).

Our model atmosphere assumes the presence of liquid water in the AHZ to support the biochemistry necessary to sustain life, as we know it on Earth. This assumption restricts us to the coolest Y dwarfs and also, for example, some cool gas giants. To illustrate our AHZ hypothesis, we use a T–P (T_{gas}–P_{gas}) profile determined from a 1-D hydrostatic model atmosphere simulation for Y dwarfs (Morley et al., 2014a). This model assumes equilibrium condensation processes such that super saturation = 1. For a $T_{\rm eff}$ = 200 K, $\log g$ = 5 object, the T–P profile places the water phase transition between gas/liquid and ice at a temperature lower than 273 K at 0.7 bar pressure (Morley et al., 2014a). To illustrate our model we use a cool Y dwarf atmosphere, for example WISE 0855-0714 whose $4.5 - 5.2$ micron spectrum shows absorption features consistent with water vapour and clouds (Skemer et al., 2016). A supporting model calculation for this object ($T_{\rm eff}$ = 250 K) shows that the temperature profile intercepts the saturation vapour pressure at $\simeq$273 K (Skemer et al., 2016), assuming equilibrium condensation processes (Morley et al., 2014a). In nature, non-equilibrium processes (super saturation $>$ 1) compete with equilibrium processes, allowing liquid water to

exist at super cooled (metastable) temperatures much lower than 273 K (e.g. Rogers and Yau, 1995; Helling and Fomins, 2013; Helling and Casewell, 2014).

Homogeneous freezing of pure liquid water is due to statistical fluctuations of its molecular structure such that smaller drops (<5 microns) freeze spontaneously at temperatures closer to 243 K while larger droplets freeze at slightly higher temperatures (Rogers and Yau, 1995); similar empirical results are found for heavy water (Wölk and Strey, 2001). On Earth, liquid water is not commonly found at such low temperatures suggesting a role for heterogeneous freezing processes. Liquid clouds are more commonly found at 253 K (Rogers and Yau, 1995). A cloud can be considered as a collection of independent liquid droplets such that each droplet must be subjected to a nucleation event before the whole cloud is frozen. A consequence of this is that mixed-phase clouds are common over the coldest (polar) geographical regions on Earth (Morrison et al., 2012; Lawson and Gettelman, 2014; Loewe et al., 2016). Aerosols and aqueous solutions influence nucleation of ice. Aerosol particles can act as ice nuclei. Ice can form directly from the gas phase on suitable ice nuclei via deposition and freezing heterogeneous nucleation processes (Rogers and Yau, 1995). Liquid water existing as a component of an aqueous solution can significantly affect the temperature at which ice begins to nucleate, depending on the water activity of the solution (Koop et al., 2000). Based on this we argue that homogeneous and heterogeneous nucleation processes allow liquid water to exist at temperatures much lower than 273 K. The lower limit for the AHZ temperature is, however, determined by the coldest temperature ($\sim$ 253 K) that can support Earth-based life.

For simplicity, we use a constant convective vertical velocity $v_{\mathrm{conv.}}$ throughout the AHZ. We use values of $v_{\mathrm{conv.}}$ taken from a 3-D model of atmospheric dynamics (Showman and Kaspi, 2013), which was used to study L/T dwarfs. Because Y dwarfs are cooler we expect the associated convective velocities to be smaller. We use two values, $v_{\mathrm{conv.}} = 100$ cm s^{-1} and $v_{\mathrm{conv.}} = 1000$ cm s^{-1}, which cover a range of plausible convection scenarios, to assess the effect of the windspeed on the final population of organisms. In addition we consider a radiative atmosphere, with $v_{\mathrm{conv.}} = 0.01$ cm s^{-1}.

2.2.2 Model of organisms and their lifecycle

We describe an individual organism as a spherical shell, following Sagan and Salpeter, 1976. The shell is described by its radius, skin width, mass, and density of the organic skin (Figure 2.1). Organisms increase their mass by consuming biomass, described below. Increasing an organism's mass increases its size and skin width according to an

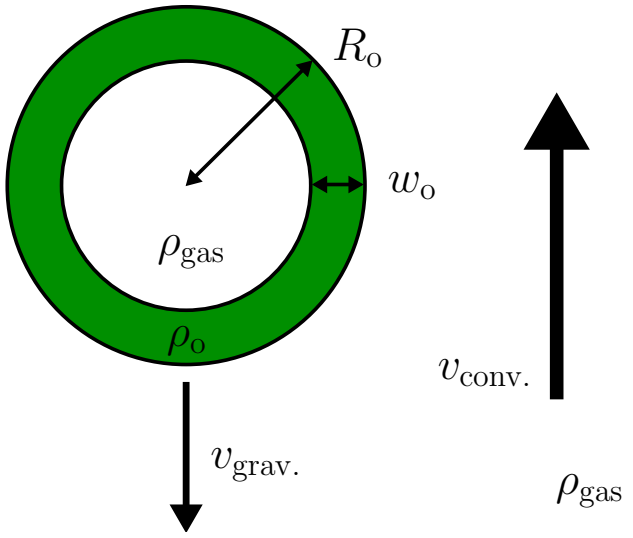

Figure 2.1: Schematic of a model organism. The thickness and density of the organic skin layer are denoted by w_0 and ρ_0, respectively. The radius of the shell is denoted by R_0 and the density of the gas within the skin, in equilbrium with the atmosphere, is denoted by ρ_{gas}. The upward velocity is denoted by $v_{conv.}$ and the terminal velocity due to gravity is denoted by $v_{grav.}$.

organism-specific growth strategy, G, which is given by

$$w_o = (1 - G)R_o, \tag{2.1}$$

where w_o is the organic skin thickness, and R_o is the radius of the sphere. Thus an individual organism with $G \to 1$ is balloon-like, whilst organisms with $G \to 0$ are (approaching) solid throughout. We limit the skin densities ρ_o to range between 0.5 g cm^{-3} $< \rho_o <$ 1.5 g cm^{-3}. This is equivalent to densities greater than some light woods and less than the density of heavy woods and bone. As a comparison, humans and microbes are approximately 1.0 g cm^{-3}, the density of water, reflecting their bulk composition. For the purpose of this paper we assume this skin is permeable so that the density of the organism within the skin is the same at the atmosphere ρ_{gas}. At the start of each experiment organisms are uniformly distributed throughout the AHZ.

Each organism has a lifecycle of growth, reproduction (subject to sufficient growth), and death. Organisms that are better suited to their atmospheric environment will generally have more progeny, so their parameter regime (analogous to genetic material) survives for longer. At each timestep in our model an organism eats, moves according to its sinking rate and the windspeed (dies immediately if it is now outside the AHZ), reproduces subject to growth rate, and finally has a chance of dying according

to a specified half-life.

The growth of an organism is determined by its consumption of biomass. Without any observational constraint we have been intentionally vague on the composition of this biomass. On Earth, organism growth is typically limited by the availability of one element, compound, or energy source at any one time. Populations of plankton in the Earth's ocean, for example, are limited by the availability of trace elements (such as P or N). We account for this by using a finite amount of biomass that is available for consumption by the organisms. Consumed biomass is returned to the atmosphere after an organism dies. The biomass is initially distributed evenly throughout the AHZ, and after each timestep any returned biomass is vertically distributed in the AHZ as a function of the organism weight within each vertical layer.

Organisms move only by convection and gravitational settling (Figure 2.1). We assume laminar flow (defined by the Reynolds number) so that the terminal velocity of the organism is given by equating Stokes' drag force to the gravitation force:

$$v_{\text{grav.}} = -\frac{\rho_{\text{o}} - \rho_{\text{gas}}}{\rho_{\text{gas}}} \frac{g V_{\text{o}}}{6\pi\nu R_{\text{o}}}, \tag{2.2}$$

where $v_{\text{grav.}}$ is the sinking velocity of the organism relative to the gas; ν is the kinematic viscosity; g is the gravitational acceleration ($16,670$ cm s^{-2}); and V_{o}, the volume of the organic material, is given by

$$V_{\text{o}} = \frac{4\pi\left(R_{\text{o}}^3 - \left(R_{\text{o}} - w_{\text{o}}\right)^3\right)}{3} = \frac{4\pi R_{\text{o}}^3\left(1 - G^3\right)}{3}. \tag{2.3}$$

The vertical movement Δh of the organism per timestep τ is given by $(v_{\text{conv.}} + v_{\text{grav.}})\tau$ so that the vertical position h after n timesteps $h_n = h_{n-1} + \Delta h$. On Jupiter and Saturn the different observed bands are thought to be sites of upwelling and downwelling. Models have suggested that Jupiter's banded structure is stable, and have also suggested that similar structures might be common in brown dwarf atmospheres (Showman and Kaspi, 2013). Based on this study, we assume that convection is stable such that at some latitudes the upward velocity will be approximately constant, and at these latitudes the body might sustain bands of life.

Each organism has a half-life of 30 Earth days, which is reasonable for Earth microbes. We retain organisms that meet the following criterion: $2^{-\frac{\tau}{T_{1/2}}} > \mathcal{U}[0,1]$, where $\mathcal{U}[a,b]$ is a number drawn from the uniform distribution with limits $a < b$, and all other variables are as previously defined. We acknowledge that some microbes are very short-lived or can spend many years cryogenically frozen before being revived (Gilichinsky et al., 2008). For simplicity, we assume that an organism dies if it moves

outside the AHZ, but we discuss this further in subsection 2.4.3.

Each organism attempts to reproduce at every timestep. The number of progeny, n_c, is determined by dividing the mass of the organism by its "reproduction mass", rounding down and subtracting one (the organism retains some mass after it reproduces). If $n_c \geq 1$, we split the organism into n_c progeny (and itself), each with a slightly perturbed set of inherited characteristic to account for genetic mutation. Therefore, as an example, if the organism mass is $3.1m_{\text{repr.}}$ it will have two progeny each of mass $m \approx m_{\text{repr.}}$. The reproduction mass is close to the birth mass of the organism, with some small variation. Inherited characteristics vary according to a distribution with the mean being the value of the parameter for the parent. Growth strategies use a normal distribution, limited to 0.01–0.99, with a standard deviation of 0.05; densities use a normal distribution, limited to 0.5–1.5 g cm^{-3}, with a standard deviation of 0.05 g cm^{-3}; reproduction masses are varied according to a log-normal distribution with a standard deviation of 10% of the mean. The initial skin width and size can be inferred from the density, strategy and the initial mass.

2.2.3 Model algorithm/flow

In terms of the program flow, the model proceeds as follows. We firstly initialise the model. This entails calculation of the atmospheric properties (such as density, scale height, kinematic viscosity, and eddy diffusion coefficient), which are stored in an array, and initialisation of organisms, either from the saved state of another model run or randomly. When restarting from a previous saved state we maintain the seed value for the random number generator, such that two model runs with the same restart configuration always end in the same end state. Once it is initialised, we timestep the model:

1. First, check that the model is still supposed to be running by comparing the current model time with the requested end of the model run, and check that there are still living organisms in the model. If these are not both true the model should stop.

2. Allocate the unused "potential biomass" on each atmospheric level to the organisms on the same level, proportional to their current mass. That is, if there is 10 μg of biomass on an atmospheric level with 2 organisms of masses 3 μg and 2 μg, the former will receive 6 μg of "food" (new mass will eventually be 9 μg) and the latter 4 μg (new mass 6 μg).

3. Loop through living organisms; in each case:

(a) increase the organism's mass according to the unused biomass they have been allocated for "eating" and recalculate size, based on the organism's genetic parameters (i.e. G, the organism's strategy and ρ_{o}, the density of its organic material)

(b) recalculate (terminal) drift velocity $v_{\mathrm{grav.}}$ (using Stoke's drag equations), subtract this from updraft velocity $v_{\mathrm{conv.}}$ and move the organism a distance $(v_{\mathrm{conv.}} - v_{\mathrm{grav.}}) \times \tau$ through the atmosphere where τ is the timestep.

(c) move the organism to a new atmospheric level if required (we track which atmospheric level the organism is on as well as altitude in the level)

(d) check whether the organism is still inside the AHZ and kill it if not

(e) split the organism into progeny (and itself) if it is large enough. If it has any progeny, we use the statistical distributions described above to randomise the inherited genetic properties. We then resize all of these organisms according to mass and genetic properties

(f) increment the organism's age by τ, and randomly kill it according to the half-life distribution.

4. Once every organism has undergone a timestep, we purge dead organisms from the model array and return their biomass to the atmospheric levels for the next timestep. At this stage we sort the organisms according to altitude, as this gives a performance benefit.

5. Disperse biomass through the atmosphere, so that it doesn't accumulate on one level. In past versions of the model the dispersion was achieved with a Gaussian blur, but this was removed in favour of even division across atmospheric levels (that is, after this step all levels have the same amount of spare biomass), which is much faster. Tests have shown this did not have any impact on final organism populations.

6. Write out the model state (at a user-specified cadence). We write out every property of every organism in the model. (Atmospheric parameters are not required, as they are the same every time.)

We continue to timestep the model until either the specified end time is reached or all organisms die.

2.3 Results

2.3.1 Analytical model estimates

For verification of our numerical model results, we calculate an estimate of organism sizes and masses for a given convective windspeed using the model described above, by assuming a zero net vertical velocity so that an organism can float indefinitely in the convective updraft inside the AHZ.

As described above, we limit the densities of the organisms to 0.5 g cm^{-3} $< \rho_{\rm o} <$ 1.5 g cm^{-3}, while gas densities in the AHZ range from 0.4 mg cm^{-3} to 1.2 mg cm^{-3}. We can then assume $(\rho_{\rm o} - \rho_{\rm gas})/\rho_{\rm gas} \approx \rho_{\rm o}/\rho_{\rm gas}$ so that Equation 2.2 becomes:

$$R_{\rm o}^2 \rho_{\rm eff.} = \frac{9 v_{\rm conv.} \nu \rho_{\rm gas}}{2g}. \tag{2.4}$$

We assume that the gravitational acceleration is effectively constant throughout the AHZ ($g = 16,670$ cm s^{-2}); and that ν ranges from 0.1 cm^2 s^{-1} at the hottest part to 0.2 cm^2 s^{-1} at the coldest part of the AHZ, with corresponding values of $\rho_{\rm gas}$ of 1.2 mg cm^{-3} and 0.4 mg cm^{-3}. We account for the inner cavity by absorbing the change in mass into the value of $\rho_{\rm o}$ to determine an "effective density", $\rho_{\rm eff.}$. For a value of $G \approx 0.5$, $\rho_{\rm eff.} \approx 7\rho_{\rm o}/8$ assuming $\rho_{\rm gas} \ll \rho_{\rm o}$. The growth strategy therefore does not make a significant difference until $G > 0.8$, after which $\rho_{\rm eff.} < \rho_{\rm o}/2$. Most organisms are in the regime where $\rho_{\rm eff.} \approx \rho_{\rm o}$.

Based on these assumptions, Figure 2.2 show typical values for the vertical position, size, and effective density of organisms for a given windspeed. We find that for moderate windspeeds (< 1000 cm s^{-1}) in the convective zone, a typical organism should be a few orders of magnitude more massive and about a factor of ten larger than a terrestrial microbe ($\sim 10^{-12}$ g, $< 10^{-4}$ cm). These estimates will be a useful check on the full model results. We find that different values of ν and $\rho_{\rm gas}$ indicative of the cold and hot limits of the AHZ change masses by less than a factor of 2 and sizes even less.

2.3.2 Numerical model estimates

Our control model experiment has a convective windspeed of 100 cm s^{-1}, a timestep of six hours, a initial population of 100 organisms with an approximate mass of 10^{-9} g distributed randomly (with a uniform distribution) across the AHZ. Each organism is initialised with random properties. We run an ensemble of 20 simulations, each for 100 Earth years.

We test each simulations for steady state conditions by looking at the stationarity

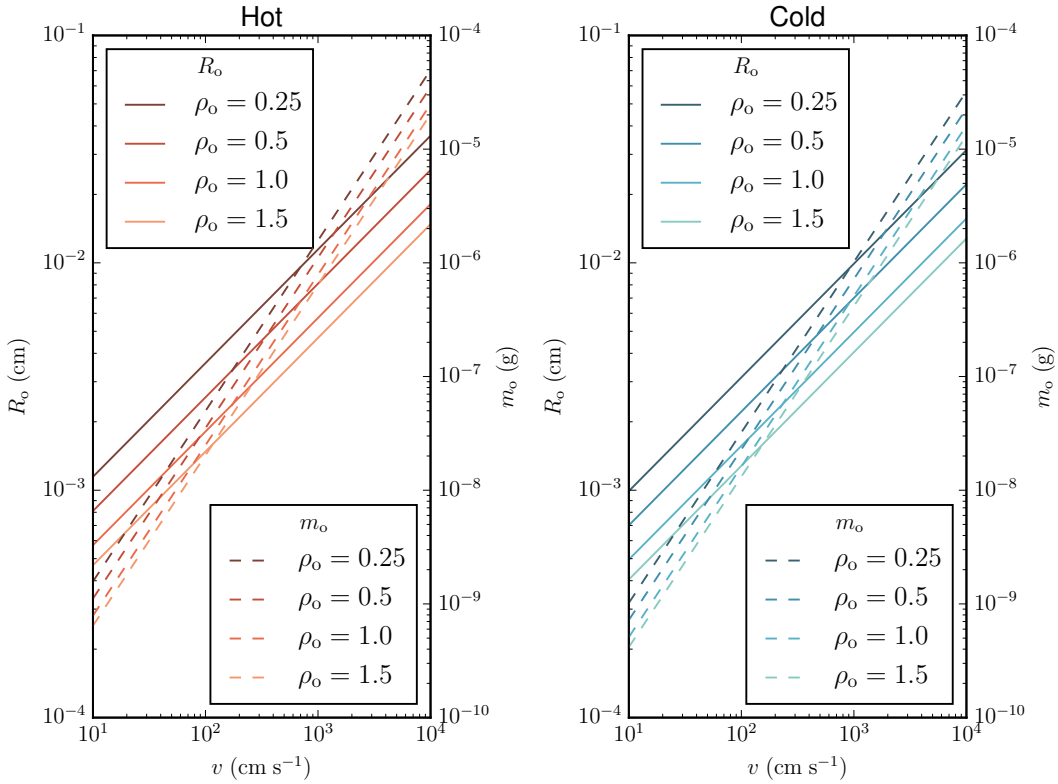

Figure 2.2: Expected size and mass of an organism for a given windspeed determined using the analytical model. The line colour denotes the density of the organism including the cavity. Solid lines denote the radius, R_o, required for the sinking rate to match the upward windspeed. The dashed lines denote the corresponding mass, m_o. Hot denotes the hotter, lower AHZ (395 K) and cold denotes the colder, higher AHZ (258 K), which use corresponding values for ν (hot 0.1 cm^2 s^{-1}, cold 0.2 cm^2 s^{-1}) and ρ_{gas} (hot 1.2 g cm^{-3}, cold 0.4 g cm^{-3}).

of the total number of organisms; a trend or changing variance would indicate that the population was still undergoing changes and had not yet settled to a viable strategy. To achieve this we use an augmented Dickey-Fuller (henceforth ADF) test (Said and Dickey, 1984) on the last 75 years of population data and found that all runs had reached steady state to a very high significance ($p < 0.01$). We present results that represent the mean model state from the last Earth year of each experiment.

Figure 2.3 shows that organisms are approximately evenly spread throughout the AHZ with a small skew towards to the top. An approximately even distribution suggest that the organisms have found a mass/size strategy to support a stable population. In general this strategy is found within a few years. The age distribution of the organisms follows the expected half-life distribution well, with the exception of a large number of very young organisms. These small organisms are also visible in the mass, skin width and size distributions. We find this population is a persistent feature of our experiments, but individuals have a short residence time as they are rapidly convected out of the AHZ. The population is an artefact of our reproduction scheme: individually they are unviable but are frequently produced as they only require a small amount of mass. The densities are evenly spread across the allowed range with a small skew to higher densities, suggesting that there is most likely no significant effect on the dynamical behaviour of the organisms. Densities are forced within the range 0.5 g cm^{-3} $< \rho_o <$ 1.5 g cm^{-3}, which accounts for the small excesses at either end of the distribution. Aside from the population of small, short-lived organisms, the mass distribution peaks at around 2×10^{-8} g, with most organisms being between 10^{-9} and 10^{-7} g, which is consistent with the analytical model. Organisms within this range are relatively stable in the convection, with residence times of 30 days or more.

We find that the growth strategy favoured by the organisms in the control calculation is skewed towards lower values of G, i.e. particles that are less hollow. As discussed above for the analytical calculations, the effect of the growth strategy on the organism's size or effective density goes approximately with the cube of G. Thus values of $G < 0.8$ have very little effect on the dynamical behaviour of the organism, which we see in the distribution. The distribution of skin widths and size is as expected with the peak value for the skin width between 0.3 and 3×10^{-3} cm, consistent with the analytical model.

2.3.3 Sensitivity runs

We run a small set of sensitivity runs to test our prior model assumptions; for each sensitivity experiment we run a ensemble of 10 replicates. Table 2.1 summarises the parameters of our sensitivity runs. We use the ADF to ensure that all resulting

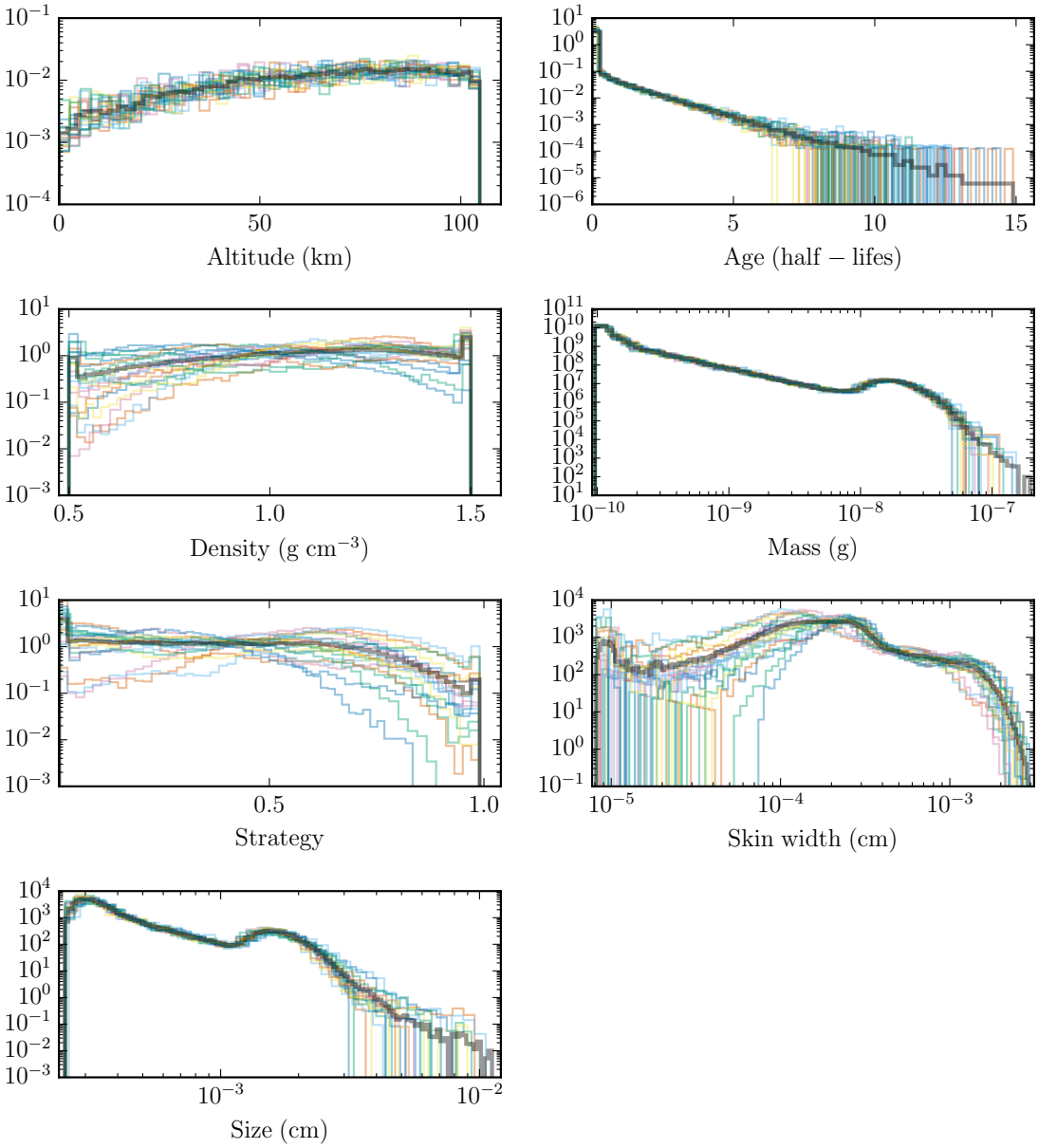

Figure 2.3: Normalised frequency distributions of organisms in the AHZ in the control runs, as a function of altitude, age (as half-lives), density, mass, growth strategy, skin width, and size. The dark lines denote the average of the ensemble of the 20 individual model run shown by coloured lines. The frequency distribution is normalised such that its integrates to unity between the lowest and highest values.

Description	m_{input} (g)	B	τ (hrs)	$v_{\text{conv.}}$ (cm s^{-1})	$T_{1/2}$ (days)
Control run	10^{-9}	1	6	100	30
High windspeeds	10^{-8}	1	2	1000	30
Radiative windspeeds	10^{-13}	1	6	0.01	30
Population increase	10^{-9}	3	6	100	30
Initial input mass	2×10^{-9}	1	6	100	30
Short half-life	10^{-9}	1	6	100	15
Long half-life	10^{-9}	1	6	100	60

Table 2.1: Initial conditions for each set of sensitivity runs. Shown is the mean initial organism mass m_{input}, the approximate biomass factor B relative to the control run, the timestep in Earth hours τ, the windspeed $v_{\text{conv.}}$, and the half-life of the organism $T_{1/2}$. Runs below the horizontal line are not discussed further, as they do not significantly change the population.

populations were stable and sustainable. We find that our results are not significantly sensitive to changes in the initial conditions for the organisms (i.e. not windspeeds) and these results are not discussed further.

In a brown dwarf atmosphere heat transport will be dominated by either radiation or convection; the transition point is called the radiative-convective boundary (Marley and Robinson, 2015). Most models find the radiative-convective boundary to be somewhere above the AHZ, but it is possible for it to be below the AHZ or even inside it. We run the models with vertical velocities of 1000 cm s^{-1} and 0.01 cm s^{-1}. The slower of these velocities is intended to replicate windspeeds in the radiative zone. Changing the wind speed will affect the range of masses that could be sustained in the AHZ: generally, slower convection supports the evolution of lighter organisms and higher convection supports the evolution of heavier organisms.

There are two implications of changing the vertical velocity that we consider when choosing the lower and upper values. First, varying the windspeed will change the distribution of organism sizes and masses that can sustain a population. To address this we also change the range of masses that are allowed within the model based on the analytical model results described above. Second, changing the vertical velocity changes the distance over which organisms can move during one timestep. We have addressed this by co-adjusting the timestep so that the Courant Friedrichs Lewy criterion is met (that is, distance travelled in one timestep is less than the length of a model grid box; Courant et al., 1928). We find that our results are not significantly affected by changing the model timestep.

Figure 2.4 and Figure 2.5 shows that the organism population distributions corresponding to vertical velocities of 1000 cm s^{-1} (fast convection) and 0.01 cm s^{-1} (radiative zone), respectively, are different to those from the control run. We find that

skin widths peak at around 5×10^{-4} cm and 3×10^{-3} cm with sizes showing two peaks at 7.5×10^{-4} cm and 8×10^{-3} cm. Thus in most cases organisms have small cavities, which is also reflected in the strategy graph. Masses drop off steadily from 10^{-9} g to a second peak at 10^{-6} g. Here the analytical calculations have somewhat overestimated the required mass to sustain a population. Age and altitude graphs are consistent with the control run.

For the radiative experiment, the organism distributions are generally similar to those of the control experiment. There is a skew in the vertical distributon of the organisms, where there are approximately twice as many organisms at the bottom of the atmosphere when compared with the top. The age distribution is close to a perfect half-life distribution. This non-convective environment also appears to support a slightly wider range of growth strategies. Unlike the control experiment, the non-convective environment cannot support the highest masses with the distribution falling off near-monotonically in log-space. This is consistent with our analytic model that shows that for every tenfold decrease in windspeed organisms should decrease in mass by a factor of $10^{3/2}$. The expected mass of approximately 10^{-14} g is comparable to the mass of a terrestrial virus (Johnson et al., 2006). Terrestrial microbes are a factor of $\sim$100 too massive to be supported by this environment. This environment could be considered as habitable if life could be described by something much smaller than a terrestrial microbe.

The half-life of organisms will impact the ability of the AHZ to sustain life. For example, shorter organism half-lives mean greater turnover of biomass and a reduced emphasis on the atmospheric transport in determining observed variations. To address this we used a half-life that was half and double that of the 30-day control run value. For organisms with a 15-day half-life there is an excess of very young organisms compared with old organisms, which is due to a higher turnover of biomass that increases birth rates. Other distributions are not significantly different from the control case.

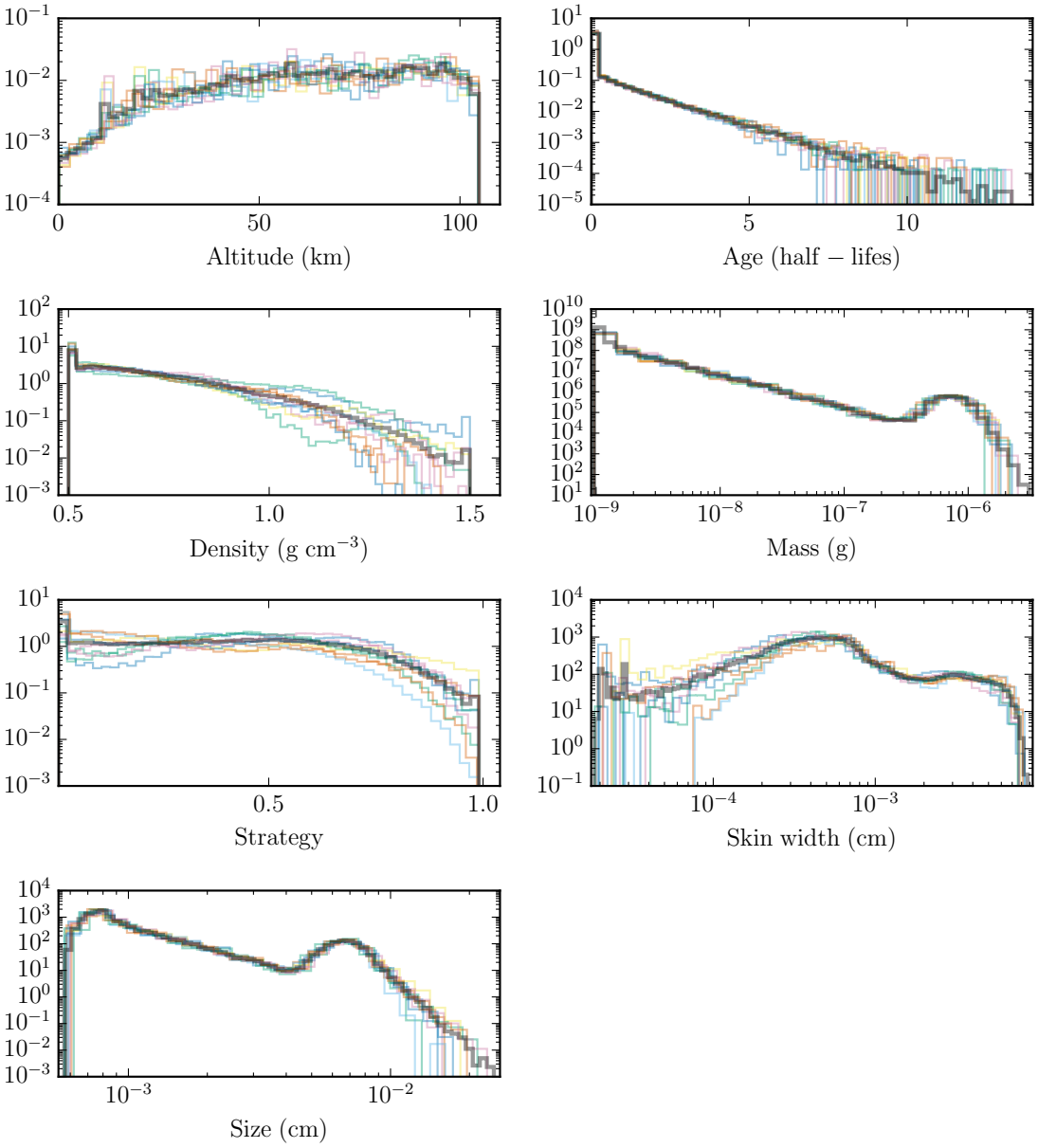

Figure 2.4: As Figure 2.3 but using a convective velocity of 1000 cm s^{-1}.

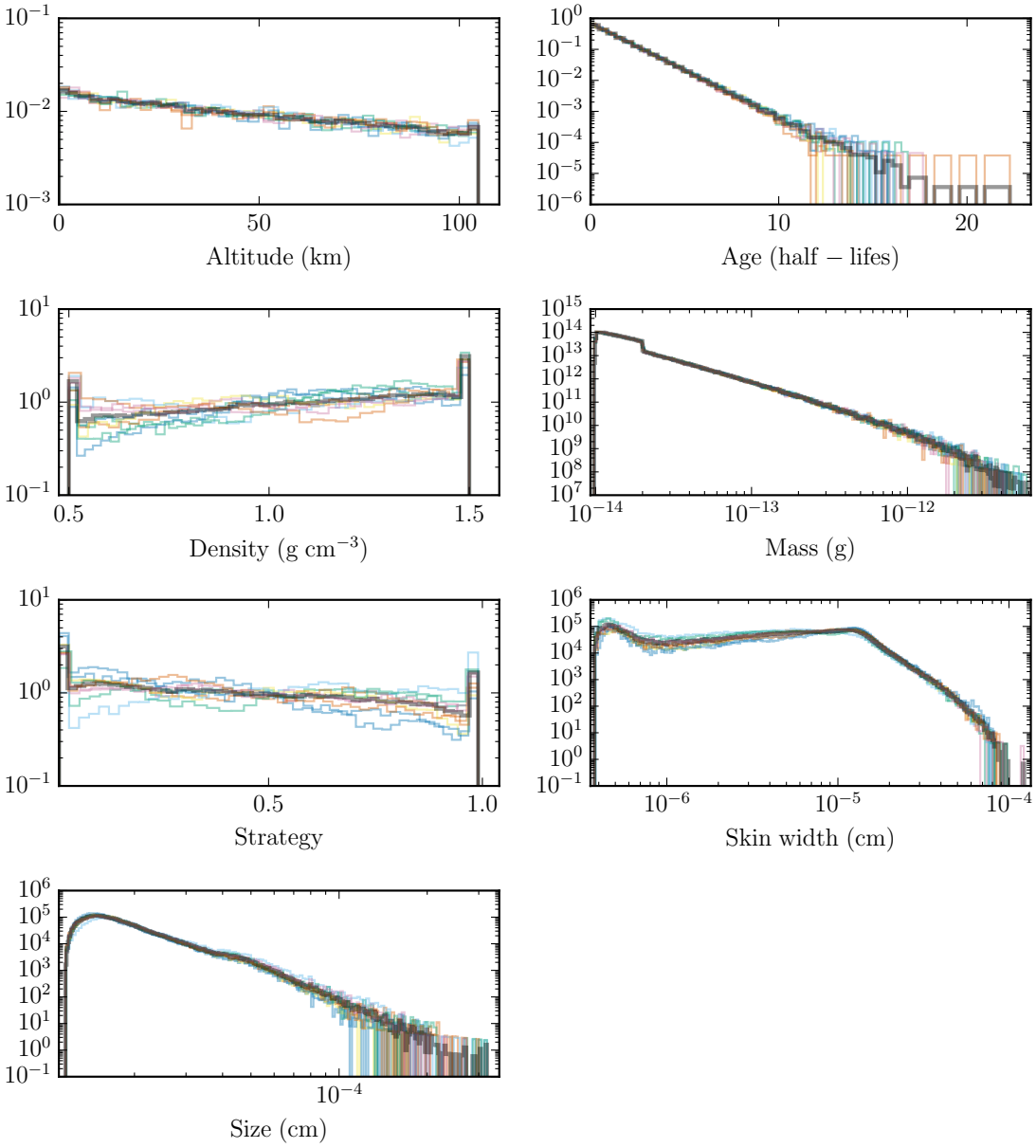

Figure 2.5: As Figure 2.3 but using a radiative vertical velocity of 0.01 cm s^{-1}.

2.4 Discussion

Here, we put our model results into a wider context. We also discuss briefly the associated implications for habitability.

2.4.1 Cool brown dwarf spatial frequency and galactic significance

There are only tens of known cool brown dwarfs of which WISE 0855-0714 is the coolest. These objects are inherently faint and consequently are difficult to detect unless they are nearby. To understand how common AHZs might be, we extrapolate from the number of known Y dwarf objects (though the results are likely applicable to other types of bodies).

To estimate the frequency of these cool brown dwarfs, we determine spatial densities based on the distances of known objects, following Kirkpatrick et al. (2012). For objects that are uniformly distributed in space, with some objects yet to be discovered, we perform a $V/V_{\rm max}$ test to assess the completeness of a sample. First, we calculate the interior volume V_i of each real object, i.e. the spherical volume centred on Earth, with radius d_i, where d_i is the distance to object i. The sample is assumed to be complete out to some distance $d_{\rm max}$. Within the corresponding interior volume, $V_{\rm max}$, the mean value of $V_i/V_{\rm max}$ should be 0.5. Using the value of $d_{\rm max}$, we can estimate the spatial density of the objects by dividing the number of objects closer than $d_{\rm max}$ by $V_{\rm max}$. Here, we calculate $d_{\rm max}$ for each spectral type, rather than define a value of $d_{\rm max}$ and assess the completeness (Kirkpatrick et al., 2012). (Naturally, we reject objects with $V_i/V_{\rm max} > 1$. In this case we remove the objects and recalculate $V_{\rm max}$ until all objects have $V_i/V_{\rm max} > 1$.)

We analysed brown dwarfs of spectral type Y0 or later with published parallaxes, using the data from Tinney et al. (2014) and references therein. Where there is more than one published parallax, we take a mean weighted by the inverse of the square of the uncertainties. We group objects into two spectral type categories: spectral types Y0 − 0.5 and ≥ Y1.

For the Y0 − 0.5 category we include 9 objects and reject 4. We find $d_{\rm max} = 9.6$ pc, $V_{\rm max} = 3.6 \times 10^3$ pc^3 and a spatial density of $\sim 2.5 \times 10^{-3}$ pc^{-3}. For the ≥ Y1 objects, we include 3 objects and reject 1. Here we find $d_{\rm max} = 10.85$ pc, $V_{\rm max} = 5.4 \times 10^3$ pc^3 and a spatial density of $\sim 0.6 \times 10^{-3}$ pc^{-3}.

Assuming the Milky Way is a disk with a diameter of 4×10^4 pc and a thickness of 600 pc (corresponding to a volume of $\simeq 750 \times 10^9$ pc^3), we can project these numbers on to the galaxy as a whole. These calculations produce very approximate numbers of 2×10^9 objects with spectral type Y0 − 0.5 and 0.5×10^9 objects with spectral type

$\geq$ Y1 in the galaxy. Further, we expect that there should be around 10 Y0 $-$ 0.5 dwarfs and 2 $\geq$ Y1 dwarfs within 10 pc of Earth.

Clearly these samples are highly incomplete so we consider this a conservative estimate. Brown dwarf cool as they age on timescales of billions of years (Baraffe et al., 2003). Hotter objects will eventually develop an AHZ, while for cooler objects the AHZ will descend in the atmosphere and will contract as the effective temperature falls and the lapse rate grows. As the AHZ descends the associated pressure will increase so that the nature of the organisms as we describe them here will undoubtedly change.

2.4.2 Implications for habitability

Estimating the total potential biomass achievable in an aerial biosphere of a brown dwarf for which we have very limited knowledge of the elemental composition of the atmosphere, let alone the nutritional requirements of a hypothetical biota, cannot be done with accuracy. We still have much to learn about how nutrient limitation and co-limitation influences the distribution of biomass on Earth. However, from a more general point of view, we would expect that the upper limit of biomass theoretically achievable in a brown dwarf atmosphere to be determined by (bio-)availability of specific nutrients. Once more data are available on the atmospheric composition of very cool brown dwarf atmospheres it may even be possible to predict which elements would limit a potential biota in these environments. We are not aware of any modelling studies predicting the presence of phosphorus in significant quantities.

The implications of the AHZ concept for habitability in the galaxy are significant. In the most simplistic view there are, conservatively, billions of cool brown dwarfs in the galaxy and hundreds within a few tens of parsec of the Earth. Some of these will be targets for characterisation by next-generation telescopes in less than a decade, although their inherent faintness makes them difficult to find in surveys.

When searching for habitable environments, we naturally take an Earth-centric focus on terrestrial planets that receive their energy from a host star. Thermal spectra of W0855-0714 shows features consistent with atmospheric water vapour and clouds (Skemer et al., 2016), suggesting that self-heating is sufficient to produce an atmosphere with liquid water at habitable temperatures. This observation is not limited to application to brown dwarfs; Jupiter receives approximately as much heating from the Sun as from its core, as does Saturn. Gas giants in other stellar systems could also potentially support similar biomes. Our work provides further evidence for the habitability of planets such as Venus that have an uninhabitable surface. Whilst the dynamics of Venus' atmosphere will likely be very different to that of a cool brown dwarf or gas giant, it seems likely that with some adjustment of the properties one could

model an organism that could sustain a population in the Venusian AHZ indefinitely. Thus we support the idea that the inner edge of the circumstellar habitable zone is not a hard limit on habitability. Detecting this aerial biosphere with current and next-generation telescopes will depend on the range and resolution of the spectrally-resolving instruments, and also the range and magnitude of byproduct gases that the organisms produce.

2.4.3 Reflections on our model organism

We described organisms as individual hollow spheres with a permeable skin. Organisms that successively evolved within the prescribed physical environment of the AHZ eventually shaped the final cohort that were characterised by their radius and skin thickness. While our organism model does exist in nature, e.g., pollen spore with air sacs, we did not impose any further constraint that could impact their atmospheric lifetime in the AHZ.

We did not consider the coalescence of similar organisms or deposition onto existing airborne particles. Earth bacteria can occur as agglomerations of cells or attach themselves to airborne particulate matter, such as pollen, or aqueous-phase aerosol (Jones and Harrison, 2004). In our simple approach, we can consider an organism as a single entity or an agglomeration of many entities. Heavier organisms sink in the atmosphere at greater speeds. Organisms made of lots of individual entities could employ an additional survival strategy: organisms could attach to each other or to atmospheric particulates as temperature decreases (as they ascend), and disperse as temperature increases (as they descend), allowing them to self-correct to find the centre of the AHZ. This strategy is similar to that proposed by Sagan and Salpeter (1976), where organisms increase in mass and split into low-mass daughter cells as they sink to the lower parts of the AHZ.

We also did not consider cryogenic freezing of organisms above the top of the AHZ. It is conceivable that an organism could pass through the upper boundary of the AHZ, spend some time in statis and subsequently sink back into the AHZ, whereupon it would thaw and reactivate. We anticipate that low-mass or low-density organisms would have greater survivability in this scenario.

Surface roughness is another parameter that organisms could use to adapt to their environment. A rough surface would increase the drag properties of the organism, resulting in slower movement that deviates significantly from Stoke's formula (Md et al., 2015). Recent empirical evidence also suggests that if a microorganism has the ability to maintain a charge it could substantially decrease its drag (Md et al., 2015). If the charge could be manipulated it could be used to stabilise the altitude of organisms.

In nature, there are a number of examples where animals manipulate their body drag through water. Fish can alter the drag between their skin and medium by altering their body smoothness by excreting high-molecular weight polymer compounds and surfactants (Daniel, 1981) or in the case of sharks by altering their body geometry (Dean and Bhushan, 2010). Studies have also proposed that seals and penguins actively use bubble-mediated drag reduction, required to launch themselves out of water (Davenport et al., 2011).

While our model of an organism is rudimentary there do exist in nature a number of examples in which animals control their movement in a laminar flow. Therefore it is possible that our microorganisms could have evolved to stabilise their movement without the need for necessarily changing their physical dimensions.

2.5 Conclusions

We used a simple organism lifecycle model to explore the viability of an atmospheric habitable zone (AHZ), with temperatures that could support Earth-centric life. The AHZ sits above some uninhabitable environment, such as an uninhabitable surface (e.g. as on Venus) or a hot dense atmosphere (e.g. the lower atmosphere of a brown dwarf or gas giant). We based our organism model on previous work that explored whether the Jovian atmosphere could support life. We illustrated this idea using a cool Y brown dwarf, for example object W0855-0714.

Our atmospheric model assumed availability of liquid water that is necessary to support the biochemistry associated with life. There exist valid counter arguments for the presence of liquid water in the AHZ of a cool brown dwarf (e.g., changes in metallicity may affect partial pressure of water, although metallicity has to change by orders of magnitude to affect H_2O (Helling et al., 2008)), which may suggest that our model is valid only for a small subset of available cool Y dwarfs (and a range of gas giants). The formation history of brown dwarfs result in a wide range of atmospheric chemical composition environments, e.g. Madhusudhan et al., 2016. In the authors' view the most compelling argument for the presence of liquid water is the observed thermal spectra of WISE 0855-0714 that showed evidence of atmospheric water and clouds (Skemer et al., 2016). Based on our understanding of Earth's atmosphere, water clouds cannot exist without the presence of liquid water.

We also assumed a constant upward vertical velocity through the AHZ and model organisms that float in the convective updrafts. Our modelled organisms can adapt to their atmospheric environment by adopting different growth strategies that maximise their chance of survival and producing progeny. We found that the organism growth strategy is most sensitive to the magnitude of the atmospheric convection. Stronger convective winds support the evolution of more massive organisms with higher gravitational sinking rates, counteracting the upward force, while weaker convective winds results in organisms that need less mass to overcome the upward convective force. For a purely radiative environment we found that the successful organisms will have a mass that is ten times smaller than terrestrial microbes, thereby putting some dynamical constraints on the dimensions of life that the AHZ can support.

We explored the galactic implications of our results by considering the likely number of Y brown dwarfs in the galaxy, based on the number we know. We calculate that of order 10^9 of these objects reside in the Milky Way with a few tens within ten parsecs of Earth. Some of these close objects will be visible to large telescopes in the next decade. Our work has focused on brown dwarfs but it also has implications for exploring life on gas giants in the solar system and exoplanets, which have uninhabitable

surfaces. Our calculations suggest a significant upward revision of the volume of habitable space in the galaxy.

CHAPTER 3

Modelling Atmospheric Ozone on M-dwarf Planets

ABSTRACT

We have developed a model of a tidally locked M-dwarf planet with a full, online chemistry scheme, consisting of a simplified ozone production and loss mechanism with the hydrogen oxide (HO_x) catalytic loss cycle. We use the Met Office Unified Model, a 3D global circulation model, modified for exoplanets. With the addition of chemistry this is one of the most sophisticated models of an exoplanet to date, and is one of the first models of its kind. The model results demonstrated that M-dwarf stellar flux is sufficient to generate an ozone layer on a planet with an O_2, H_2O and N_2 atmosphere at Earth-like abundances and atmospheric mass.

We find that ozone accumulates on the night side of the planet, where there is no UV radiation and therefore no significant ozone loss mechanism. The cold traps – cold points on the night side of the planet, to the north and south of the equatorial atmospheric jet – have a particularly high concentration of ozone due to the extremely long ozone lifetime. Atmospheric transport and dry deposition play a major role in the structure of the atmospheric ozone layer, with HO_x dominating the ozone loss throughout the atmosphere and deposition being more important at the surface.

Author Contributions: I wrote the chapter, developed the simulations and performed the analysis, with guidance and editing suggestions from Paul Palmer. Paul Palmer, Nathan Mayne (University of Exeter), Ian Boutle (Met Office), James Manners (Met Office) and Luke Abraham (Cambridge) offered significant input on the model development.

3.1 Introduction

As observational capabilities improve our prospects of detecting a habitable "Earth-like" planet increase. Recent surveys have detected of Earth-sized planets on close orbits around cold M-dwarf stars, notably Proxima Centauri b (Anglada-Escudé et al., 2016) and the TRAPPIST 1 planets (Gillon et al., 2017). For these planets, orbital distance and low stellar flux compensate for each other, resulting in Earth-like levels of top-of-atmosphere (TOA) radiation, placing them in the circumstellar habitable zone (Kasting et al., 1993).

It is no coincidence that these planets orbit M-dwarfs; they represent 70% of all stars (Bochanski et al., 2010), and the detectability of their planets is greater (when compared with Sun-like stars), due to the increased planet-to-star radius ratio. Furthermore, the detectability of a planet increases as the orbital semi-major axis decreases because of the diminished effect of inclination, the increased frequency of transits and the larger radial-velocity signature. As an M-dwarf is cooler than a Sun-like star the circumstellar habitable is closer in; thus, a planet in the habitable zone of an M-dwarf star is much more likely to be detected and we are able to detect smaller planets around these stars (below an Earth radius) (Charbonneau and Deming, 2007). Demographic studies also suggest that M-dwarfs are more likely than larger stars to host small planets (Shields et al., 2016).

In sum, these observational factors suggest that M dwarfs are our best hope for finding habitable zone exoplanets. However, there are a large number of unknowns in the assessment of M-dwarf planet habitability[1]. In addition to the normal considerations of the atmospheric composition, the magnitude of the greenhouse effect, the stellar environment, the inventory of water and other factors that may determine habitability on a terrestrial planet (see Figure 1.1 and Meadows and Barnes, 2018), there are: the increased M-dwarf activity (and additional susceptibility of the planet to the effects of activity due to the much nearer circumstellar habitable zone); the impact of tidal interactions and heating between the star and planet; the effect of the change in stellar energy distribution (skewed towards longer wavelengths); the parameters of the planet's orbit and rotation, including synchronous rotation; magnetic interactions between the star and planet; and other factors (Shields et al., 2016). These planets differ significantly from anything in the solar system, so the importance of each of the above factors is still unknown. Until telescopes are capable of detailed observations of M-dwarf planets, we are limited to examining them through speculative modelling

[1]In this chapter and the next we broadly take the simplistic Earth-centric definition of habitability; a planet with liquid water at the surface. However, we also consider the environmental conditions at the planetary surface, in particular UV radiation.

efforts.

To that end, studies with GCMs have shown that close-in M-dwarf planets, even tidally locked, could host liquid water at the surface (e.g. Boutle et al., 2017; Turbet et al., 2017; Meadows et al., 2018). For a terrestrial planet the global circulation is driven almost entirely by stellar radiation, which is by far the largest heat source in the system. Naturally this creates spatial inhomogeneities. For a tidally-locked planet with a permanent day and night side, these inhomogeneities are even more exaggerated. In this scenario, the 3-dimensional nature of the system – a hot day side, a cold night side and an atmospheric jet transporting heat around the equator – means that 1-dimensional models are not necessarily sufficient to properly simulate the atmospheric dynamics. This is especially true when clouds and convection are involved, as these processes are difficult to simulate in 1 dimension (see e.g. Tompkins, 2000; Palmer, 2012, for a discussion of these difficulties).

Historically, GCM studies of M-dwarf planets have not incorporated a full chemistry scheme, partly due to the uncertainties in the atmospheric composition and partly due to the perceived sufficiency of 1D chemistry (where chemistry is needed). On the Earth, the day and night chemistry is different (see relevant sections in e.g. Jacob, 1999; Seinfeld and Pandis, 2006), most obviously where driven by photons. Informed by the results from GCMs, one might expect that the spatial inhomogeneities in the circulation and dynamics drives non-uniform chemistry, resulting in planets that have different day- and night-side chemical environments. This is particularly relevant to tidally locked planets, which have gyres on the night side (Showman and Polvani, 2011) that trap air, extreme day-night temperature differences compared with a fast-rotating planet like Earth, and portions of the atmosphere or surface that are never exposed to stellar radiation.

Simulations of a "tidally locked Earth" (which orbits in 365 days but is tidally locked) have confirmed that there are chemical differences on the day and night side of a tidally locked planet (Proedrou and Hocke, 2016). In that work, a simple ozone-based photochemistry model showed that night-side ozone was enhanced over the day-side, and that ozone was present at different altitudes on each side. In addition, the authors found that as chemical lifetimes[2] on the night side of the planet became longer the atmospheric transport becomes more important, contributing to the non-uniform ozone distribution. However, these simulations used an Earth-like top-of-atmosphere radiation flux, a 365-day year and Earth continents, which limit applicability to M-dwarf planets such as Proxima Centauri b. The stellar radiation spectrum in particular plays a critical role in the determination of the chemical equilibrium state of the ozone

[2]The expected amount of time that a molecule will persist before being consumed in a reaction.

layer.

Projecting from these results, we suggest that in the case of a planet where (for example) gases which determine atmospheric heating interact through chemistry, or where the presence of an ozone layer affects the surface UV environment, the inclusion of a chemistry scheme could dramatically change the habitability of the planet (either directly or through dynamics). To test this hypothesis, we develop a fully 3D online photochemical model of atmospheric ozone, which is known to be radiatively important and a factor in planetary habitability, shielding the surface from harmful radiation, and apply it to a tidally-locked M-dwarf exoplanet, nominally Proxima Centauri b.

3.1.1 Ozone in Earth's stratosphere

On Earth, stratospheric ozone can be approximated through a simple set of chemical mechanisms; in order of importance, the Chapman cycle (involving oxygen atoms and molecules and UV photons), the hydrogen oxide (HO_x) catalytic loss cycle (involving the oxidation of water), the nitrogen oxide (NO_x) catalytic cycle (involving molecules produced through aircraft exhaust fumes, lightning, biogenic emissions and volcanic activity), the chlorine radical (ClO_x) loss cycle as well as other mechanisms involving CFCs, gases produced by plankton, polar stratospheric clouds and so on. If we are interested in habitable planets, in most cases we assume the presence of oxygen and water in the planetary atmosphere. Therefore, if there are sufficient UV photons present, we can approximate the planetary ozone through the same mechanisms, especially the Chapman mechanism and the HO_x cycle. However, the unknowns relating to planetary composition and geology mean that we cannot necessarily assume that NO_x or ClO_x will be present. We therefore narrow our focus to the Chapman mechanism and the hydrogen oxide catalytic loss cycle, which are described in more detail below.

$$\begin{aligned}
\textbf{Initiation}: \quad & O_2 + h\nu \rightarrow 2O(^3P) \quad (\lambda < 240\text{nm}) && \text{(R1)}\\
& O(^3P) + O_2 + M \rightarrow O_3 + M && \text{(R2)}\\
& O_3 + h\nu \rightarrow O_2 + O(^1D) \quad (\lambda < 320\text{nm}) && \text{(R3)}\\
& O(^1D) + M \rightarrow O(^3P) + M && \text{(R4)}\\
\textbf{R3 + R4 Net}: \quad & O_3 + h\nu \rightarrow O_2 + O(^3P) \quad (\lambda < 320\text{nm}) &&\\
& O_3 + O(^3P) \rightarrow 2O_2 && \text{(R5)}
\end{aligned}$$

The Chapman mechanism is given above (Jacob, 1999). Here M denotes an inert molecule such as N_2, and $O(^3P)$ and $O(^1D)$ are the ground and first excited state of atomic oxygen respectively. Note that reactions R1 and R3 require UV photons with wavelengths less than 240 nm and 320 nm respectively[3]. The M dwarf spectrum (approximately) follows a blackbody distribution; thus small, cold stars such as Proxima Centauri output significantly less radiation at UV fluxes due to their reduced blackbody temperature and these photons are much less abundant at the TOA for a red dwarf planet when compared with the Earth, even if total insolation power is the same. With insufficient 240 nm photons the Chapman mechanism cannot be initiated and therefore no O_3 will form. This is the crux of the problem of ozone layer viability on a tidally-locked red dwarf planet.

On the Earth, reactions R2, R3 and R4 are fast, resulting in continuous exchange between O_3 and $O(^3P)$, whilst R1 and R5 are slow. However, the mechanism will work differently in the case of a tidally-locked M-dwarf planet. We note that R3 is likely to be much slower due to the reduced UV flux, resulting in an enhancement of O_3 over $O(^1D)$ (relative to Earth). We also note that once O_3 has been formed, either an $O(^3P)$ atom or a UV photon is required to break it down again; thus, if O_3 is transported to the night side of a tidally-locked planet it will persist until it is transported back onto the day side, assuming that the $O(^3P)$ lifetime is too short for significant transport to the night side.

$$\begin{aligned}
&\textbf{Initiation}: && H_2O + O(^1D) \rightarrow && 2OH && \text{(R6)}\\
& && OH + O_3 \rightarrow && HO_2 + O_2 && \text{(R7)}\\
& && HO_2 + O_3 \rightarrow && OH + 2O_2 && \text{(R8)}\\
&\textbf{R7} + \textbf{R8 Net}: && 2O_3 \rightarrow && 3O_2 &&\\
&\textbf{Termination}: && OH + HO_2 \rightarrow && H_2O + O_2 && \text{(R9)}
\end{aligned}$$

The HO_x catalytic cycle is given above (Jacob, 1999). Note here that the initial formation of the OH molecule requires the presence of the excited $O(^1D)$ atom, which (in our case, as on Earth) is only produced by a UV photon in the Chapman mechanism. Hence OH cannot be produced on the night side of a tidally-locked planet. Again the $O(^1D)$ lifetime is short, so it is not transported in great quantities. On the night-side, where O_3 cannot be produced (due to the lack of UV photons), transported OH could

[3]We show the stellar spectrum for an M-dwarf and the Sun in Figure 3.1. These are scaled to top of the atmosphere fluxes, but the relative number of 240 and 320 nm photons is illustrative.

conceivably destroy a large amount of O_3 before the reaction is eventually terminated; however, once OH is converted back into H_2O and O_2, no further OH can be produced. At this point the lifetime of O_3 becomes very long (essentially infinite) as there are no possible reactions that remove it in either the HO_x cycle or the Chapman mechanism. Thus night-side lifetime of O_3 will depend on largely on lifetimes and abundances of HO_2 and OH.

3.1.2 Summary of earlier UM work

Our chosen model for these simulations is the Met Office Unified Model (UM), a model that has been extensively verified for both short-term weather prediction and long-term climate studies for the Earth, which has recently been generalised to simulate exoplanets. The adaptation of the UM for exoplanets was described in Mayne et al. (2013) and Mayne et al. (2014). In this initial work, the UM was generalised to simulate dynamics of gas giant planets. Later work with the UM has demonstrated the importance of both 3D modelling for dynamics and the inclusion of chemistry. In Lewis et al. (2018), it was demonstrated that a continent can radically change the dynamics in a planetary atmosphere; placing a continent at the substellar point of a tidally locked planet changes the day-night temperature contrast and cools the planet, and moving the continent eastward of the substellar point was enough to change the global circulation, generating two counter-rotating jets and weakening the typical central jet. These complicated dynamics cannot be simulated in 1D. In Drummond et al. (2018b), it was shown that opacity was the dominant driver of the thermal/dynamical structure in the atmosphere of GJ 1214b. In Drummond et al. (2018a) it was shown that the inclusion of a coupled chemical relaxation scheme dramatically changed methane abundance in a hot Jupiter atmosphere, a result that significantly differed from earlier studies with 1D and 3D models without chemistry. These works clearly show the value of a GCM fully coupled with a chemistry model, and that less sophisticated model may in some cases get the results wrong. The complexity of the model and its ability to describe complicated 3D dynamics could therefore make the difference between a simulated planet being habitable or not.

The basic model setup for our work is described in Boutle et al. (2017), henceforth referred to as Paper I, which builds upon the initial adaptation of the model to exoplanets. Here the authors adapted the generalised UM to a tidally locked M-dwarf planet, nominally Proxima Centauri b. In that work it was shown that Proxima Centauri b was likely to be habitable in a tidally-locked orbit (its orbital parameters are given in Table 3.1). Two different atmospheric compositions were used; the first was a nitrogen atmosphere with a small amount of CO_2 and the second an "Earth-like"

Parameter	Value
Semi-major axis / AU	0.0485
Stellar irradiance / W m^{-2} ($S_\oplus$)	881.7 (0.646)
Orbital period / Earth days	11.186
Ω / rad s^{-1}	6.501 $\times 10^{-6}$
Eccentricity	0
Obliquity	0
Radius / km ($R_\oplus$)	7160 (1.1)
g / m s^{-1}	10.9

Table 3.1: Planetary parameters for the simulated Proxima Centauri B planet.

atmosphere with the addition of O_2, O_3, CH_4 and N_2O. In both of their simulations the atmospheric composition was held constant in time, and it was suggested that in the Earth-like case a full coupled chemistry scheme might allow a better insight into the chemical evolution and steady state of the atmosphere.

Here we have taken the initial steps in the develop of an appropriate chemistry module for this model. The UM already contains a full chemistry scheme: the UK Chemistry and Aerosol model (UKCA). With some modifications, the fundamental chemical framework is general enough that it is applicable to any sufficiently Earth-like planet, thus we have chosen to adapt it rather than implement a new scheme. In this chapter we describe the adaptation of the UKCA for exoplanets, and show some initial results from a counterpart simulation of Proxima Centauri b with fully coupled chemistry.

3.2 Model Development and Setup

3.2.1 Chemistry scheme

In line with subsection 3.1.1, we removed all chemical reactions from the UKCA with the exception of the Chapman mechanism and the hydrogen oxide catalytic loss cycle (reactions R1 to R9). We also leave O_3 dry deposition and HO_2 wet deposition on[4]. We add or modify output variables to give reaction fluxes for each reaction in these mechanisms.

Each chemical species involved in these mechanisms (with the exception of O_2 and H_2O) is set to a flat field with a mass mixing ratio (MMR) of 10^{-9} so as to not bias the model with an initial field. Given that the initial reactants involved in the two reaction chains are O_2 and H_2O (and photons), which are highly abundant, we expect that with enough model time an initial tracer gas fields will have no impact on the end state of the model. We test this hypothesis in subsection 4.2.3.

3.2.2 Radiation scheme

There are two separate radiation schemes in the model. The first interacts dynamically with the model; that is, absorption, reflection, heating rates etc. calculated using this radiation. This is the standard UM radiation scheme. The stellar spectrum for this aspect of the model is identical to the one used in Paper I, and is shown in Figure 3.1. This spectrum is from BT-Settl for an M dwarf with $T_{\text{eff}} = 3000$ K, $g = 1000$ ms^{-2} and metallicity = 0.3 dex (Rajpurohit et al., 2013).

The UKCA uses a separate radiation scheme, with more bands than the dynamical radiation model, which is applied only for photodissociation and other chemical reactions. In the original UKCA model there is no flux scaling with orbital distance, since this is insignificant (in terms of chemistry) for the Earth, and the model cannot describe non-Earth-like orbits. We therefore we scale the flux to a stellar insolation constant (given at 1 AU) and synchronise the stellar position between the two parts of the model. The stellar spectrum in the UKCA is subdivided into 18 bands, and we calculate the flux in these bands from the same spectrum as above. Flux in each band is given in Table 3.2. Note that highest-energy UV radiation is severely reduced compared to redder bands, with only 2 photons per second per cm^2 in the 187 nm band.

[4]Dry deposition is the removal of a chemical at the surface whilst wet deposition is absorption in droplets of precipitation.

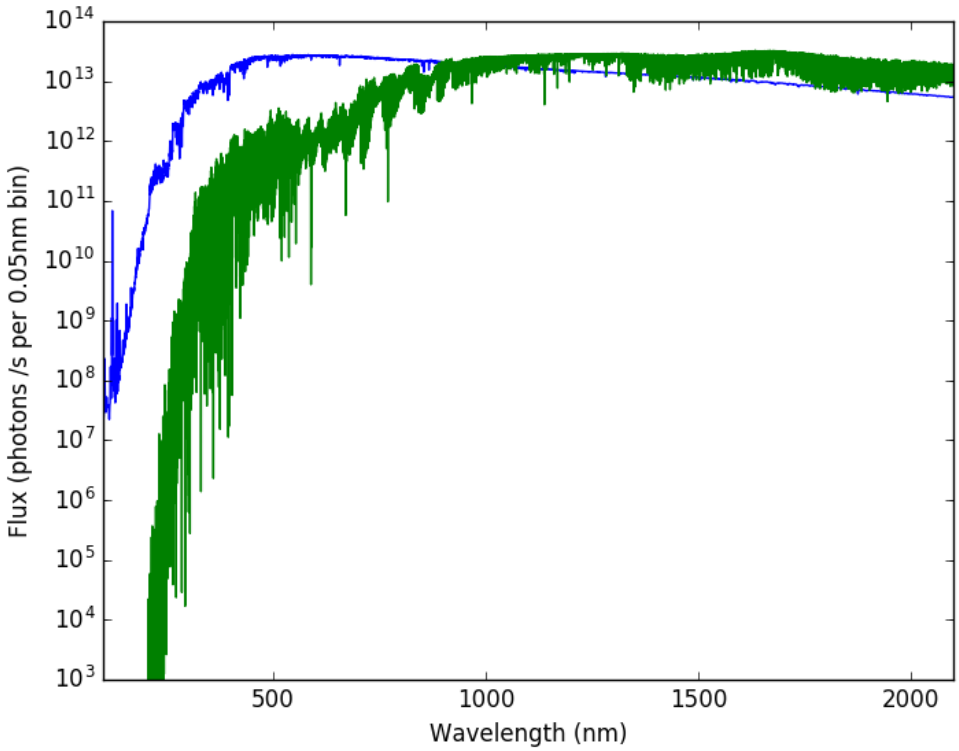

Figure 3.1: Proxima Centauri b TOA flux. The blue line is TOA flux for Earth, green is Proxima Centauri b, both scaled to the semi-major axis of orbit. Units correspond to those used in the model; a flux in a small wavelength bin.

Wavelength band (nm)	TOA flux at 1 AU (photons s^{-1} cm^{-2})
187	2.213
191	2.874
193	3.589
196	1.205×10^1
202	3.502×10^1
208	5.388×10^2
211	6.885×10^2
214	1.684×10^5
261	2.107×10^7
267	4.660×10^7
277	1.922×10^8
295	9.886×10^8
303	1.066×10^9
310	3.349×10^9
316	1.390×10^{10}
333	1.110×10^{11}
380	1.980×10^{12}
574	1.319×10^{15}

Table 3.2: M-dwarf TOA flux in UKCA bands, given at 1 AU.

3.2.3 Other model parameters

To allow simple comparisons, the model setup replicates the tidally-locked case from Paper I, with planetary parameters as described in Table 3.1. We use the "Earth-like" configuration from Paper I, except with trace greenhouse gases (GHGs) removed, leaving only a constant background of 23.14% O_2 (MMR) and 0.0594% CO_2 (MMR) with the remainder being composed of the dynamic tracer gases we are investigating (e.g. O_3, OH etc.) and N_2 (approximately 77%).

The trace GHGs that were removed are CH_4 and N_2O. We chose to remove the GHGs as they are chemically important species; both interact with O_3. Whilst it is possible to run the model with the gases acting in the radiation/dynamics scheme and not the chemistry, we do not think this makes any physical sense. We discuss this decision further in subsection 3.4.1.

In Paper I the atmosphere extends only to around 40 km on 38 levels. To study the ozone layer, this must be extended to altitudes that are important for ozone chemistry. Therefore the model top was increased to 85 km with the addition of 22 layers for a total of 60, the lower 38 levels being identical to the ones in the Paper I model. High wind-speeds in the upper atmosphere, above 40 km, results in the violation of the Courant-Friedrichs-Lewy condition in the model (that is, the distance travelled

by a parcel of air in one timestep is greater than the size of a grid box), resulting in instability. To counteract this the model timestep was reduced from 20 (Earth) minutes to 12 minutes. Chemistry and radiation timesteps were unchanged from default values (1 Earth hour). Tests have shown that reducing the timestep should not significantly impact the simulation results. We maintain the $2^\circ \times 2.5^\circ$ model grid from the previous simulations, with the substellar point being at latitude and longitude 0°.

We refrain from a full description of physics in the model as this has not been changed with respect to Paper I. For a comprehensive description we direct the reader to Paper I and Mayne et al. (2013) and Mayne et al. (2014).

We run the model for 20 Earth years. We see no significant changes in the model atmosphere after the first $5 - 10$ years. We show that total atmospheric ozone mass is steady in Figure 4.1 to confirm that the model has reached some equilibrium state.

3.3 Simulation Results

Results from the model are presented below. For a detailed discussion of atmospheric dynamics we refer the reader to earlier works, particularly in Paper I, and focus here mainly on the atmospheric chemistry. As above, we run the model for 20 years for spin-up. At this point we run for a further 120 days; we then take a time mean over this period for each of the variables below, leaving a 3D grid of values for each. We plot portions of these grids as slices through specific lines of latitude or longitude, or means over latitude, longitude or both.

3.3.1 Basic description of simulated atmosphere

We show a simplified representation of the model atmosphere in Figure 3.2. The top panels show meteorological and dynamical parameters whilst the lower panels describe the chemistry. The left panels show an area-weighted mean profile for the day-side hemisphere whilst those on the right show the night-side. The atmospheric jet is visible peaking at around 30 km altitude. Dynamically the day and night sides are not significantly different; the jet is in the same location and air temperature is broadly the same, with the exception of very low altitudes (below 2 km), where it is much colder on the night side. Wind speeds are also increased at low altitudes (below 15 km) on the night side, from around 20 m/s to around 50 m/s, but above this the structure of the jet is similar. UV flux on the day side decreases slowly from 30 km to 10 km, after which it drops off sharply. Humidity is low at high altitudes and on the night side, but increases dramatically from 10 km downward on the day side. At these altitudes on the day side there is significant cloud presence which aligns with the humidity profile. On the night side there is minimal cloud cover. Broadly there is good agreement with Paper I, though we discuss this in subsection 3.4.1.

In the lower panels we can see the mean ozone profile, which is almost identical between the day and night sides, peaking at 30km. This is similar in structure to the classic predicted Chapman steady state profile and the ozone profile on Earth. Ozone concentration is slightly enhanced on the night side at low altitudes, which is due to an accumulation at the cold traps (discussed in subsection 3.3.3).

We show reaction fluxes (that is, the number of moles of reactant/product undergoing reaction per grid box per second for a given reaction) for the slow reactions in the chemical scheme, excluding fast cycling reactions R2, R3 and R4. On the day side there is significantly more flux for R1 than other reactions, and reaction flux roughly mirrors UV flux from the panel above dropping off at high altitudes as number density decreases. R5 occurs only above 15 km, roughly mirroring O_3 concentration, with

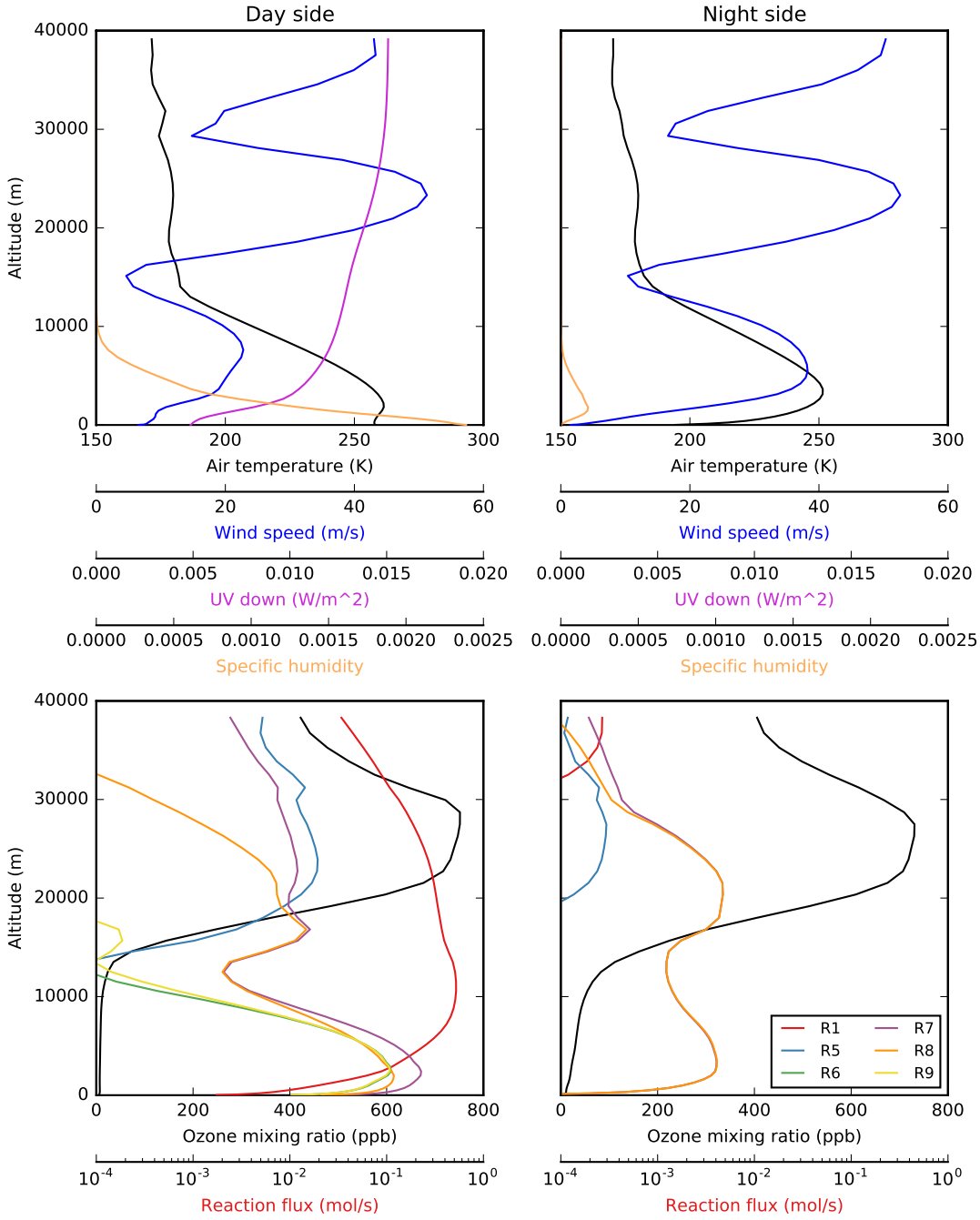

Figure 3.2: Basic properties of the simulated atmosphere. The left and right hand panels show hemispherical means for the day and night side respectively. The top panels show meteorological factors whilst the lower panels show chemistry. In the lower panels, the black line shows ozone burden per model grid box and the coloured lines show reaction fluxes for the reactions given in the legend (which refer to corresponding labelled reactions in the Chapman and HO_x mechanisms). Reaction fluxes are plotted logarithmically as a flux per model grid box. The legend in the lower right plot refers to the reactions in subsection 3.1.1.

around 100× more flux on the day side where $O(^3P)$ is being produced. By contrast, reactions from the HO_x mechanism occur mainly below 15 km. There is no flux for R6 above 15 km, roughly in line with humidity in the panel above. Other reactions display a double peak in the profile with some flux at $20 - 30$ km but significantly more in the lower atmosphere in the lowest 5 km. Reactions R6 and R9 occur almost entirely on the day side, whilst R7 and R8 occur on both sides. For the latter reactions the double-peaked distribution reverses on the night-side, with higher flux at 20km and lower below, but an overall reduced flux, from a maximum of around 0.1 mol/s to 0.01 mol/s. On the night side the profile of these two reactions is identical reflecting the cyclic nature of the mechanism. By contrast on the day side we see an excess of R7 at high altitudes and at $3 - 5$ km. To maintain chemical equilibrium (ignoring transport), the shortfall must be made up through R9; indeed we see that where there is a difference between R7 and R8 there is some flux of R9, and on the night side, where flux profiles are near identical, there is little to no R9 flux. Above 20 km, where there is fast transport (due to high wind speeds) R9 flux is lower.

3.3.2 Meteorological and dynamical factors

We discuss the dynamics and meteorology in the simulations below.

We show air temperatures in Figure 3.3. In the top left we show surface temperature. It is notable that there is a significant portion of the day-side hemisphere that is above the 273 K triple temperature meaning that with an Earth-like atmospheric composition it is possible for there to be liquid water at the planetary surface, as in Paper I. The cold traps are clearly visible at longitude 225°, latitudes 50° and −50° with temperatures of approximately 150 K. The presence of the atmospheric jet is also clear, warming the equatorial band around the night side, but temperatures remain below 273 K. There is a persistent thermal inversion on the night side with air between 2 and 5 km being warmer than air at the surface. At these altitudes air remains at approximately freezing point. Our maximum (time mean) temperature is 287 K and our minimum temperature in the cold traps is 147 K, in both cases 3 K cooler than Paper I. This is discussed further in subsection 3.4.1.

Wind speeds are shown in Figure 3.4 and Figure 3.5. The jet is visible in Figure 3.4 at around 30 km altitude. On the night side a strong persistent jet/wind structure develops in the lower atmosphere, but this disappears on the day side. At 15 km there is little wind in either direction, which results in a very stable layer in the atmosphere with very slow transport (refer to subsection 3.3.6 for further discussion). Wind speeds in the meridional direction are much slower than zonal winds.

We note the presence of vortex structure at the cold traps. Air travels poleward

after passing the cold trap (at around longitude 250°), then circles back down to rejoin the jet at the anti-stellar point (at 180°). This is clearly visible in the section through latitude 30° in Figure 3.5, where we see a reversal in wind direction centred at approximately longitude 225°, and in the longitude 225° slice in Figure 3.4, where we see strong negative (decreasing longitude) wind speeds at the poles in contrast the central latitudes. This structure serves to trap air on the night side of the planet, resulting in a long residence time for air that does not pass straight through the jet, and is an important feature impacting the ozone abundance, described below. These features are described in detail in Showman and Polvani (2011).

Finally we show downward UV flux in Figure 3.6. As shown in Figure 3.2 there is a slow gradient below 30 km with a sharp drop from around 10 km and below. At latitude 0°, there is a surprising increase in downward UV from 15 to 10 km, most visible in the contours in the longitude 0° plot. We attribute this to reflection; at the substellar point below 15 km there is complete cloud cover, resulting in high reflectivity.

The change in UV intensity as we descend through the atmosphere mirrors UV intensity on the Earth. High-energy UVC is rapidly absorbed at high altitudes, UVB is absorbed on a slower gradient through the ozone layer and UVA is attenuated at low altitudes but is most likely to reach the surface.

Our surface UV levels are much lower than on an Earth-like planet. We find that surface UV is approximately 100× lower than on a similar planet with Earth-like TOA radiation (c.f. section 4.4). The extremely low UV flux from the star means that even a weak ozone layer is enough to absorb harmful UV radiation. We also find that the significant cloud cover at the substellar point (described in Paper I) absorbs a large quantity of the surface UV. This is evident in the spatial structure in the surface UV, which shows depletion at the substellar point and an increase both to both the east and west.

3.3.3 Ozone layer

Atmospheric ozone is shown in Figure 3.7. The model suggests that an ozone layer does form even with reduced UV flux. In the top left we show the ozone column in Dobson units[5]. On Earth ozone columns are approximately 300 Dobson units, so columns on the M-dwarf planet are smaller by around an order of magnitude, with the exception of the cold traps, where ozone approaches Earth-like levels. In the following panels (particularly at longitude 225°) we see that the enhanced column is due to ozone being transported down to low altitudes at these points. Ozone lifetime is very long here

[5]Collapsed down to the surface, one Dobson unit of ozone at is equivalent to a layer that is 0.01 mm thick at 273 K and 100 kPa.

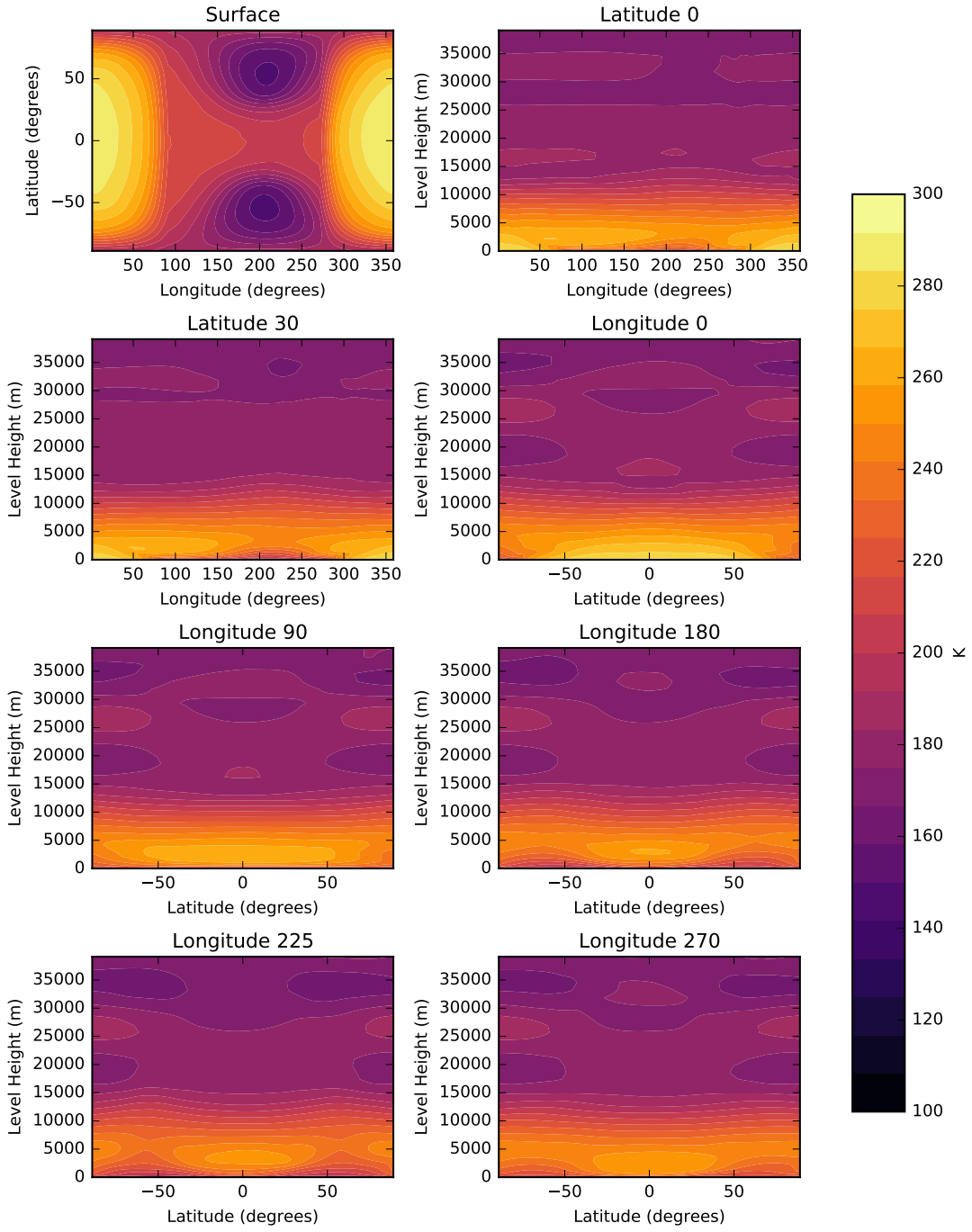

Figure 3.3: Air temperature in the simulated atmosphere. Panels show means over 120 days of model time. The top left panel shows surface temperature. Remaining panels show slices through latitudes 0°, 30° and longitudes 0°, 90°, 180°, 225° and 270°.

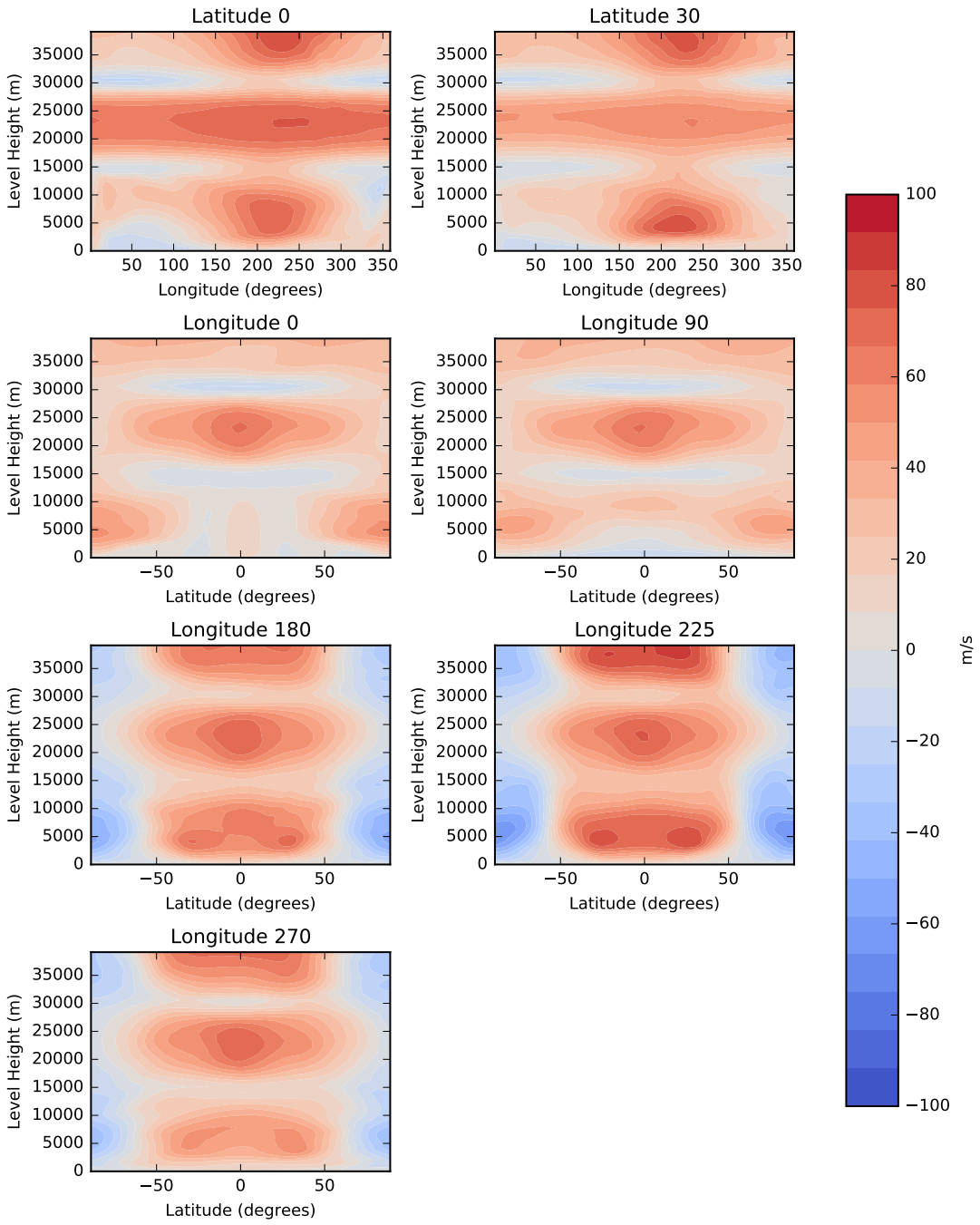

Figure 3.4: Zonal winds in the simulated atmosphere. Panels show means over 120 days of model time. Panels show slices through latitudes 0°, 30° and longitudes 0°, 90°, 180°, 225° and 270°.

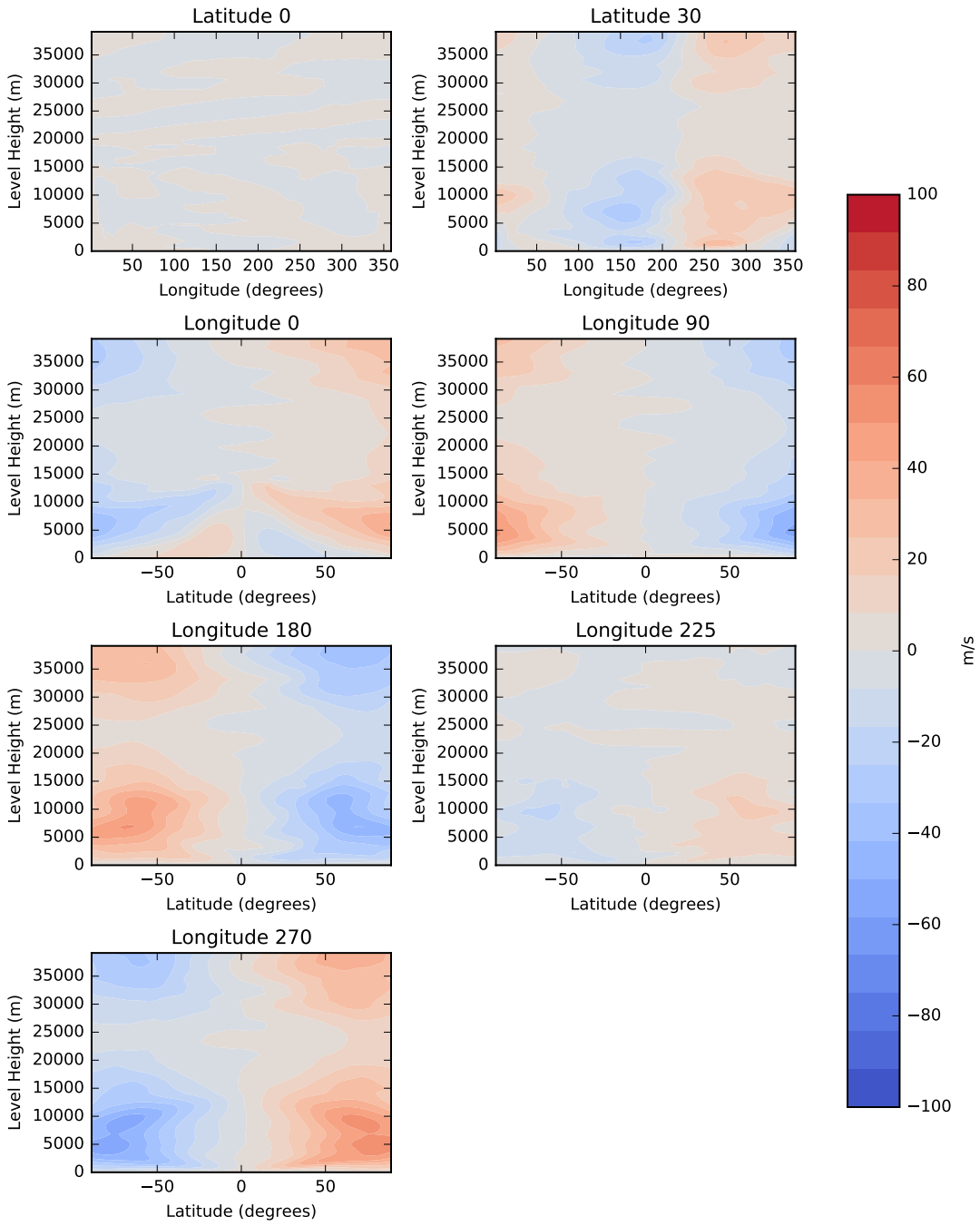

Figure 3.5: Meridional winds in the simulated atmosphere. Panels show means over 120 days of model time. Panels show slices through latitudes 0°, 30° and longitudes 0°, 90°, 180°, 225° and 270°.

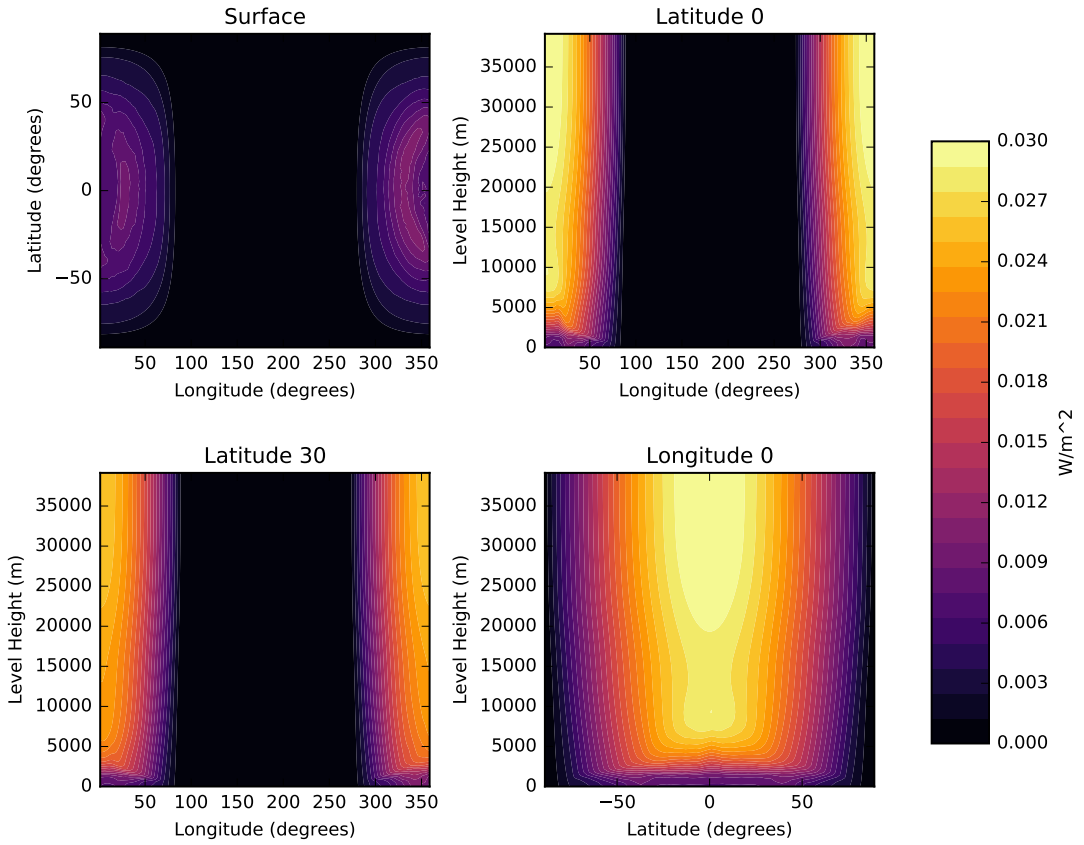

Figure 3.6: Downward UV in the simulated atmosphere. Panels show means over 120 days of model time. The top left panel shows surface UV. Remaining panels show slices through latitudes 0°, 30° and longitudes 0°. We do not show the night-side plots here as there is obviously no UV flux at these locations.

due to there being few active loss reactions. We note that ozone dry deposition is still active on the night side, which results in O_3 loss in the surface layers of the model grid. This is observable through a noticeable gradient in ozone concentration in the lowest levels of the atmosphere on both the day and night side.

Ozone columns are notably increased on the night-side and roughly around the equator at the location of the atmospheric jet. There is also an increased ozone column at the poles on the day side, which is visible at low altitudes in the longitude 0° and 90° plots. Above 40 km (not shown in figures) there is enhanced O_3 concentration on the night side of the planet. The maximum ozone column is 141 Dobson units, in the southern cold trap, and the minimum is 28 Dobson units, on the day side at latitude 55°, longitude 41°.

Concentration in the ozone layer is on the order of 1 ppm, contrasting with values in the Earth's atmosphere (10 ppm). The structure of the ozone layer is reasonably similar to that on Earth, with a broad band between 20 and 40 km, and some depletion at the poles. This is an natural consequence of our simple ozone scheme; ozone concentration is effectively determined by the availability of UV photons and number density of air, resulting in the characteristic steady-state ozone profile (Jacob, 1999).

Returning to Figure 3.2 is instructive. Naively assuming that our hemispherical averages perfectly reflect results from a pseudo-2D model, our hemispherically-averaged ozone profiles show none of the interesting structure aside from a slight increase in ozone at low altitudes. This demonstrates the importance of 3D photochemical modelling for e.g. observers; the rich structure here that could conceivably be observed is totally lost in the profiles.

3.3.4 Mixing ratios

We discuss mixing ratios of other tracer species here. We present mixing ratios of $O(^3P)$, $O(^1D)$, OH and HO_2 in Figure 3.8, Figure 3.9, Figure 3.10 and Figure 3.11 respectively. For ease of comparison we maintain the same contours in each of the above figures.

We discuss $O(^3P)$ and $O(^1D)$ first. $O(^1D)$ is the excited state of $O(^3P)$, produced through photolysis of O_3 (and rarely O_2). The two concentrations are conformal in structure with approximately 10^9 $O(^3P)$ atoms per $O(^1D)$ atom, reflecting that $O(^1D)$ is much more reactive than $O(^3P)$ and has a comparatively reduced lifetime. For both species there is little to no presence on the night side. This is expected; both atoms are produced exclusively through photolysis and are reactive, resulting in a lifetime that is too short for transport far onto the night side. There is some transport past the terminators, visible at longitudes 90° and 270°, but the transported atoms are rapidly

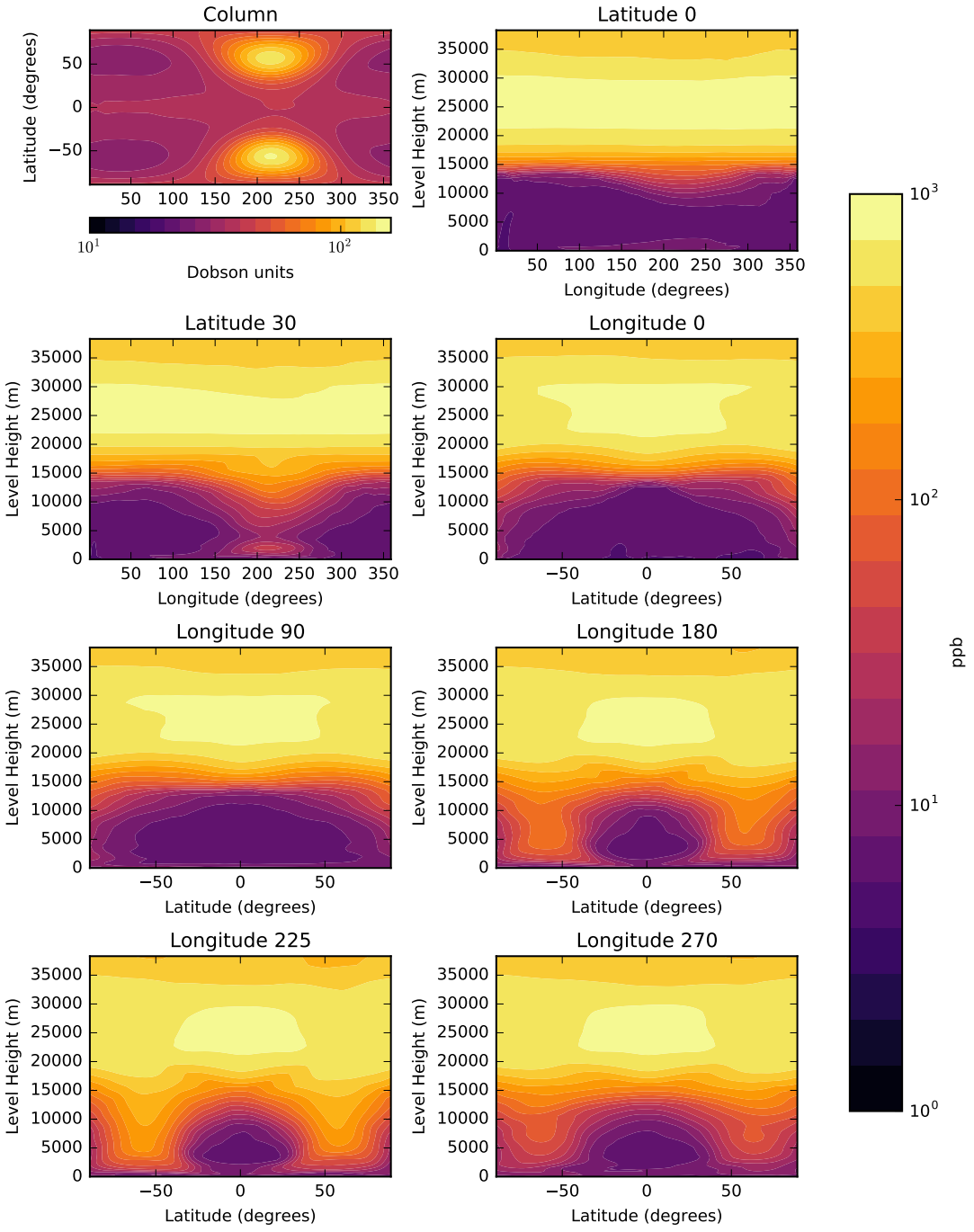

Figure 3.7: O_3 in the simulated atmosphere. Panels show means over 120 days of model time. The top left panel shows O_3 columns in Dobson units. Remaining panels show slices through latitudes 0°, 30° and longitudes 0°, 90°, 180°, 225° and 270°.

depleted as evidenced through the latitude 0° and 30° plots. From 40 km down to 15 km there is a steady gradient; below this the gradient is smaller. Concentrations roughly reflect the fluxes of fast cycling reactions R2, R3 and R4.

Comparatively, OH and HO_2 are much more well-mixed, reflecting their longer lifetimes and cyclic behaviour. There is still a notable day-night contrast, visible in the latitude plots, but concentrations are within an an order of magnitude across the terminators. The HO_x mechanism can only be initiated on the day side; however, through reaction R9, these species can be removed on the night side. Hence, at a given altitude, we see depletion of these species as they are transported across the night side (in the direction of increasing longitude).

Both species are depleted at the cold traps. We can understand this through consideration of a "young" air parcel passing through the terminator, being transported to the cold traps. The air parcel will initially contain OH and HO_2 which have been produced on the day side. Production rate of the two species on the night side is nil due to the lack of O atoms, whilst the reaction rate of R9 remains constant. Hence, over time there is exponential decay of both of these species. Simulations with inert tracers have shown that air at the cold traps is oldest of anywhere on the night side meaning this part of the atmosphere will have the lowest concentrations of these gases.

3.3.5 Reaction fluxes

We now discuss reaction fluxes. In each case we present a column reaction flux as well as reaction flux along latitude and longitude lines through the atmosphere. We maintain contours between the two fast reactions R2 and R3 (Figure 3.13 and Figure 3.14) and between all other reactions.

We discuss the Chapman mechanism first. We show fluxes for reactions R1, R2, R3 and R5 in Figure 3.12, Figure 3.13, Figure 3.14 and Figure 3.15 respectively. (Reaction flux for the de-excitation reaction R4 is not shown.)

We note firstly that reaction fluxes for all of the Chapman mechanism reactions are nil on the night side, with the only exception being the column flux for R5. This flux occurs at higher altitudes (above 40 km), where there is significant transport due to very high wind speeds and a small amount of O_3 and $O(^3P)$. Aside from this, all reactions involved short-lived species or UV photons, which are only present on the day side.

For R1 we see a flux that roughly aligns with UV flux, peaking at around 10 km at the substellar point with a reaction flux of 10 mol/s. At the terminators there is a small flux but high-energy UV photon density is low, resulting in a thousandfold decrease in reaction flux compared with longitude 0°. Between the two terminators the flux is

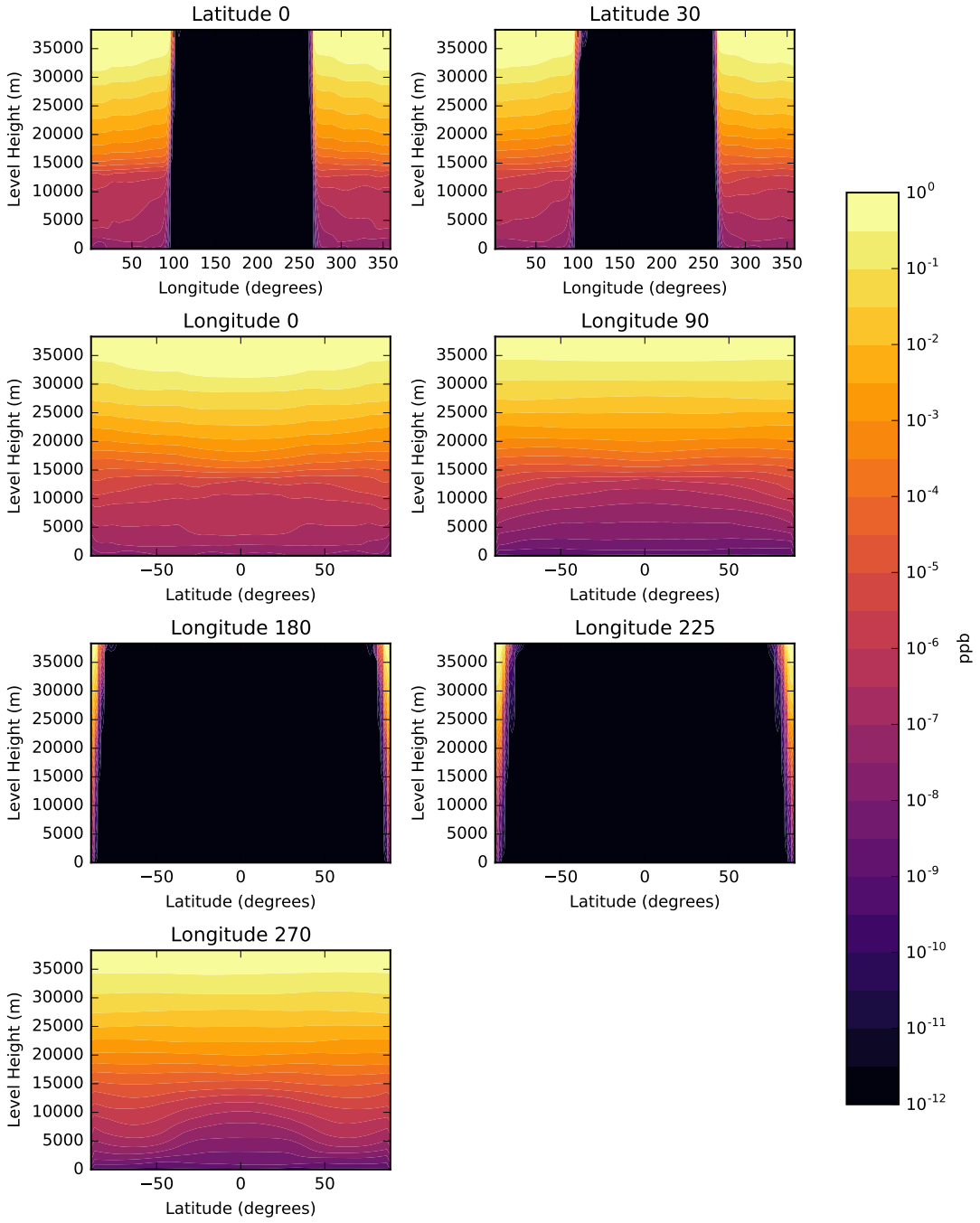

Figure 3.8: O(^{3}P) mixing ratio in the simulated atmosphere. Panels show means over 120 days of model time. Panels show slices through latitudes 0°, 30° and longitudes 0°, 90°, 180°, 225° and 270°.

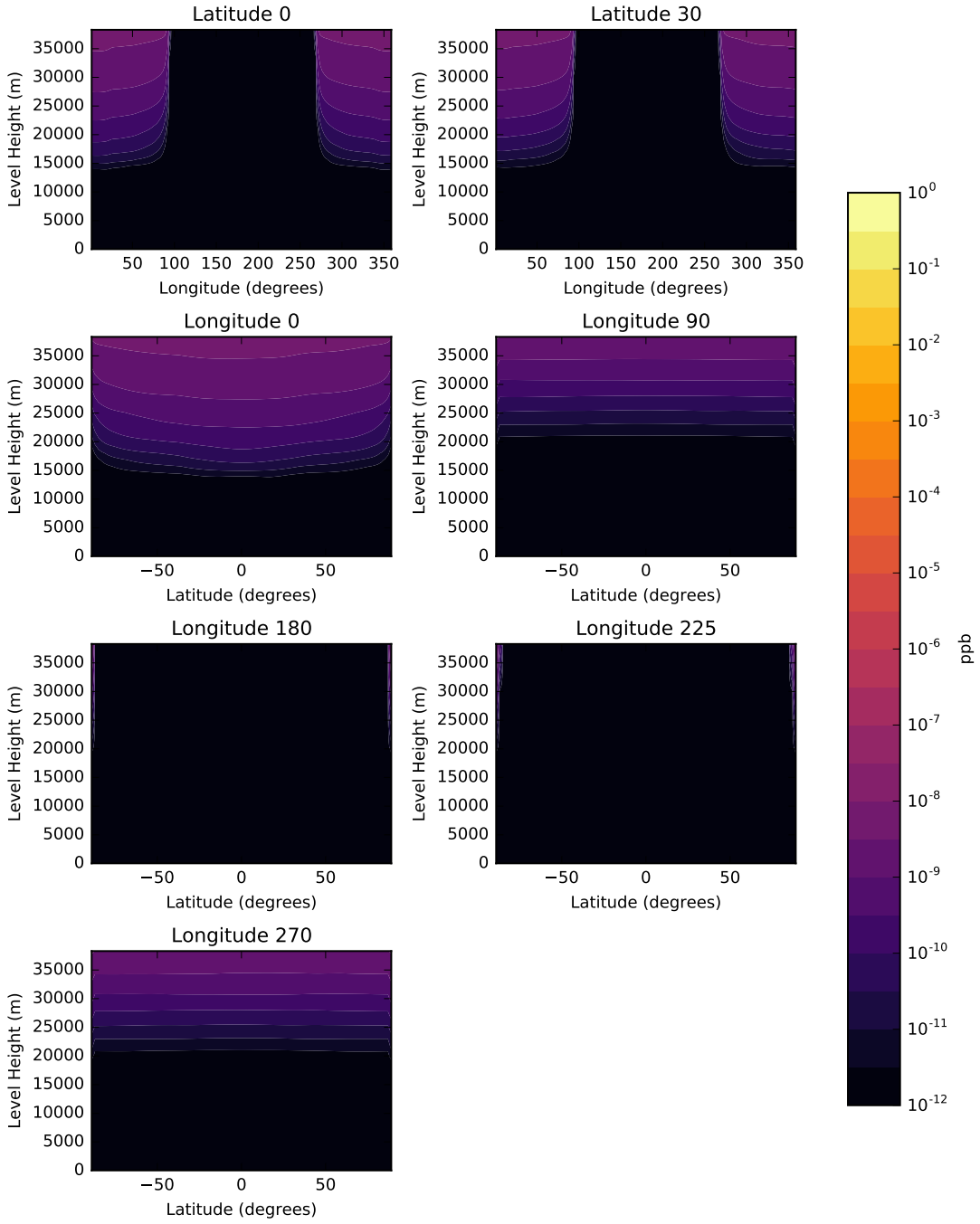

Figure 3.9: O(^{1}D) mixing ratio in the simulated atmosphere. Panels show means over 120 days of model time. Remaining panels show slices through latitudes 0°, 30° and longitudes 0°, 90°, 180°, 225° and 270°.

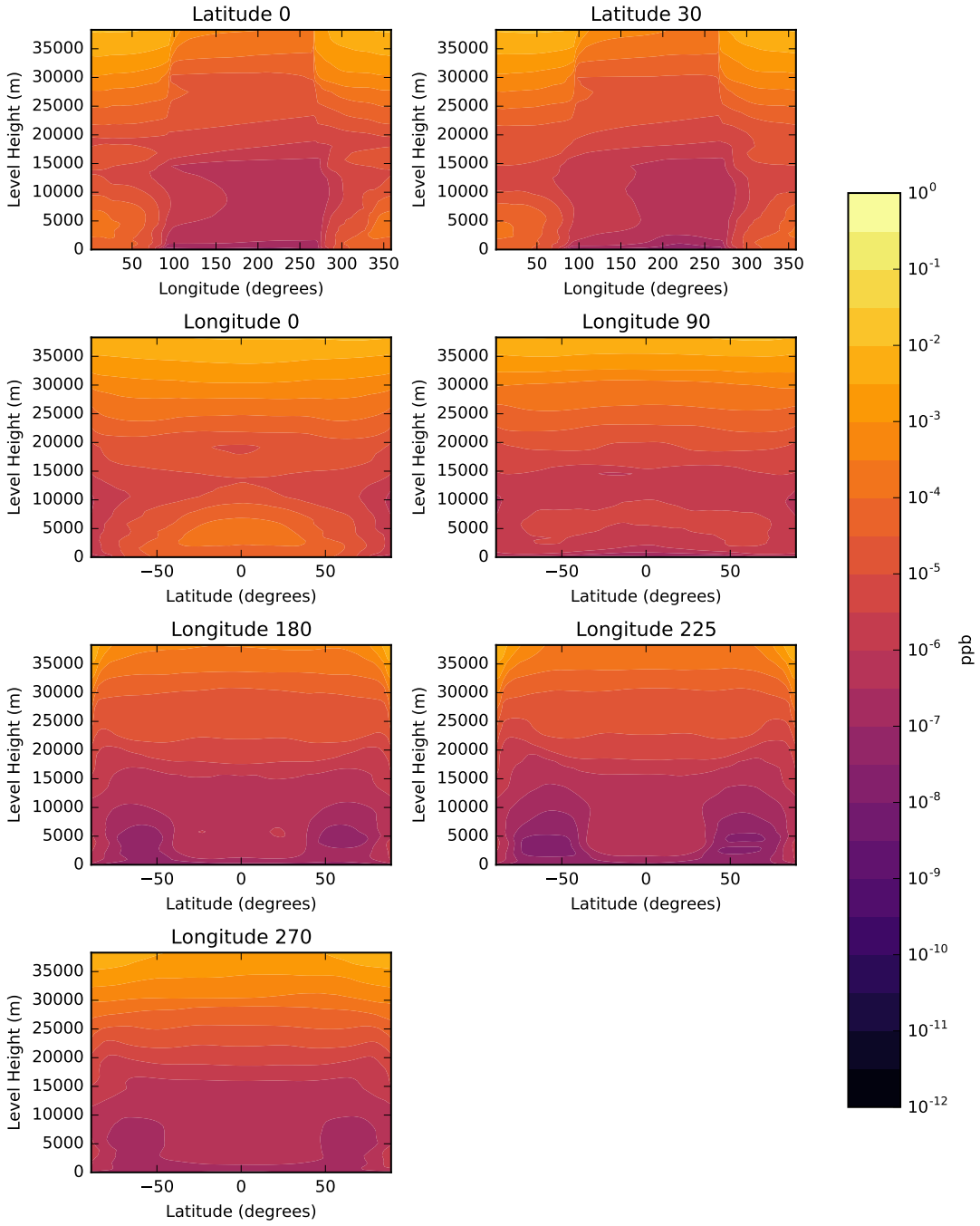

Figure 3.10: OH mixing ratio in the simulated atmosphere. Panels show means over 120 days of model time. Remaining panels show slices through latitudes 0°, 30° and longitudes 0°, 90°, 180°, 225° and 270°.

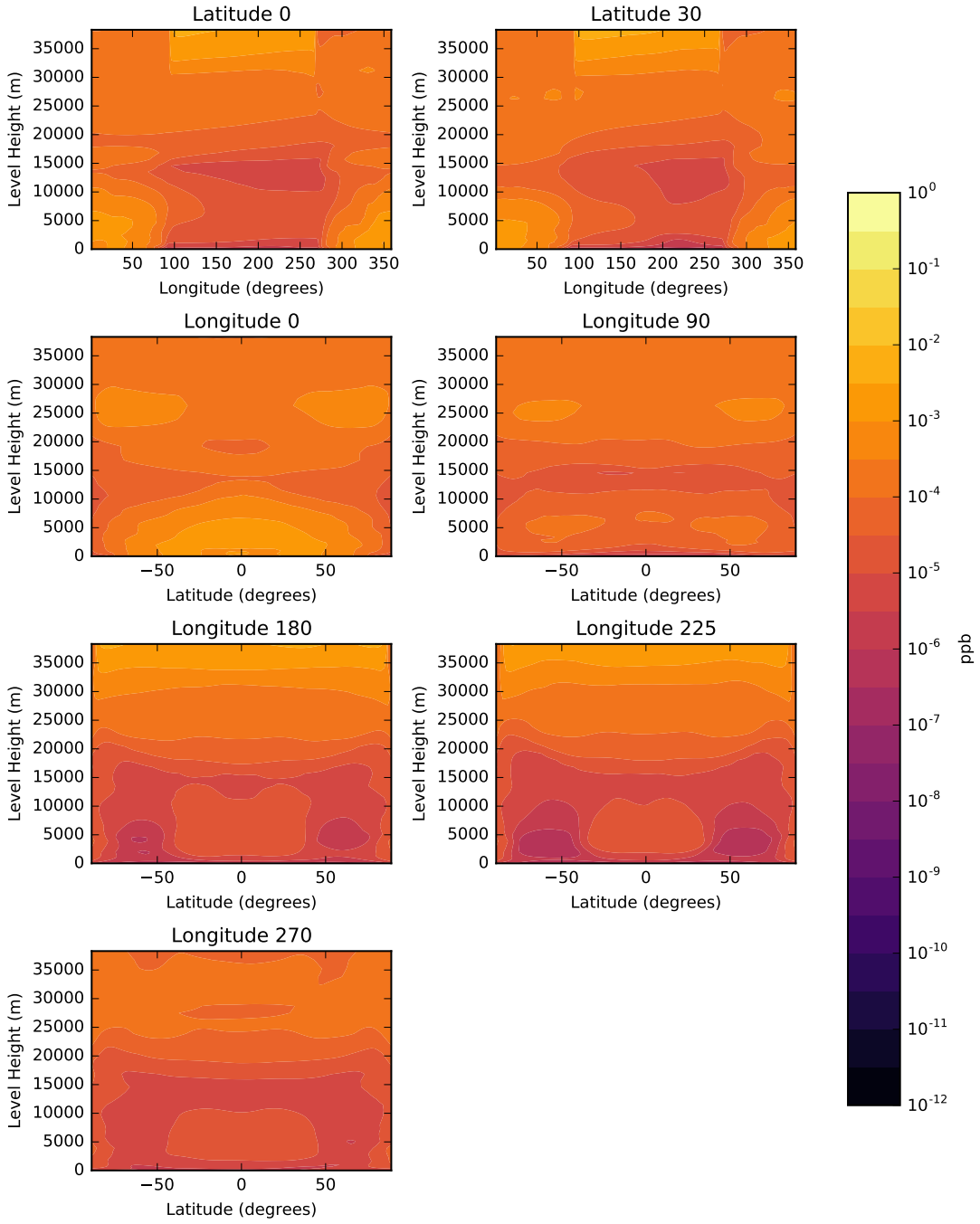

Figure 3.11: HO_2 mixing ratio in the simulated atmosphere. Panels show means over 120 days of model time. Panels show slices through latitudes 0°, 30° and longitudes 0°, 90°, 180°, 225° and 270°.

similar, with a slightly different structure at 10 km.

For the fast cycling reactions R2, R3 and R4 the structures are identical and reaction fluxes are much larger than other reactions, confirming that these cycle rapidly. Reaction flux peaks at 20 km at the substellar point, at roughly the altitude of maximum O_3 and UV photon number density. There is some flux at the terminators, and we see a similar feature to the cold trap O_3 enhancement at the 270° terminator. This aligns with O_3 concentration at the terminator in Figure 3.7. The only notable difference between the two reaction fluxes is visible in the column flux, where we see there is a small flux of R2 just past the terminator. This is $O(^3P)$ that has been transported to the night side, which quickly reacts with any available O_2 molecule. R3 cannot occur on the night side due to the lack of photons, explaining the discrepancy. Looking to Figure 3.15 we see that R5 shows similar features to R2 and R3, albeit with a reaction flux around five orders of magnitude lower.

Comparing R3 flux with R1 flux at the terminator indicates some differences; R1 occurs at much higher altitudes with very low flux below 30 km, in contrast with R3, which peaks at $15 - 20$ km. We attribute this to the fact that R1 requires a much more energetic photon, which is less able to penetrate through the atmosphere at low intensity and indirect (approaching 90°) angles. However, the model output only contains broadband UV, so we are unable to probe further here.

We now discuss the HO_x reactions. Figure 3.16 shows the initiation of the HO_x chain of reactions. We note firstly that reaction fluxes are for R7 and R8 are significantly larger than reaction fluxes for R6 and R9 throughout the atmosphere (with the exception of the substellar point). This indicates that each OH molecule produced through R6 will undergo the O_3 destruction/HO_2 production cycle many times before being converted back to O_2 and H_2O. Comparing with reaction flux of R9, we estimate that an OH molecule will undergo of order 1000 $HO_2 \leftrightarrow$ OH conversions before being removed through R9.

Comparing with the previous set of reactions, the relative lack of structure across altitudes and between the day and night side of the R7, R8 and R9 fluxes indicates the longer lifetimes of these reactants. R6 by contrast shows sharp structure and altitude dependence reflecting the limited availability of short-lived $O(^1D)$. For the latter reaction, at the substellar point above around 15 km there is a major drop in reaction flux. This is due to an incorrectly-set mask in the model code, and is not a real feature in the model.

In the reaction flux columns we clearly see gradual night side depletion of OH and HO_2 through R9. In the latitude plots we also see the increased reaction fluxes at $20 - 25$km, reflecting the fast transport in the atmospheric jets at this altitude. At $10 - 15$ km, where transport is very slow, the species are depleted much more rapidly.

Comparing R7 and R8 with R9 at the cold traps, we see relatively little structure in the former and a significant reduction in the latter. From Figure 3.7 we know there is a major O_3 enhancement at this point and from Figure 3.10 and Figure 3.11 we know that OH and HO_2 are depleted. Reaction rates depend on the concentration of reactants multiplicatively, hence a tenfold enhancement of O_3 and a tenfold reduction of OH (for example) results in the same reaction rate. By contrast, both reactants for R9 are depleted, resulting in a quadratic reduction in flux.

For all reactions in the HO_x mechanism there is significant enhancement at the substellar point. This simply reflects the (relatively) high UV and humidity at this location.

3.3.6 Ozone lifetime

We calculate O_3 lifetimes in the simulated atmosphere by dividing O_3 burden in a given model grid box by the loss reaction fluxes in that grid box. We note here that transport and diffusion are much faster than lifetimes at many points in the atmosphere. Thus, a given ozone molecule on the night side will not persist for its full chemical lifetime of 10000 years; rather it will eventually reach the day side or surface and be destroyed. We discuss this further below.

In Figure 3.20 we depict O_3 lifetime against each of the three loss mechanisms: the Chapman mechanism (loss through R5), the HO_x cycle (loss through R7 and R8) and deposition. Our model predicts that atmospheric ozone loss is dominated by loss through the HO_x mechanism (with the exception of the surface layer), as the net lifetime tracks HO_x lifetime very closely. This aligns with calculations for the Earth, where the Chapman mechanism famously over-predicted stratospheric ozone concentration and the HO_x mechanism was discovered to be a significant sink in the Earth's stratosphere (Jacob, 1999).

We find that ozone lifetime on the night side of the planet is significantly longer than lifetime on the day side, but on both sides of the planet the (mean) chemical lifetime is hundreds of years increasing to as much as 10000 years at the cold trap latitudes on the night side. We see a sharp increase in ozone lifetime at the terminators, indicating the rapid decrease in UV photon and free O atom abundance (depicted in Figure 3.6, Figure 3.8 and Figure 3.9), and a steady increase across the night side indicating the gradual depletion of OH and HO_2.

The simulations show that deposition is significantly faster than any of the other loss mechanisms. In the surface layer net lifetime matches deposition lifetime as the other reactions become insignificant. Deposition lifetime is uniform across the planetary surface.

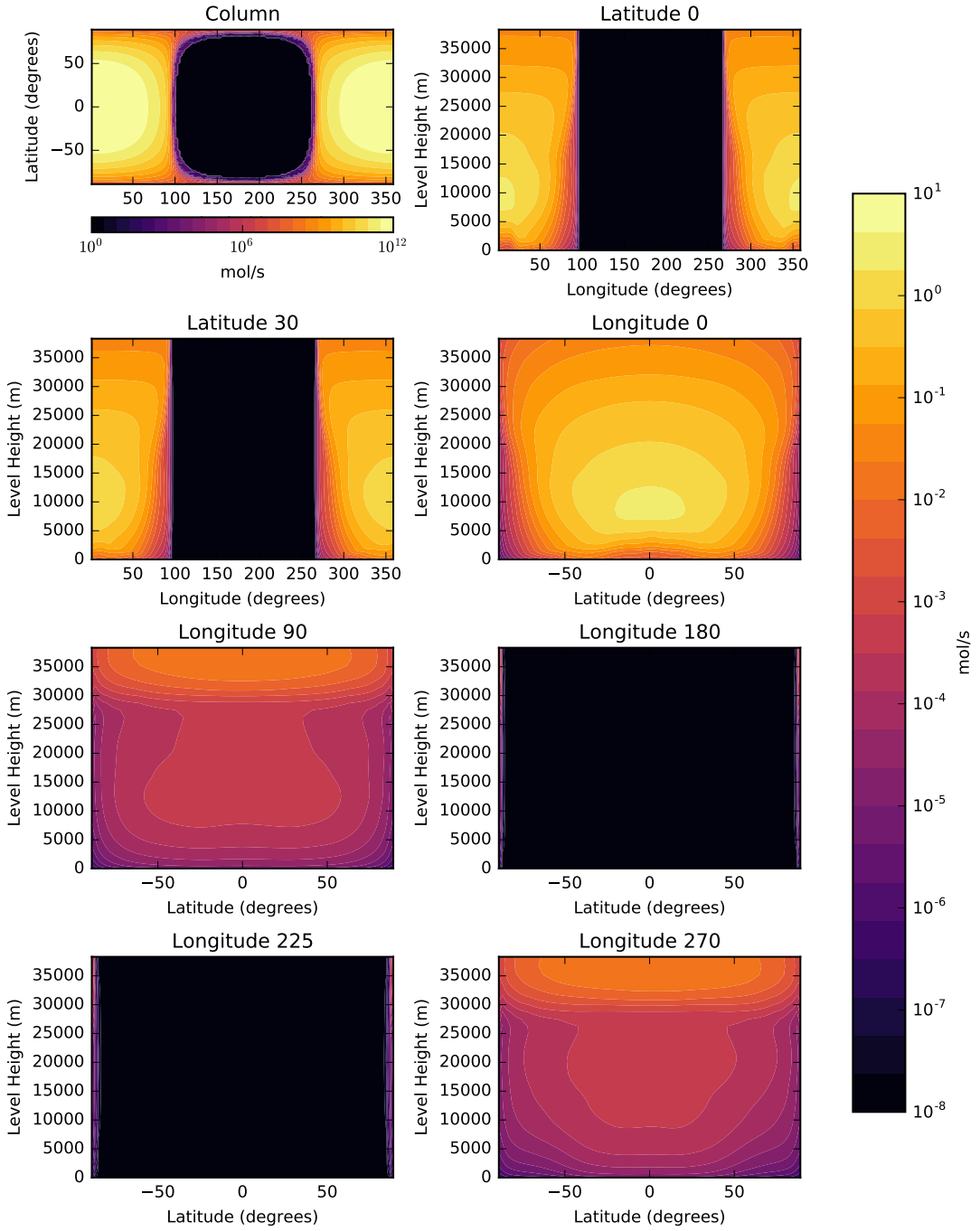

Figure 3.12: Flux for R1 from the Chapman mechanism in the simulated atmosphere. Panels show means over 120 days of model time. The top left panel shows a column through the atmosphere. Remaining panels show slices through latitudes 0°, 30° and longitudes 0°, 90°, 180°, 225° and 270°. Scales are matched to all other slow reactions.

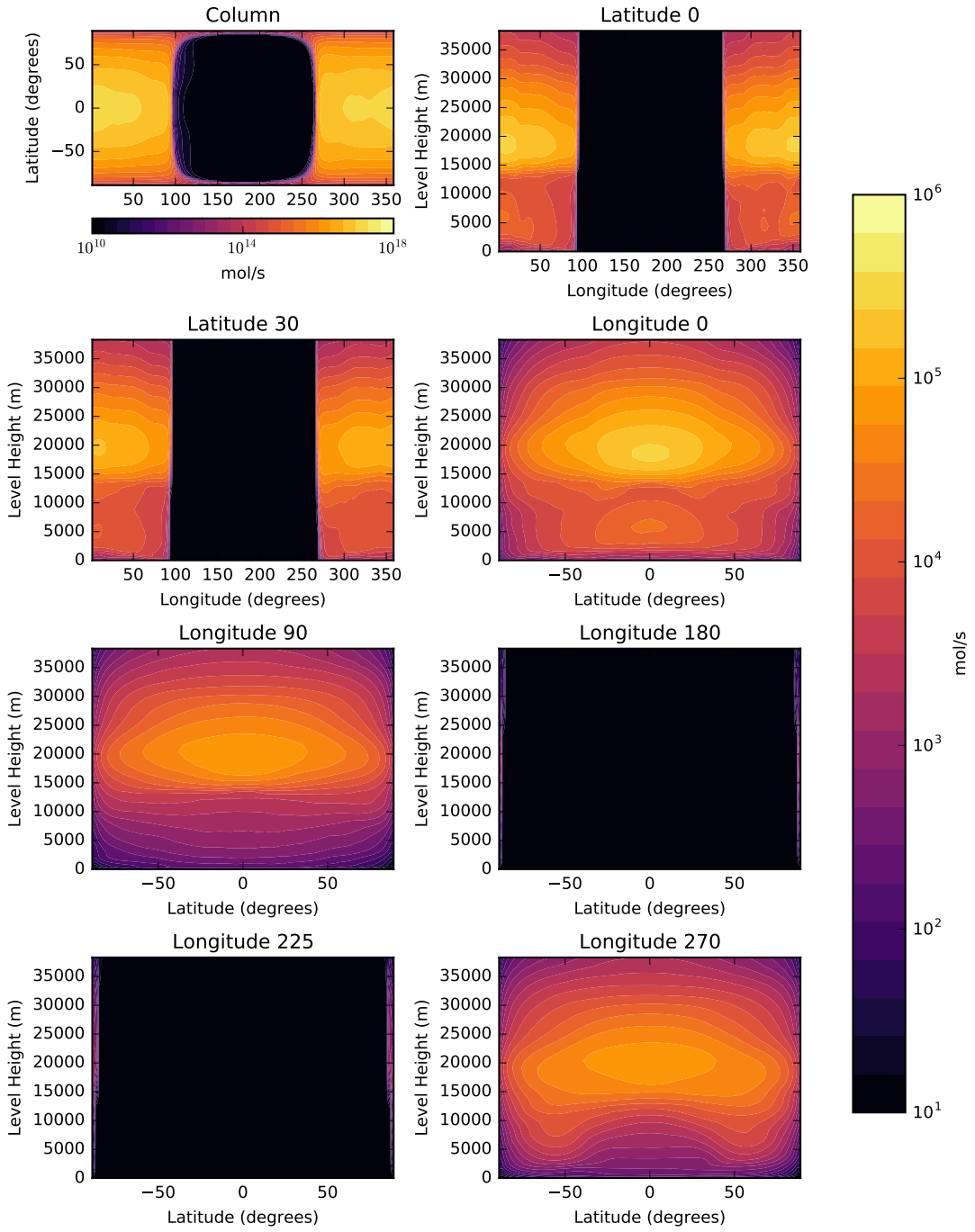

Figure 3.13: Flux for R2 from the Chapman mechanism in the simulated atmosphere. Panels show means over 120 days of model time. The top left panel shows a column through the atmosphere. Remaining panels show slices through latitudes 0°, 30° and longitudes 0°, 90°, 180°, 225° and 270°. Scales match the other fast reaction, Figure 3.14.

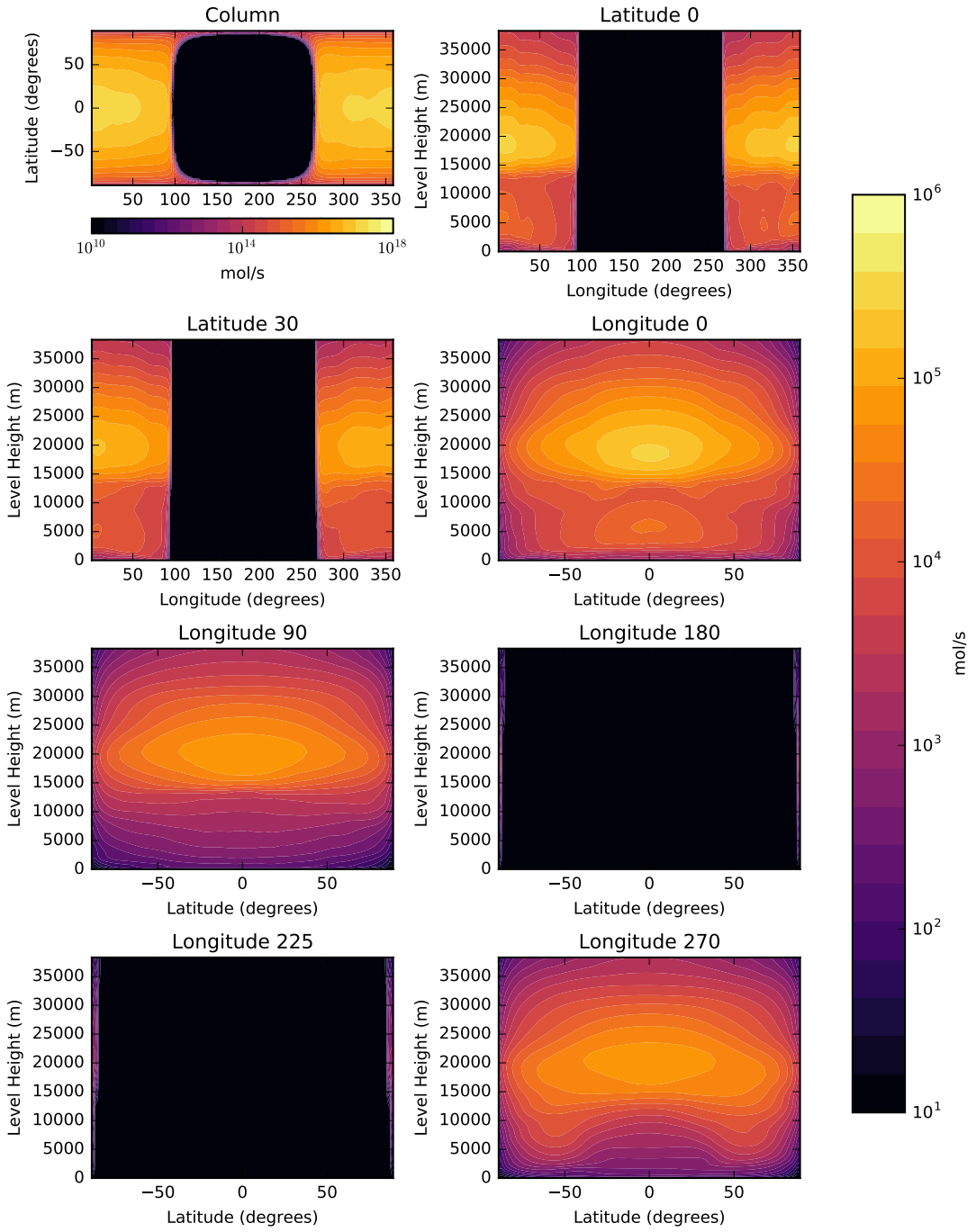

Figure 3.14: Flux for R3 from the Chapman mechanism in the simulated atmosphere. Panels show means over 120 days of model time. The top left panel shows a column through the atmosphere. Remaining panels show slices through latitudes 0°, 30° and longitudes 0°, 90°, 180°, 225° and 270°. Scales match the other fast reaction, Figure 3.13.

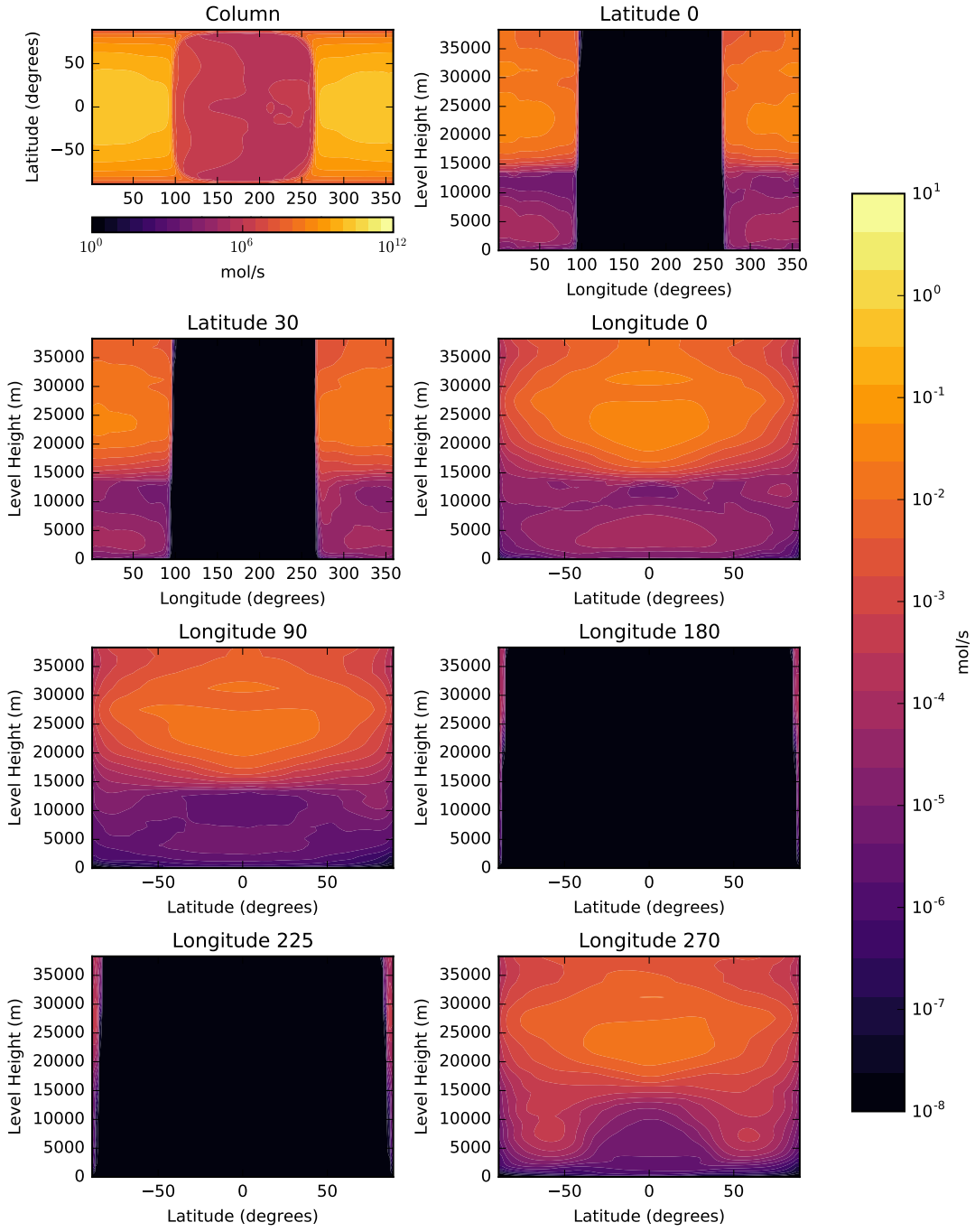

Figure 3.15: Flux for R5 in the simulated atmosphere. Panels show means over 120 days of model time. The top left panel shows a column through the atmosphere. Remaining panels show slices through latitudes 0°, 30° and longitudes 0°, 90°, 180°, 225° and 270°.

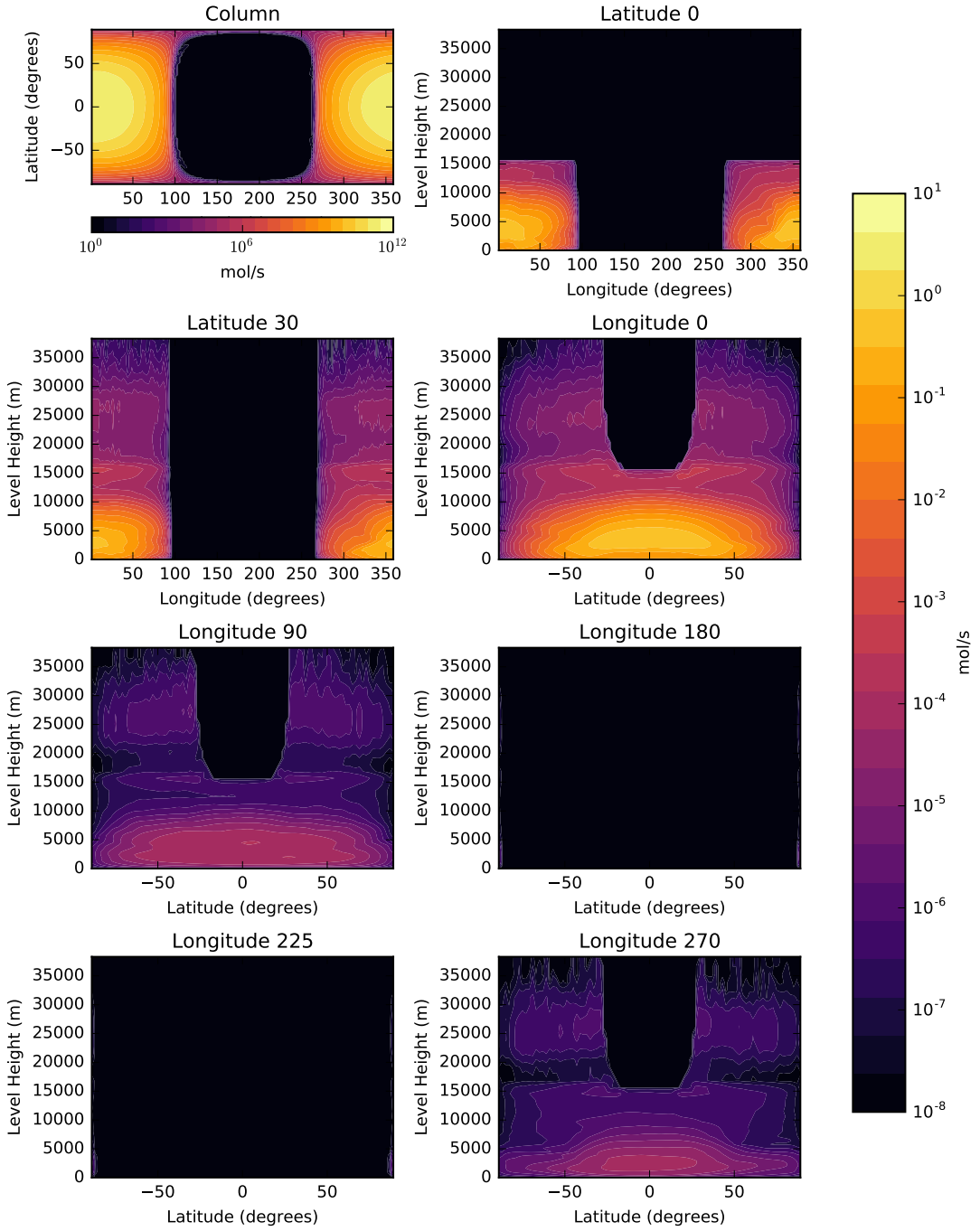

Figure 3.16: Flux for R6 from the HO_x mechanism in the simulated atmosphere. Panels show means over 120 days of model time. The top left panel shows a column through the atmosphere. Remaining panels show slices through latitudes 0°, 30° and longitudes 0°, 90°, 180°, 225° and 270°. Scales are matched to all other slow reactions.

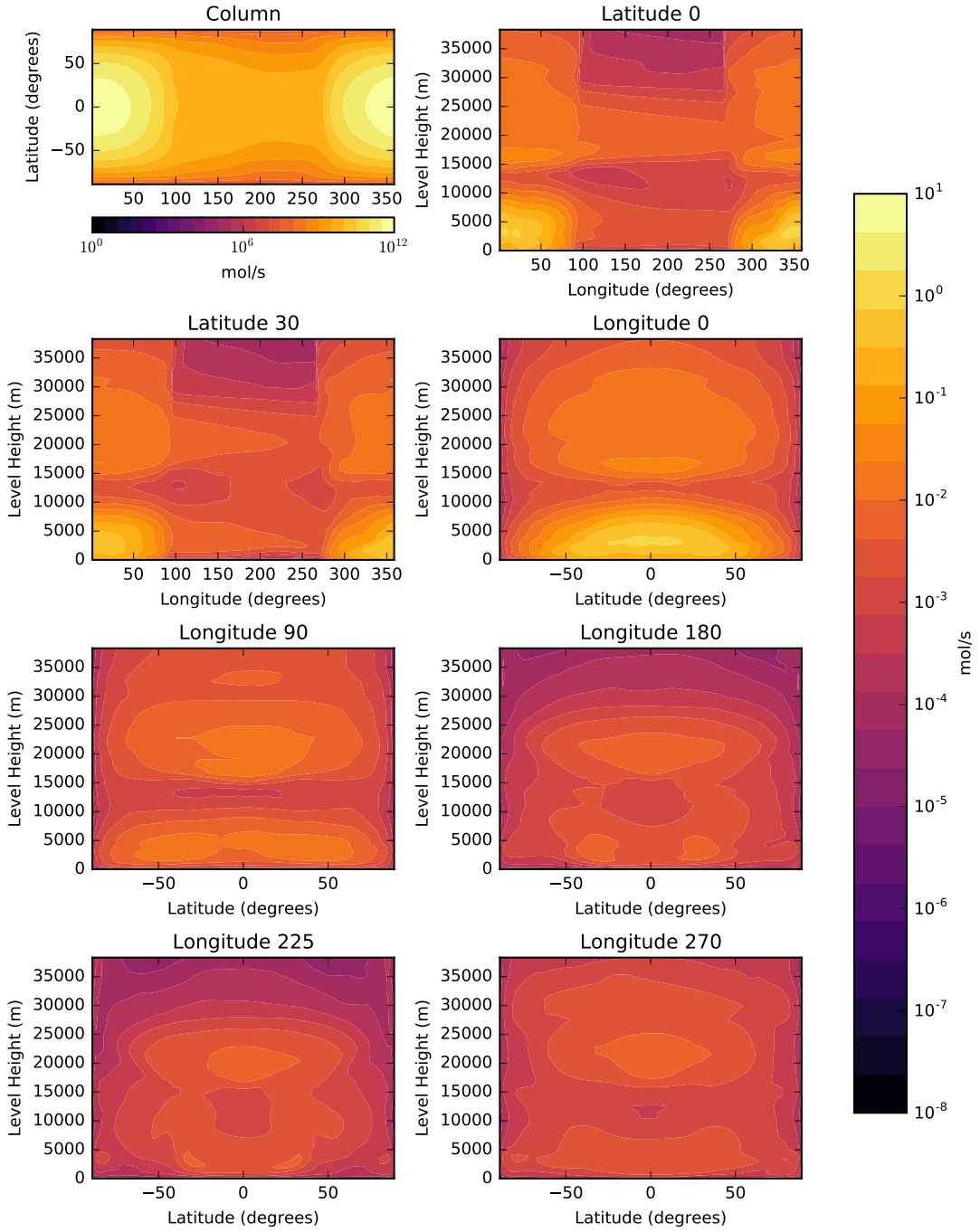

Figure 3.17: Flux for R7 from the HO_x mechanism in the simulated atmosphere. Panels show means over 120 days of model time. The top left panel shows a column through the atmosphere. Remaining panels show slices through latitudes 0°, 30° and longitudes 0°, 90°, 180°, 225° and 270°. Scales are matched to all other slow reactions.

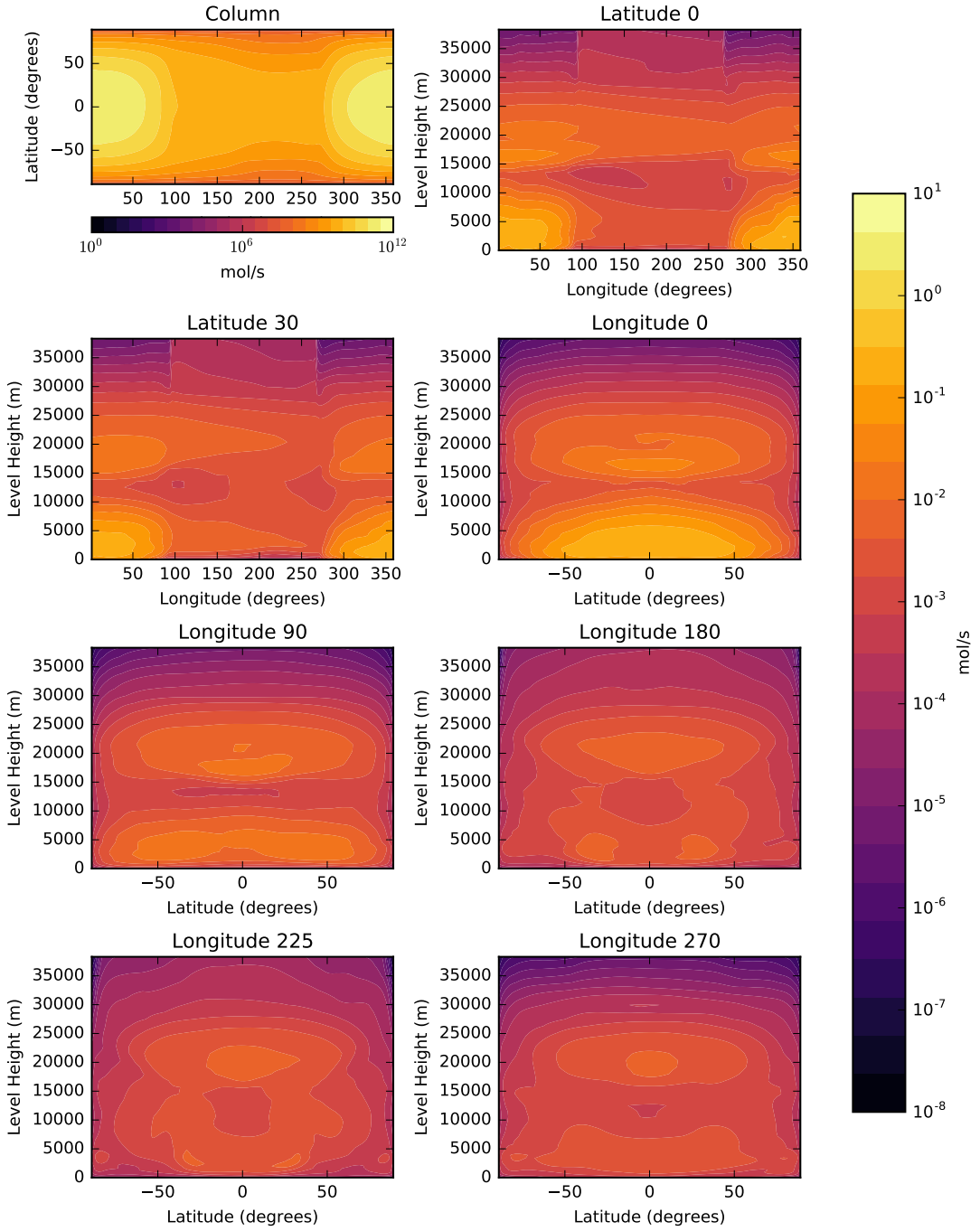

Figure 3.18: Flux for R8 from the HO_x mechanism in the simulated atmosphere. Panels show means over 120 days of model time. The top left panel shows a column through the atmosphere. Remaining panels show slices through latitudes 0°, 30° and longitudes 0°, 90°, 180°, 225° and 270°. Scales are matched to all other slow reactions.

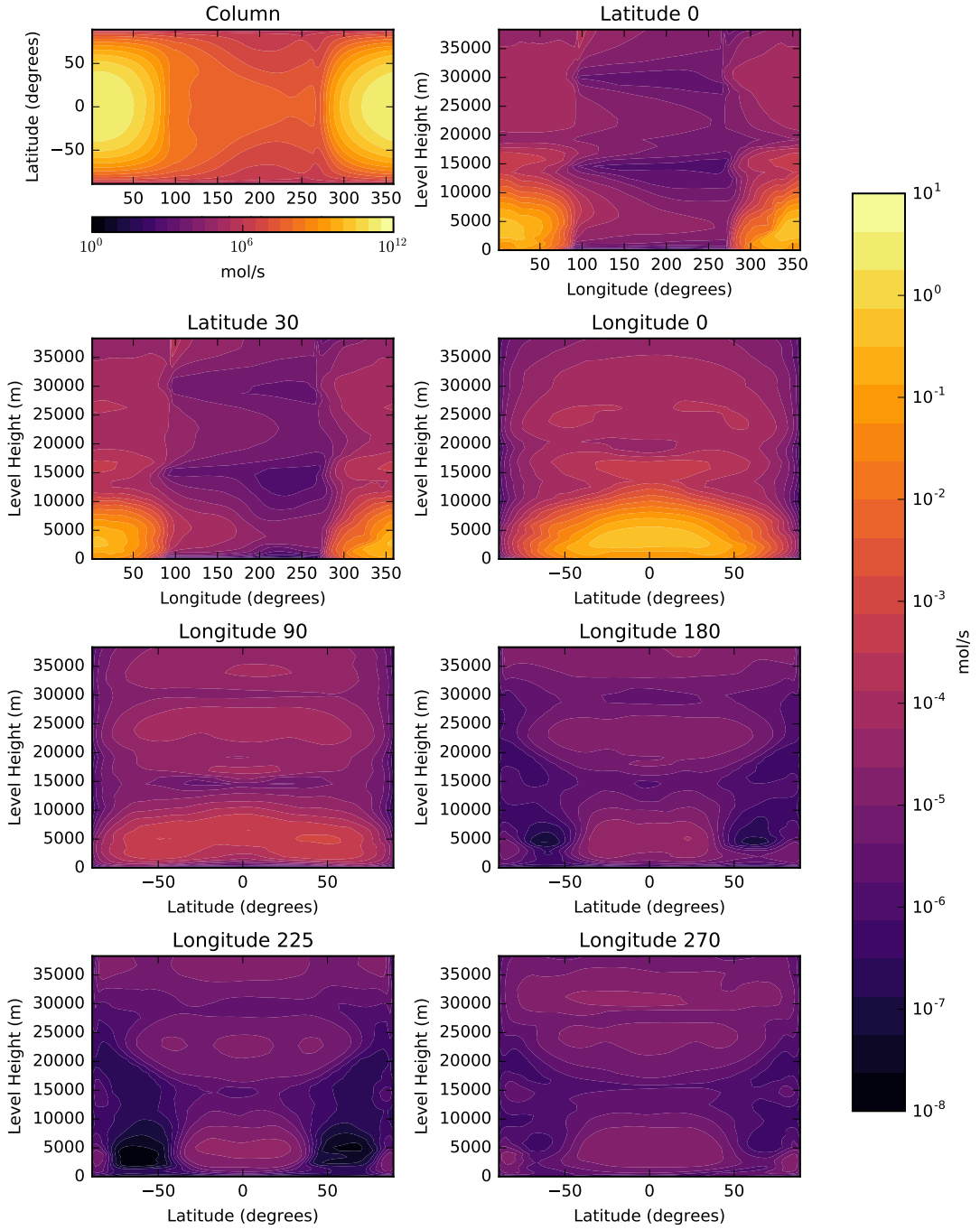

Figure 3.19: Flux for R9 from the HO_x mechanism in the simulated atmosphere. Panels show means over 120 days of model time. The top left panel shows a column through the atmosphere. Remaining panels show slices through latitudes 0°, 30° and longitudes 0°, 90°, 180°, 225° and 270°. Scales are matched to all other slow reactions.

In Figure 3.21 we show net ozone lifetime in more detail. We see a clear day-night boundary, with the shortest lifetime at the substellar point. Ozone loss at this point occurs mainly through R7 and R8 (as seen in Figure 3.17 and Figure 3.18) but burden is low, resulting in a short lifetime. The atmospheric jet at $20 - 25$ km is also clearly visible in the top two plots, as is the stable atmospheric layer at 15 km. In the plot at 225° we see the extremely long lifetime at the cold traps, exceeding 10^5 years, explaining the accumulation of ozone at low altitudes.

To gain a further understanding of the importance of transport, we calculate a "transport lifetime" for each grid box. This is calculated by dividing the grid box dimensions by corresponding wind speeds. Thus, if a grid box has a transport lifetime of an hour, a parcel of air entering the box will exit on the far side of the box in approximately one hour. (The model grid is described in subsection 3.2.3, but zonal and meridional box dimensions are on the order of a few hundred km.)

We caution here that our calculated transport lifetime does not account for vortices and other large-scale atmospheric features, such as those at the cold traps, that would cause a given air parcel to circle through several grid boxes before returning to the same point. A full study of atmospheric circulation, using inert tracers, emissions and age of air, would be a sensible next step for this model.

We show transport lifetime in Figure 3.22. In the figures we clearly see the atmospheric jet, where transport lifetime is on the order of a few hours. Given that there are 144 longitudinal grid boxes, we estimate that at latitude 0° a parcel of air will travel around the equator in a period between a few days and one month. The stable layer at 15 km is also visible here. On the night side we see that transport is generally quicker than on the day side, with fewer highly stable points, aligning with the increased windspeeds visible in Figure 3.4 and Figure 3.5.

The cold traps are visible in the section through longitude 225°, but the effect here is not as exaggerated as in the chemical lifetime. As noted above the transport here is slower than depicted, due to a vortex-like structure described in subsection 3.3.2.

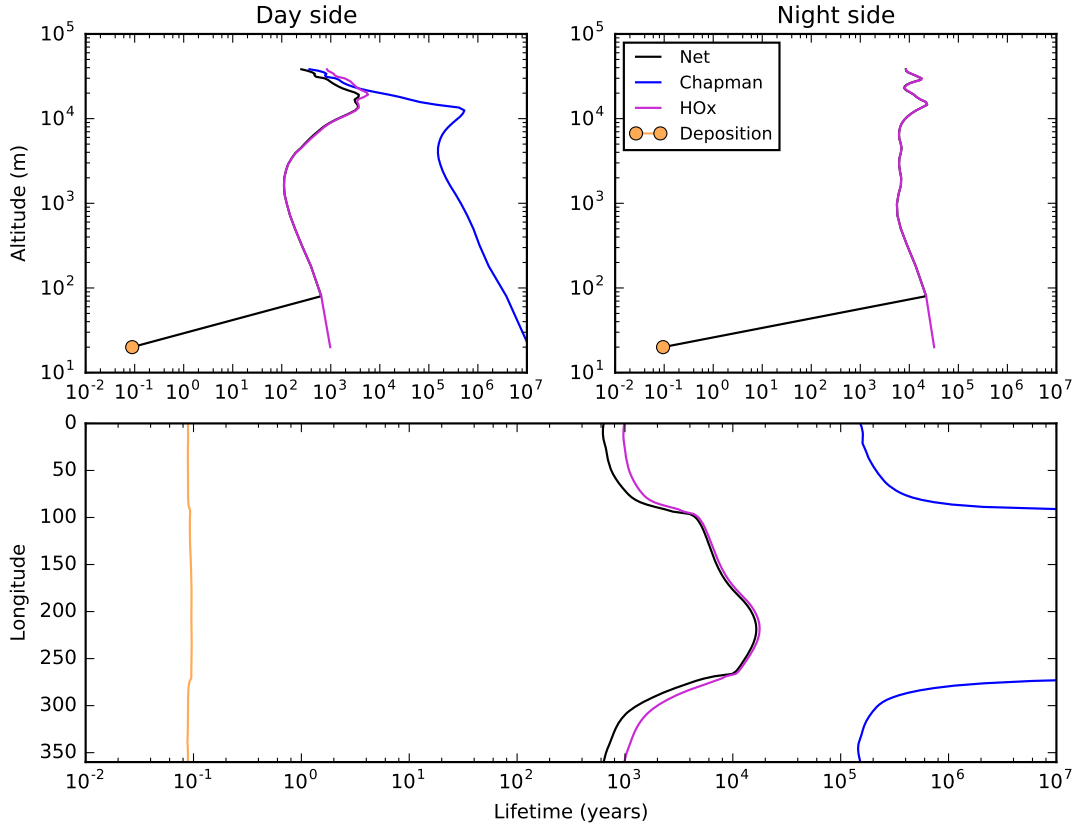

Figure 3.20: O_3 lifetime partitioning between the three loss mechanisms. The top two plots show hemispherical means for the day and night side respectively. As deposition occurs only in the surface layer it is depicted as a point rather than a line in the altitude plots. Chapman lifetime is extremely long on the night side and therefore is not depicted in the top right plot. The lower plot shows meridianally and vertically averaged lifetime against longitude.

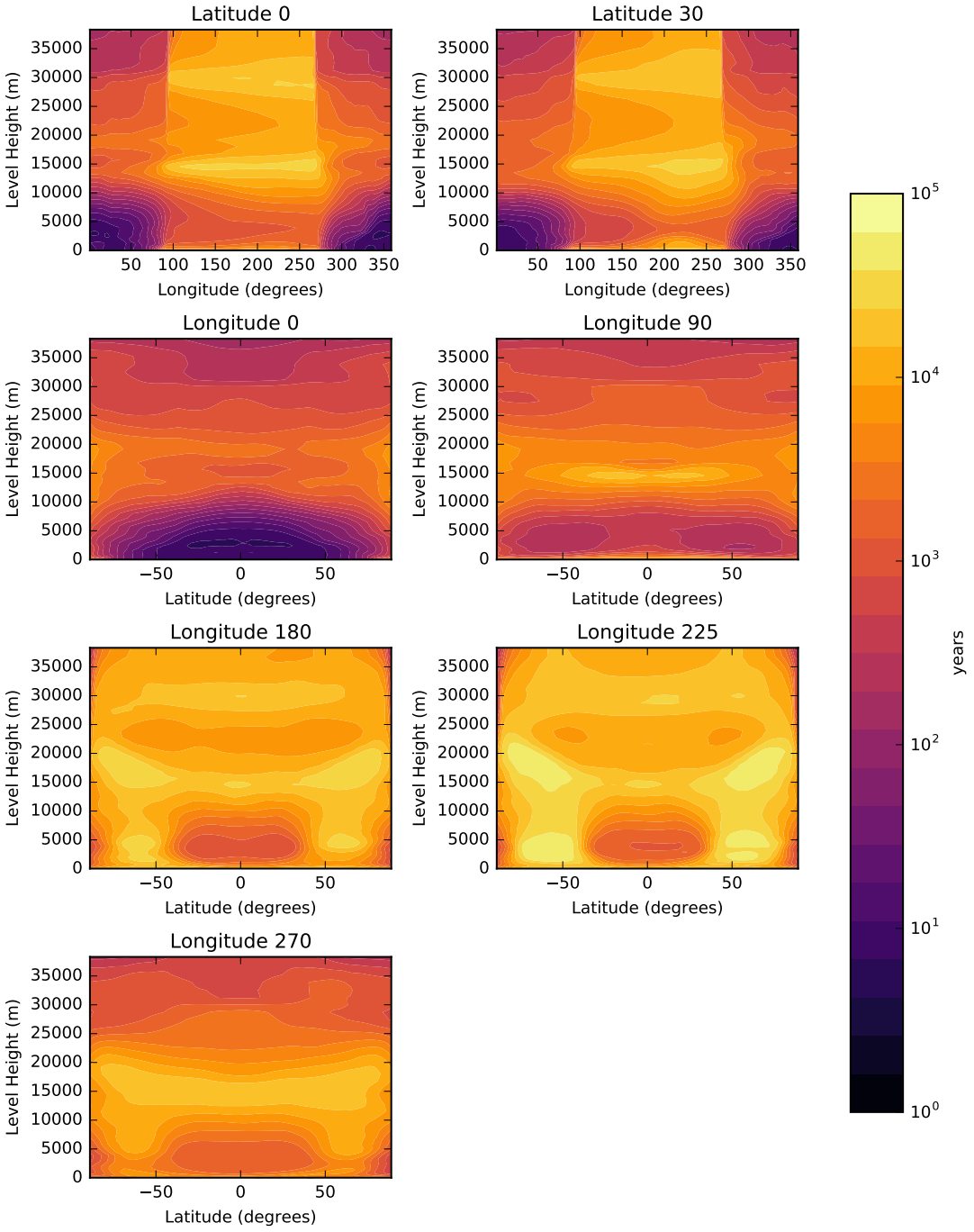

Figure 3.21: Net O_3 lifetime. Panels show means over 120 days of model time. Panels show slices through latitudes 0°, 30° and longitudes 0°, 90°, 180°, 225° and 270°.

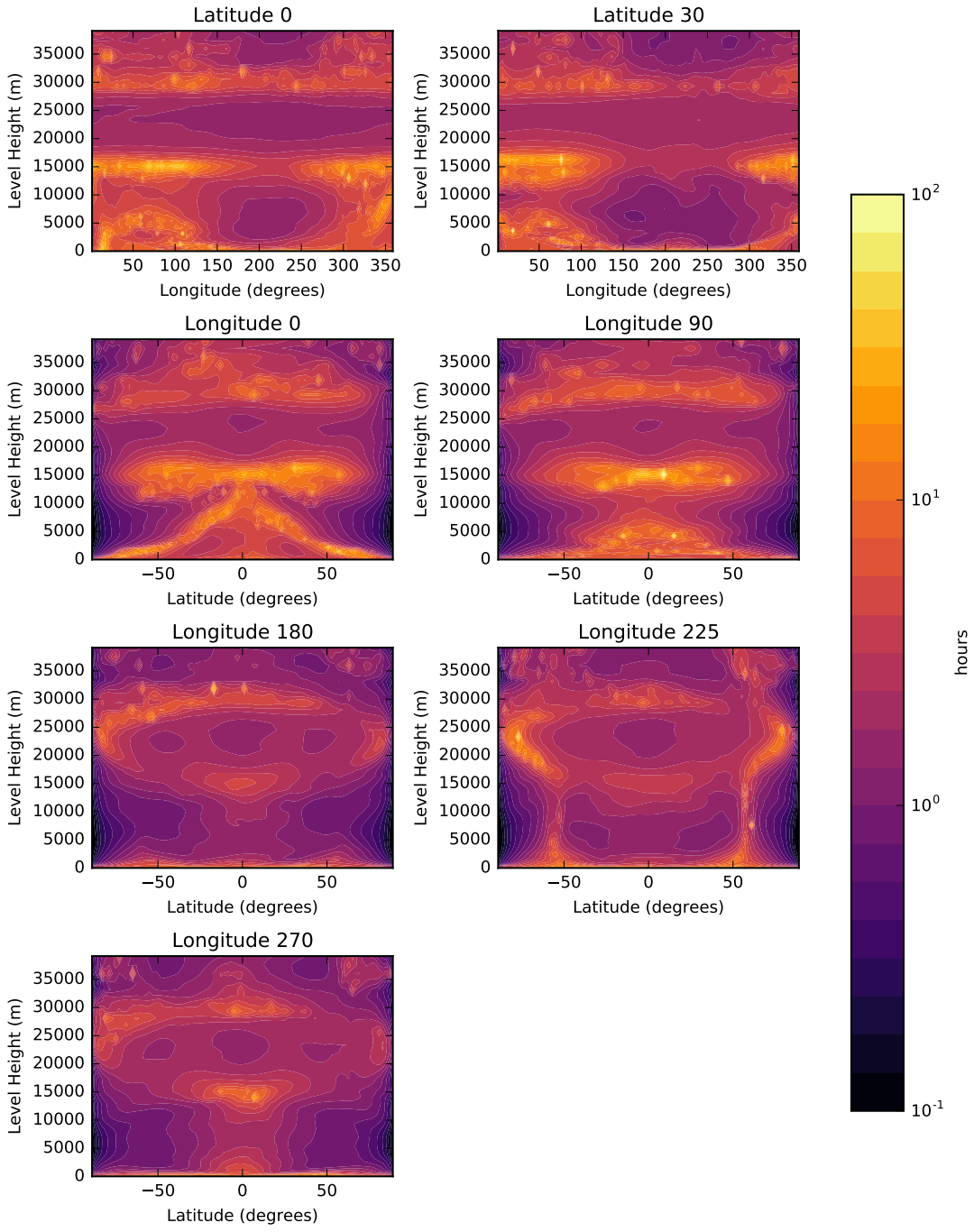

Figure 3.22: Transport "lifetime" for each grid box in the atmosphere. Panels show means over 120 days of model time. Panels show slices through latitudes 0°, 30° and longitudes 0°, 90°, 180°, 225° and 270°.

3.4 Discussion

We now have a complete picture of atmospheric ozone on our simulated planet. Briefly, it is produced on the day side at $20 - 25$ km, whereupon it is transported to the night side. Here the chemical lifetime is extremely long, due to the lack of any significant loss mechanism, so ozone accumulates over a period of years. There is a particular concentration of ozone at the cold traps, where day-to-night transport is too slow for significant concentrations of OH and HO_2. Ozone is lost overwhelmingly through the HO_x mechanism, with the exception of the planetary surface, where deposition dominates.

3.4.1 Comparison with Boutle et al. (2017)

Our simulation results are mostly consistent with Paper I. We first reiterate the major differences between our models:

- We have reduced the model timestep from 20 minutes to 12, though this should not affect the results significantly.
- We have increased the model top to around 80 km.
- We are using online chemistry, of particular relevance in the case of ozone. In the Paper I model the ozone layer is a prescribed Earth-like layer; thus our ozone layer is around 10 times thinner, with a different profile.
- In our model, water vapour is removed from the atmosphere through the HO_x cycle, rather than just through precipitation.
- We have removed some radiatively active background greenhouse gases (GHGs). These are N_2O and CH_4, with MMRs of approximately 5×10^{-7} and 1×10^{-6} respectively. (Our model still contains CO_2.)
- Removing CH_4 switches off the methane oxidation parameterisation, which produces water vapour in line with methane abundance.

We note a few key differences in the model output. We reproduce their Figure 5, with the same axis scaling for comparison, in Figure 3.23. The top of our atmosphere (above 15 km) is colder, ranging from 170 K to 185 K with a small lapse rate compared to their atmosphere which is a fairly even 185 K on both the day and night side, showing no major vertical trend. Further, our maximum and minimum surface temperatures are different, at 287 K and 147 K respectively compared with 290 K and 150 K in

Paper I. Finally, humidity is lower throughout the atmosphere, but especially above 15 km. We discuss some of the possible differences below.

Firstly, we have removed some background greenhouse gases (GHGs) that cause heating in atmosphere. Based on experiments performed in subsection 4.2.1, we expect that these GHGs heat the upper atmosphere by a few K up to as much as 10 K. Lower in the atmosphere the impact is minimal. In Paper I, their nitrogen-dominated planet (that does not include the background GHGs, O_2 or O_3) has a lower upper atmosphere temperature than their Earth-like atmosphere, with the difference in temperature being a fairly even 10 K. In subsection 4.2.1 we find the reduction in ozone column from an Earth-like ozone layer to the M-dwarf layer (as calculated by the online chemistry) causes around 5 K cooling in the upper atmosphere. Ozone acts as a GHG, and therefore the smaller ozone column will result in less absorption at $10 - 40$ km, explaining this cooling. To first order it appears the remaining $5 - 10$ K of heating is provided by the background GHGs.

However, we note that our atmosphere is cooler than even their nitrogen-dominated atmosphere, which also lacks GHGs. Clearly, unless the boundary condition at the top of the atmosphere is exactly correct, extending the model top to 85 km will impact the 40 km layer of the atmosphere. It appears that this extension of the atmosphere, along with the removal of the GHGs causes the 40 km layer to cool by at least 10 K. A model run with GHGs included and no chemistry would allow the isolation of the effects of increasing the model top and removing GHGs.

Our model also has lower humidity above 10 km, by an order of magnitude at 20 km and by a few times at 40 km and at the surface. Water vapour is a GHG that is particularly important in the case of an M-dwarf planet with significant IR irradiance (where water is a strong absorber); a smaller water vapour column results in less radiative heating in the atmosphere. Furthermore, humidity is naturally a significant factor in cloud formation, which presents one of the most important sources of both heating (through long-wave absorption and downward re-radiation) and cooling (through short-wave reflectance) in a planetary atmosphere.

In our model, water vapour is removed from the atmosphere through R6 (and at a later stage added back into the atmosphere through R9). In a steady state, ignoring any feedback loops resulting from a change in humidity, we expect that turning on chemistry results in some water vapour being converted into the "reservoir" species OH and HO_2. An overall decrease in water vapour is therefore expected, particularly where $O(^1D)$ is prevalent.

When switching off the HO_x mechanism, we indeed see that this is the case. However, when we completely switch off the chemistry scheme in our model, we find that the humidity is *lower* than with chemistry, meaning that our humidities cannot be

explained by the inclusion of chemistry alone. The decrease in humidity must therefore be attributed to two factors: the removal of the methane oxidation scheme used in Paper I, which produces water vapour depending on methane concentration, and the removal of the GHGs and the change in model top, which cause changes in temperature and atmospheric dynamics.

Further investigation is needed to quantify the contribution of the methane oxidation scheme; however, the results from Chapter 4 show that the inclusion of an online chemistry scheme (with H_2O as a reactant) can significantly alter the atmospheric profiles of water vapour, cloud cover and therefore ultimately temperatures. Cloud feedback on temperature is poorly understood even for Earth and one of the largest uncertainties in modelling of climate change (France et al., 2013). Much more work is needed to fully explore the implications of changes in water vapour availability in a model exoplanet atmosphere. An exploration over a range of planetary surfaces (varying land to ocean ratio) and water inventories (from Dune planet to waterworld) would be an interesting further step.

A full comparison with Paper I, covering heating and cooling rates, cloud cover, convective behaviour, precipitation and so on is beyond the scope of this work; however, we again refer the reader to subsection 4.2.1 for a more direct comparison between a model with an online chemistry and without.

3.4.2 Implications for planetary habitability

Our model suggests the planetary surface may be habitable, in agreement with Paper I, retaining a significant area of the planetary day side that is over 273 K (though our day-side maximum and night-side minimum temperature are respectively lower and higher). Ignoring any stellar activity and assuming that the Proxima Centauri flux does not significantly depart from the model spectral energy distribution, our model suggests the possibility of an ozone layer, even though UV flux is greatly reduced when compared with Earth.

This is good news for habitability. The ozone layer shields the surface from the most damaging UV (and higher energy) radiation. Figure 3.6 shows the surface UV is reduced by over 60% between 40 km and the surface, with most of the absorbed UV concentrated into the high energy bands. Similar studies with 1D models agree with our findings (e.g. O'Malley-James and Kaltenegger, 2017). Further investigation is required to understand the behaviour of the ozone layer after a flare, particularly with regards to surface UV, but we present an initial investigation in section 4.3.

Furthermore, the presence of persistent thick clouds at the substellar point is imprinted onto the surface UV levels, indicating that even without ozone, it may be

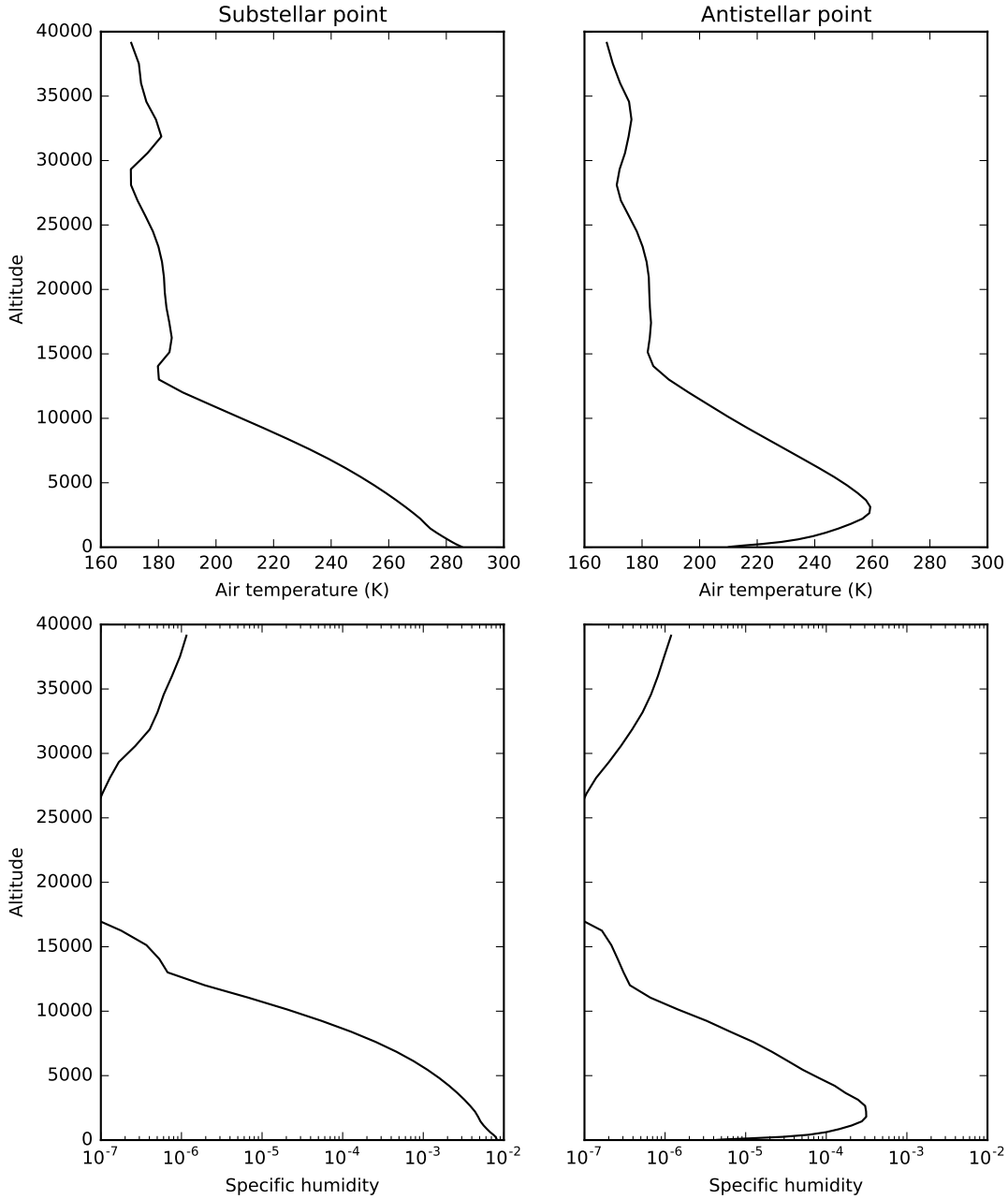

Figure 3.23: Temperature and water vapour profiles for the substellar and antistellar points. This provides a direct comparison with Fig. 5 from Paper I, though we have not run their nitrogen dominated simulation here. The left panel is the day side and the right panel is the night side.

possible to avoid damaging UV irradiation in the event of a flare or the loss/lack of an ozone layer. Much more work is needed to understand the cloud feedbacks on a tidally locked planet, and further simulations might cover planets with only a small quantity of water (known as a Dune planet, after Herbert's 1965 book of the same name) to investigate the impact of our assumption of a water planet.

On the Earth, tropospheric ozone causes health problems and smog. For reference, WHO air quality guidelines set a daily maximum 8-hour mean ozone concentration of around 50 ppb[6]. Our surface ozone values are significantly lower, ranging from 9 ppb at longitude 301°, latitude −57° to 0.3 at longitude 218°, latitude 59° with a surface-wide mean of 3.3 ppb. This is due to the rapid deposition at the surface and low overall atmospheric mass of ozone. Again, further simulations with the addition of continents and with no oceans would provide interesting comparisons here.

3.4.3 Implications for observations

The detectability of a given atmospheric gas depends on its concentration in the atmosphere. We have demonstrated here that for some of these gases – particularly ozone, which is commonly designated a potential biosignature – concentration may have a strong spatial dependence. Notably, there is a significant disparity in ozone concentration at high altitudes across the terminator[7], strong day/night differences in ozone columns and clear day/night differences in the concentration of our other tracer species and water vapour.

Whilst even pseudo-2D models (that is, two independent 1D columns on the day and night side) may correctly identify the differences in the day- and night-side chemistry, it would be impossible to model correctly without accounting for the atmospheric transport and dynamics (such as the jet) and features like that cold traps that clearly play an important role in the formation and structure of the O_3 layer. The terminator regions are especially important for observations; transmission spectroscopy probes only this region. It follows that our estimates of our chances of detecting atmospheric ozone (and other gases) at the terminator depend strongly on the accuracy

[6]See https://www.eea.europa.eu/data-and-maps/indicators/air-pollution-by-ozone-2/assessment

[7]There is next to no water vapour at very high altitudes, as it is removed very effectively through precipitation at lower altitudes (see Paper I). With no photons (on the night side) or deposition the ozone lifetime is extremely long at high altitude. Conversely, on the day side the ozone lifetime is much shorter due to the unattenuated UV flux. This region is not depicted in our plots, firstly to allow better comparison with Paper I and secondly because there are some minor issues with the radiation scheme, which is not designed for this sort of simulation, in the topmost layers of the model. These issues manifest in model output that appears visibly unphysical but is unimportant for the rest of the model.

of our modelling studies[8]. To take an extreme example, if it were possible to detect $O(^3P)$ through transmission spectroscopy, Figure 3.8 indicates that (depending on the geometry of the transit) the precise location of the day-night boundary would be the difference between attempting to detect a gas at 1 ppb and a gas at less than 1×10^{-12} ppb.

If we underestimate our chances of detecting a gas, we risk proposals being rejected for low probabilities of success and the needs of the community being ignored by instrument designers. If we overestimate detectability we risk false negatives (rejecting the idea that a planetary atmosphere contains ozone or some other gas based on a flawed expectation of high abundances). In both cases we risk the misidentification of optimum targets and the subsequent wasting of research time and money. Thanks to the work of the Earth science community, much of the fundamental modelling work has been done, so the step up to full 3D modelling for the exoplanet community is small. As a community we should make full use of the computational resources available to us, and the adaptation of 3D Earth models to exoplanets will allow us to skip straight from 1D to state-of-the-art 3D.

3.4.4 Discussion of model chemistry

This iteration of model is naturally only applicable to the most Earth-like planets; those with water, nitrogen and oxygen in their atmospheres with water oceans. However, without any conclusive data about the composition of exoplanet atmospheres we are only able to speculate based on formation models and the Solar System. Here we have assumed a very Earth-like planet. Our aim in this study is not to assess whether or not such a planet could feasibly form. Instead we aim to gain some understanding of the habitability of any sufficiently Earth-like planets – in other words, we wish to answer the question "if an Earth-like planet with an Earth-like atmosphere could form here, would it be amenable to life?"

However, the model is an adaptable framework, and the inclusion of additional simple chemical mechanisms in future is possible. Likely candidates are the NO_x catalytic cycle (with precursors produced through stellar flares, lightning, volcanic activity, as well as aeroplanes and some organisms on Earth) and methane chemistry. We discuss this further in subsection 5.2.1.

The Chapman mechanism and HO_x catalytic cycle are a good description of an Earth-like atmosphere composed of mainly of water, oxygen, inert gases and UV

[8]It is of course possible to estimate the *detectability* with a 1D model but with a strong spatial inhomogeneity it is difficult to say whether or not a given detectable concentration is physically possible.

photons – i.e. a planet that would almost certainly be habitable by current definitions. However, an oxygenated atmosphere is not a requirement for habitability; Earth itself is thought to have had a reducing atmosphere in the past. In a planetary atmosphere that contains a significant quantity of CO or CH_4 (perhaps dominated by methanogenic life) or that retains a hydrogen envelope or some other reducing atmosphere, the atmospheric chemistry will be different, and the two mechanisms explored above will likely be unimportant. Simulations of these types of planetary atmospheres pushes GCMs that were originally designed for Earth too far outside of their bounds in many cases (though we note that the UM performs well in dynamical simulations of e.g. hot Jupiters; see Mayne et al. (2014) for example). We anticipate that, as in the oxygenated, tidally-locked case, 3D online chemistry schemes will show some departures from 1D models or 3D models with no chemistry when simulating planets that have some sort of strong spatial inhomogeneity, such as tidal locking. In these cases we encourage the development of models that include online chemistry. If one were to retain only the most fundamental framework of the UKCA – i.e. the chemical solver and radiation scheme – it is possible that reducing atmospheres could be simulated in future. However, the core of the model does not currently contain condensation of any species other than water, complicating matters. Work is ongoing to add more condensing species.

3.5 Conclusions

We have adapted the UK Met Office Unified Model to include a full, online, 3D photochemistry scheme, which simulates chemistry in a tidally-locked M-dwarf planet atmosphere. We focus specifically on atmospheric ozone in an atmosphere with an Earth-like composition and therefore include the Chapman mechanism and the hydrogen oxide catalytic loss cycle, which describe the ozone layer through interactions between oxygen, water and UV photons. We believe this to be one of the first fully online, fully 3D atmospheric chemistry models for a true tidally-locked M-dwarf planet (as opposed to Earth simulations that simply change the rotation rate).

Our model is based upon that of Boutle et al. (2017), which uses orbital and planetary parameters from Proxima Centauri b. The model has shown that it is possible to develop an ozone layer on such a planet, even with TOA UV levels $100\times$ lower than those on Earth. This is a key result from the model; the viability of an ozone layer on an M-dwarf planet is disputed (though we note that our model does not include the effects of M-dwarf activity and extreme UV flux).

The resulting ozone layer takes an interesting format; the ozone settles into a band at the typical $20-40$ km altitude, with a significant build up of ozone on the night side at low altitudes near the cold traps. We find total ozone columns are around 10 times smaller than for Earth, but the distribution is much less uniform with the greatest ozone columns occurring above the cold traps.

The distribution of ozone through the atmosphere is controlled by transport due to the long chemical lifetimes. In terms of chemistry, the dominant loss mechanism is the hydrogen oxide catalytic loss cycle. Ozone lifetimes range from a few years on the day side to thousands of years on the night side.

Comparing with Boutle et al. (2017), our simulations tentatively suggest that the online chemistry scheme slightly decreases the atmospheric temperature above 15 km, reduces (already low) humidity throughout the atmosphere and reduces maximum and minimum surface temperatures by 3 K, though there are some differences between the two model configurations that prevent us from directly attributing all of the observed changes in the model output to the chemistry scheme.

CHAPTER 4

Sensitivity of Ozone and Climate on M-dwarf Planets

ABSTRACT

We present results from a suite of simulations that examine the impacts of certain planetary parameters on the habitability and atmospheric chemistry of our M-dwarf planet described in the previous chapter. We find that the simulations are highly sensitive to the chemistry scheme used, with night-side ozone columns having a significant effect on the atmospheric circulation. Reverting to a prescribed ozone layer results in a night side that is more than 50 K warmer at some points on the surface.

We also look at the sensitivity of our model to the initial abundances of our chemically-active tracer species, where we find that the model spin up time is highly dependent on the abundance ratio of HO_x species to O_x species.

Following this we subject our atmosphere to an electromagnetic flare. We find that the flaring has minimal impact on our total ozone column; however, uncertainties regarding the spin up become important. Our results again point to the importance of the spatial dimensions in the chemistry simulations.

Finally we simulate the same planet on an Earth-like orbit at 1 AU with solar irradiation and the M-dwarf planet in a resonant, eccentric orbit. In both cases our model suggests that planetary rotation produces a more homogeneous ozone layer with less severe temperature gradients. In the Earth-like orbit simulation we find around 100× more surface UV and greatly increased ozone columns (akin to Earth). Behaviour of atmospheric ozone in the two M-dwarf orbits is very similar, with the exception of the spatial non-uniformity arising from the transport effects described in the previous chapter.

Author Contributions: I wrote the chapter, developed the simulations and performed analysis, with guidance and editing suggestions from Paul Palmer.

4.1 Introduction

In Boutle et al. (2017), henceforth referred to as Paper I, the authors demonstrated the use of the Met Office Unified Model to simulate close-orbit exoplanets, particularly centred on Proxima Centauri b. In Chapter 3, we built on that work by developing a chemistry module, and using it to show that a tidally locked planet with an atmosphere composed of approximately 80% N_2 and 20% O_2 can maintain a weak ozone layer, even with a greatly reduced TOA UV flux (compared to Earth).

Here we develop these results by investigating the effects of given physical properties or mechanisms on the atmosphere. In particular, we simulate a planet in a 3:2 resonant orbit, a planet at 1 AU with a Sun-like TOA spectrum, a planet subjected to weak stellar flares and investigate the impact of switching off parts of the chemistry scheme. For brevity, we focus on the end state of the model and the factors like the ozone columns, surface temperatures and surface UV values which are important for habitability, rather than conducting a detailed analysis of the model chemistry as in Chapter 3. The model runs herein are summarised in Table 4.1.

For each simulation we describe the motivation behind the model run and its set up, followed by the model results, comparing with the control case from Chapter 3 where appropriate. We discuss the tidally locked simulations first and subsequently the simulations with different orbits.

We show the mean ozone column over time in Figure 4.1, which indicates the spin up time for each of the models with chemistry. In Figure 4.2 we show some key features of the simulations where the planet is tidally locked. We neglect to show some of the atmospheric parameters such as meridional winds, which show no significant features.

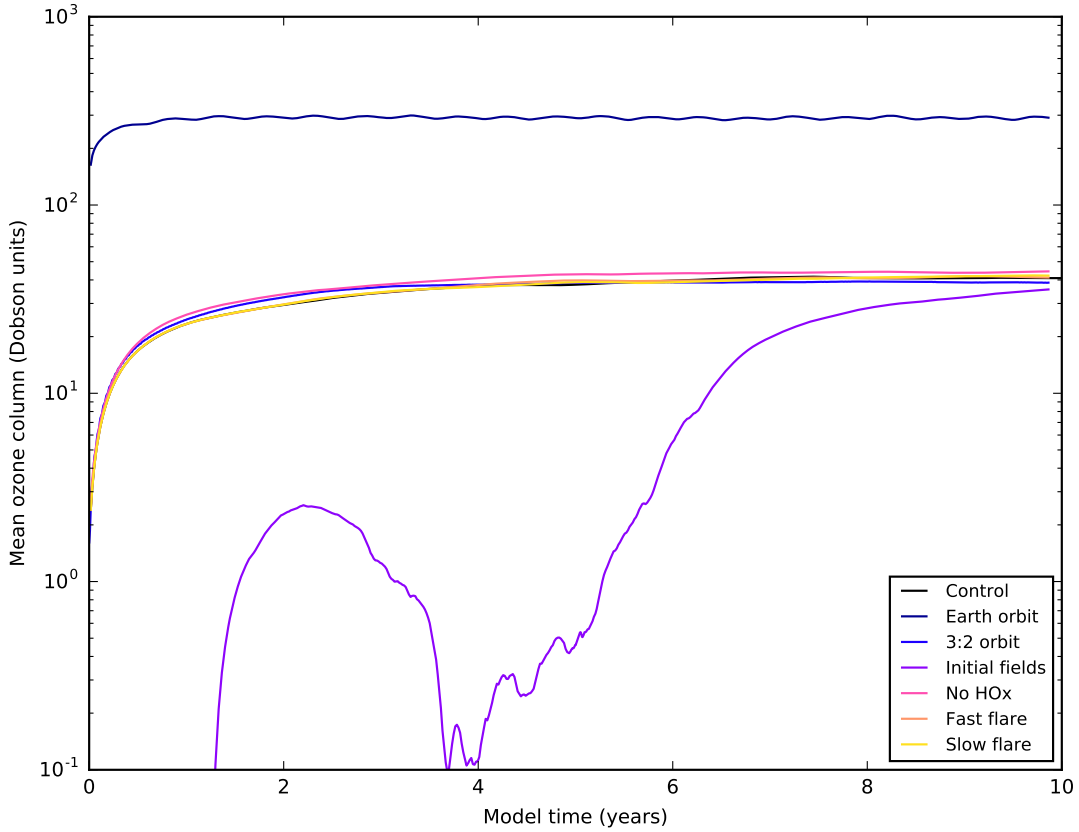

Figure 4.1: Mean ozone column over time in each of the simulations. With the exception of the initial conditions run, each model has reached a (chemical) steady state within 10 years. As the mean ozone column is area-weighted, it is proportional to total atmospheric ozone mass. Non-chemical model spin up times are much shorter, on the order of a year, but we run for 10 years for ease of comparison with other models.

Simulation	Orbital configuration	Description
Control	Tidally locked	Control simulation, as described in Chapter 3
No chemistry	Tidally locked	Model run with chemistry switched off
No HO_x	Tidally locked	Model run with HO_x mechanism switched off
Fast flare	Tidally locked	Stellar flux is increased to 600% for one hour, once annually
Slow flare	Tidally locked	Stellar flux is increased to 150% for one day, once annually
3:2 orbit	Eccentric 3:2 resonance orbit	Otherwise identical to control run
Earth orbit	Earth orbit	Planet is moved to 1 AU with Earth-like rotation rate and solar insolation

Table 4.1: Simplified description of each of the model runs.

4.2 Comparison of chemistry schemes

To determine the impact of our choice of chemical scheme, we run our control simulation with the HO_x mechanism removed, with the chemistry completely switched off and with different initial chemical concentrations.

4.2.1 No chemistry

We chose to use an online chemistry scheme partly in order to gauge its importance in an assessment of planetary habitability. Models are chaotic and sensitive[1]; in some cases, if the feedback from the chemistry scheme is large enough, a model with no chemistry may predict a habitable surface where none is possible and vice versa. It is conceivable that such a situation might occur (for example) on the edge of the CHZ, on a planet where the planetary albedo is dominated by clouds and cloud formation depends on the chemistry[2] (to some extent true on Earth; e.g. Charlson, 2001). On our own planet, we are learning that only a few degrees of warming could have dramatic impacts on our climate (Collins et al., 2013).

In subsection 3.4.1, we made some comparisons with Paper I that demonstrated clear differences between the output of our model and theirs, but were unable to properly attribute the differences to the chemistry scheme due to other factors like the changing GHG concentrations, increased model top and methane oxidation scheme. Here we avoid these uncertainties by running the exact same simulation as our control, except with the chemistry scheme switched off. In this case the model defaults to a static 3D O_3 field that is taken from Earth simulations. This field is identical to the one in the Paper I simulations and is described in detail in that work. In brief, ozone columns are around 10 times larger, with less ozone at the poles and the ozone layer being higher in the atmosphere. By comparing the outputs between the control and this simulation, we directly demonstrate the impact of an online chemistry scheme on the climate system.

We discuss first the key metrics shown in Figure 4.2. We show the difference (deltas) between the run with no chemistry and our control run (i.e. the model described

[1]Chaos theory was pioneered by Lorenz after discovering that weather models were highly sensitive to initial conditions (Lorenz, 1963).

[2]Naturally, with current characterisation capabilities, the uncertainty in planetary and atmospheric composition, stellar activity, orbital configuration and so on is likely to dwarf the impact of any chemistry feedbacks. However, for a given atmospheric composition and set of planetary parameters, the inclusion (or not) of atmospheric chemistry could significantly move the inner and outer edge of the CHZ in models. Such a situation might occur as the first detailed exoplanet characterisation results are returned.

in detail in Chapter 3) in the day and night side mean profiles. The model run with no chemistry is depicted in black.

Our results show that the two models differ quite significantly. Looking first to the temperature profile deltas, switching off chemistry results in a day side that is 5 K warmer above 15 km and 5 K cooler below this point with a difference of 2.6 K in the surface layer. On the night side, the atmosphere is more than 5 K warmer in the top 15 km, 2.5 K warmer between 15 and 25 km and up to 5 K cooler between 15 and 2 km. The most significant differences are in the surface layer, where the mean night side temperature is 9.5 K warmer without chemistry. Comparing the day and night side profile, we note that the day-night temperature gradient is smaller at most altitudes but especially at the surface.

We attribute the increased high-altitude temperatures directly to shortwave ozone absorption, which increases the temperature by 5 to 10 K in the stratosphere (as found in Paper I, comparing the nitrogen and Earth-like simulations). This absorption will result in a colder lower atmosphere; we note that in Paper I the main source of heating on the day side (as given in Figure 4) is short-wave radiation, and their Figure 5 shows the same upper/lower atmosphere temperature contrast between the Earth-like simulation with ozone and the nitrogen-dominated simulation without.

We show surface temperatures in more detail in Figure 4.3. We show the output from the model on the left and the delta between this model and the control run on the right. On the day side, temperatures are slightly lower in the run without chemistry up to around latitudes $\pm 70°$, but the temperature gradient is higher in the control run meaning that the poles are colder with chemistry on. The net result is that in both models the area of the surface that remains above the important 273 K water triple temperature is about the same, but the area that is at around 300 K is larger in the run with chemistry extending much further polewards, up to almost latitude $\pm 50°$.

On the night side the temperatures are radically different between the two runs, being notably warmer without the chemistry. At the anti-stellar longitudes the run without chemistry is more than 50 K warmer either side of the jet. The cold traps have moved eastward, up to the terminator, where there is a very steep temperature gradient, but at the coldest point the temperatures are only slightly warmer in the run without chemistry. With the chemistry on, the cold traps cover a much larger area, expanding up to the poles (as noted above). At the equator, the two simulations have similar temperatures at around 210 K.

In our models (as well as the Paper I model) the night side of the planet has little to no cloud cover or water vapour resulting in very efficient radiative cooling, with the bulk of the night side heating occurring through transport from the day side. Given that the only differences between the two models presented here (in terms of radiation)

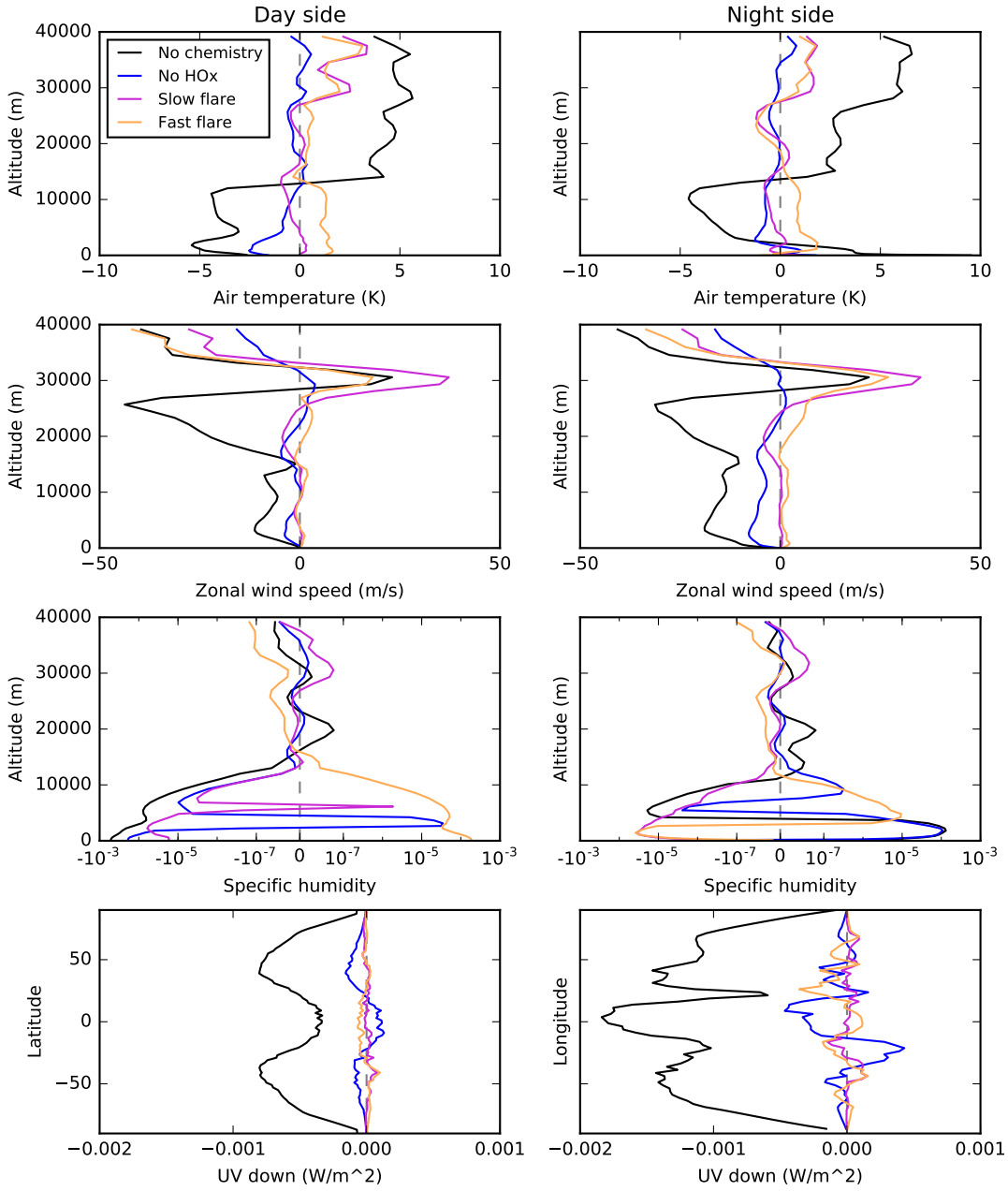

Figure 4.2: Differences in key parameters compared with the control run for the tidally locked simulations. We subtract the control run data from the sensitivity run data, thus a positive value on e.g. the air temperature plot indicates that the sensitivity run atmosphere is warmer than the control. For the top three plots, the left panels show day-side mean and the right panels show night-side mean. In the specific humidity plot the axis is symmetrical-logarithmic with the central portion (-10^{-7} to 10^{-7}) being linear and the remainder logarithmic. In the bottom plot we show zonal and meridional means for the planet's day-side.

are water vapour and ozone concentration, and that ozone is a strong absorber in the infrared (Shields et al., 2016) and there is very little water vapour on the night side, we theorise that our much smaller ozone columns in the model with chemistry result in a significantly more transmissive atmosphere on the night side, making the cooling mechanism even more efficient.

In Paper I it was suggested that the day side temperature may be controlled by the night side temperature through efficient heat redistribution by the super-rotating jet, following Showman and Polvani (2011) and Pierrehumbert (1995). Our results appear to contradict this supposition, as the decreased night-side temperature does not result in a decreased day-side temperature. We speculate that the heat redistribution may be more efficient but that the day-night heating contrast (ignoring the heat redistribution of the jet) is even larger; that is, the magnitude of the day-night heat redistribution effect has increased, but has increased less than the night-side cooling rate. Further simulations are needed to fully capture the dynamical effects at work here.

Returning to Figure 4.2, we see that wind speeds are much lower with the chemistry switched off. At the altitude of the atmospheric jet, at $20-25$ km, wind speeds are lower on both the day and night sides, by over 40 m/s on the day side. Below 15 km wind speeds are again lower on the day side but more so on the night side where winds are up to 20 m/s slower. The day-night temperature gradient is a factor in the driving and generation of the superrotating jet (Showman and Polvani, 2011); the smaller day-night temperature contrast when switching off chemistry results in a weaker jet.

We do not place much weight on the wind speeds at 30 km and above; since all model runs differ from the control above this point we assume that the control run was in some perturbed state and that with longer time means this disparity would disappear. We have found that the precise altitude of the jets can vary, particularly at high altitude, and suggest that in this case the jet in the control was at a higher altitude than in the other runs. This explains the sharp change from a negative wind speed delta at 40 km to a positive at 30 km. By contrast, the change in windspeed due to removal of chemistry is a real feature that is caused by the aforementioned temperature gradient.

Comparing specific humidities, we find that humidity is decreased at low altitude on the day side of the planet when chemistry is switched off and mostly lower on the night side but slightly increased in the lowest few km. We do not see any significant changes above $10-15$ km where all models show very low humidity. One would expect that (ignoring any dynamical effects) humidity would be lower with chemistry switched on due to the removal of water molecules through HO_x mechanism. Comparing to the deltas for the run without the HO_x mechanism, we see that the removal of the HO_x reactions increases humidity as expected, meaning that the decreased humidity is due

to some other effect. In Paper I it was found that humidity in the model (without chemistry) arises almost entirely from convection on the day side; our warmer day side likely drives more convection resulting in the change in humidity.

Finally, we see that the model run without chemistry results in lower surface UV, an obvious consequence of a lower ozone column. Note that in Figure 4.2 we show an *absolute* difference between the two runs as opposed to a proportional difference, thus the features across latitude and longitude simply reflect the structure that results from clouds, as described in subsection 3.3.2. Returning to Figure 4.3, we see the reduction in UV flux at the surface is fairly homogeneous but there is some structure at the equator, where our chemistry scheme predicts a slight enhancement in ozone compared to the higher latitudes. Overall surface UV is reduced by around 10% overall, up to 30% at some locations.

4.2.2 No HO_x mechanism

We chose to include the HO_x mechanism because it is an important sink of O_3 on Earth, and likely to be an important chemical mechanism where water vapour and ozone interact (Jacob, 1999). As shown in Figure 3.20, HO_x dominates ozone (chemical) lifetime throughout most of the atmosphere, with the exception of the surface and the top layers of the atmosphere on the day side, where deposition and the Chapman mechanism become more important respectively. To investigate the impact of this mechanism further, we ran the simulations with the HO_x mechanism switched off.

As expected, we see an increased mean ozone column when removing HO_x. In our control simulation, the mean ozone column over the entire surface is around 41 Dobson units; with the removal of the HO_x mechanism this increases to 44 Dobson units. Comparing the ozone lifetimes due to the Chapman mechanism and the HO_x cycle in Figure 3.20, one might expect a much higher mean ozone column in this simulation; however, we note again that transport plays an important role in the structure and formation of the ozone layer, thus the chemical lifetimes exaggerate the importance of the HO_x cycle throughout most of the atmosphere.

Looking firstly at the important atmospheric parameters in Figure 4.2, we see some similar effects to those above that result from an increased ozone column, except reduced in magnitude. We do not see any major change in day/night temperature profiles or wind speeds (excepting the anomalous jet altitude above 30 km in the control run, described above). At the surface, we also find that UV irradiation is reduced, in line with the increased ozone columns, by as much as 10%.

We see increased humidity on the both sides of the planet. In the control run we expect that some water vapour will be converted into OH or HO_2 due to the HO_x

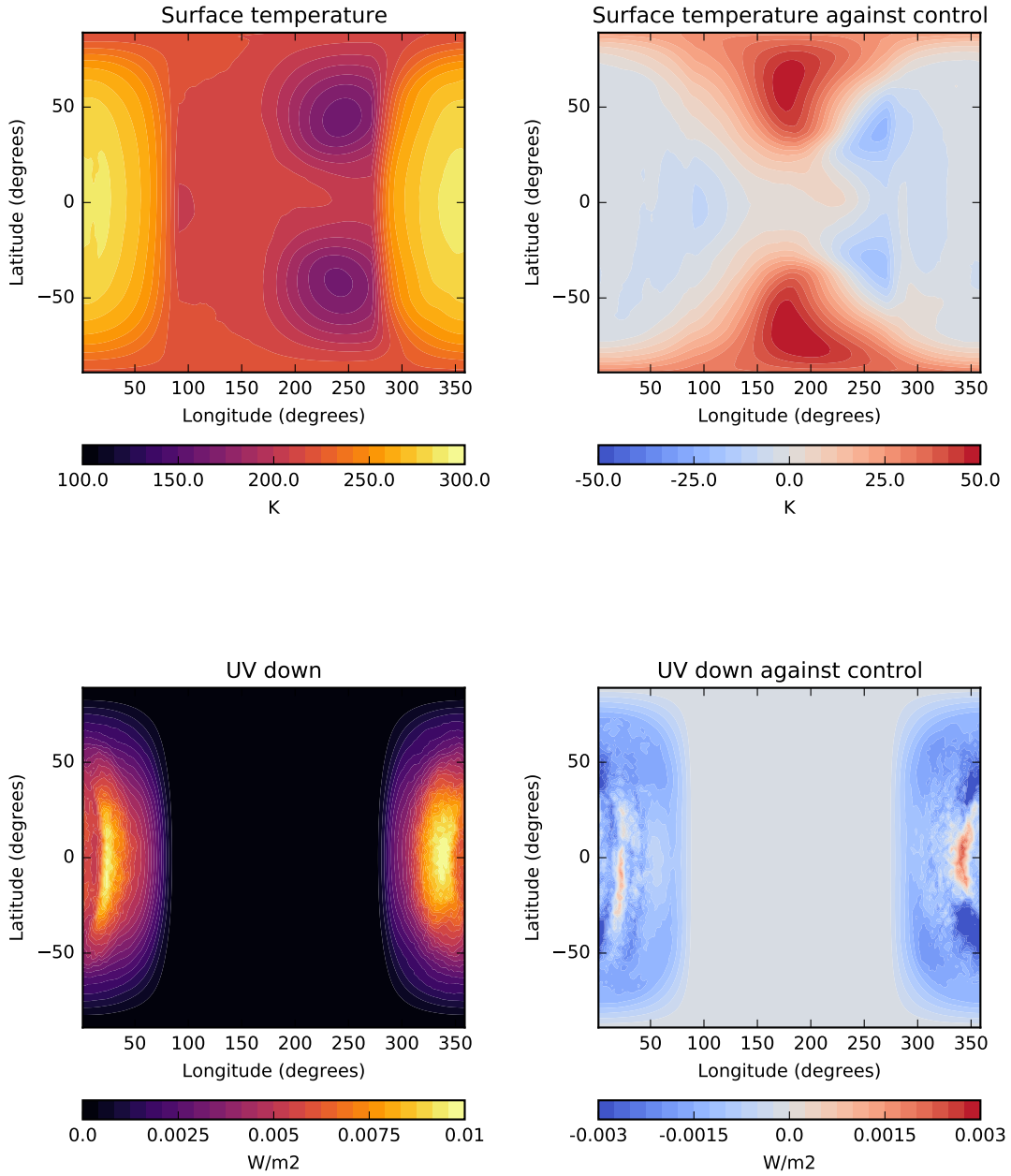

Figure 4.3: Comparison of temperature and surface UV with and without chemistry in the tidally locked simulation. On the left we show the output from the model (without chemistry) and on the right we show the change compared to the control run (i.e. a positive value shows an increase over the control run).

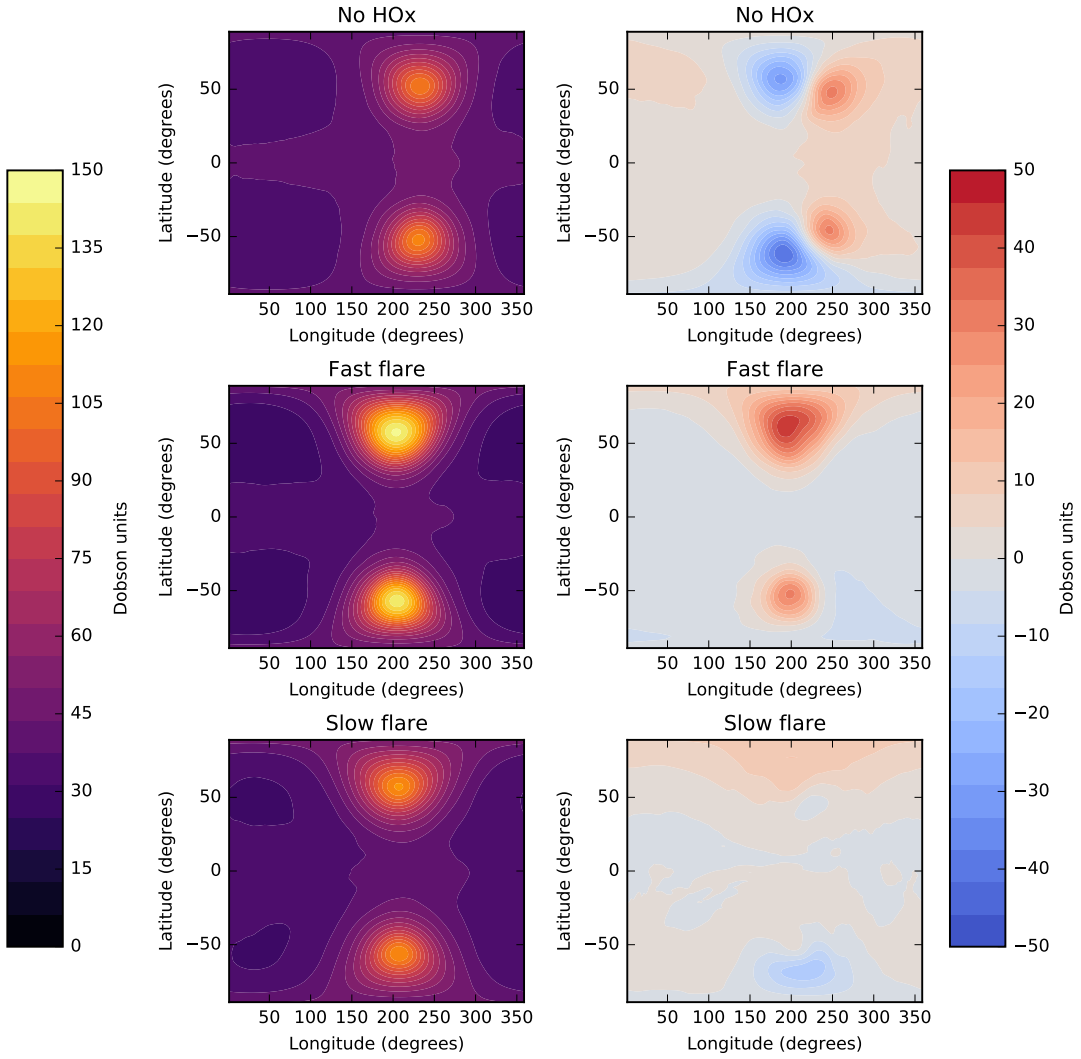

Figure 4.4: Differences in O_3 columns in tidally-locked runs. On the left we show the values from the model and on the right we show the change compared to the control run (i.e. a positive value shows an increase over the control run).

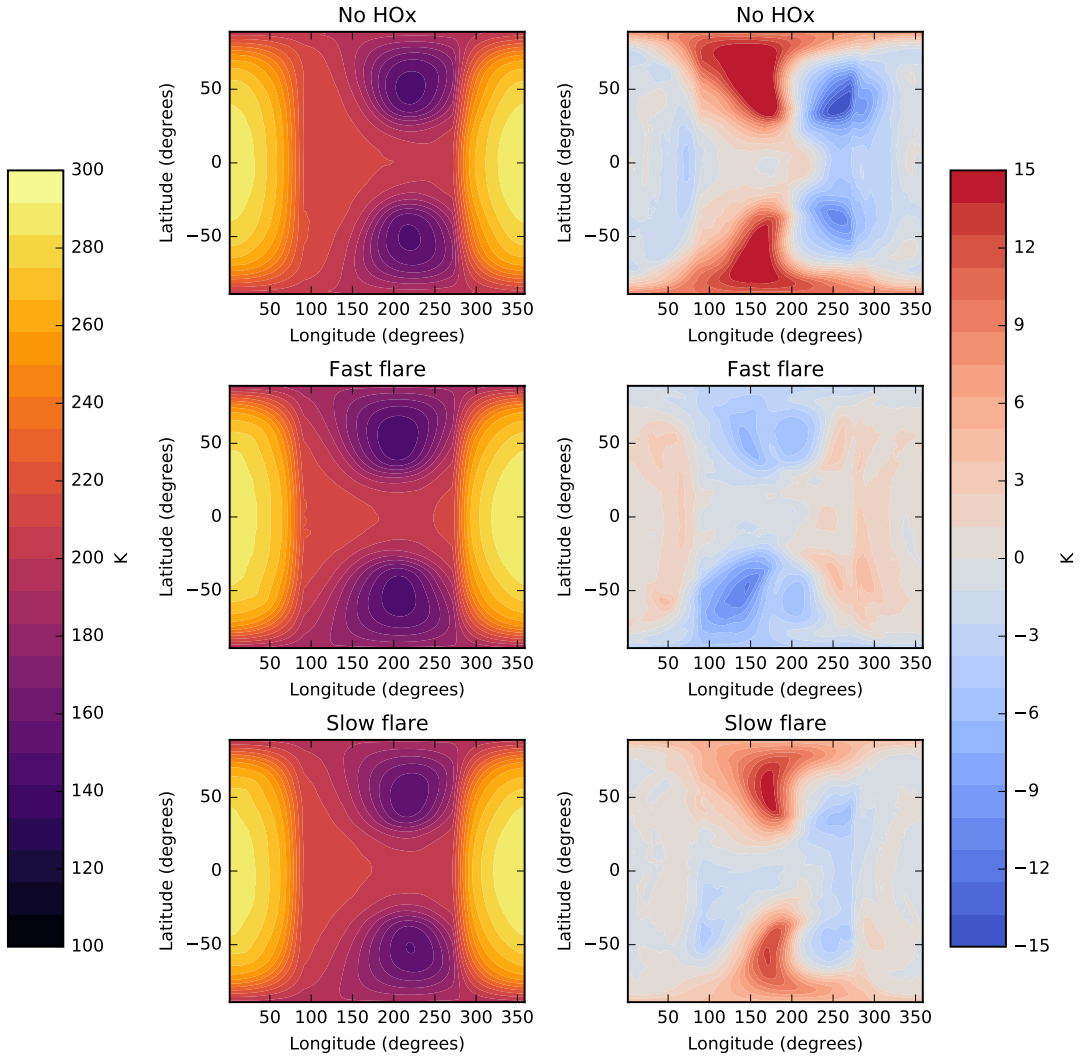

Figure 4.5: Differences in surface temperature in tidally-locked runs. On the left we show the values from the model and on the right we show the change compared to the control run (i.e. a positive value shows an increase over the control run).

mechanism; the removal of the HO_x mechanism should result in increased humidity. The effect is mostly small in magnitude (a few percent) as a fraction of total humidity.

We show ozone columns from this simulation in Figure 4.4. It is immediately obvious that in this simulation the cold traps have moved eastward, and indeed this is confirmed through the plot of surface temperature in Figure 4.5. As in the run with no chemistry, we see increased night-side temperatures between longitudes 90° and 180° and at the poles. Day side temperatures remain similar between the full chemistry model and this model. The magnitude of the change in night-side heating is smaller here, changing the surface temperatures by 20 K (c.f. over 50 K without chemistry).

It is remarkable that such a small change in the mean ozone column results in such a large change in the planetary dynamics. We note that the results from this simulation represent a sort of half-way point between the full chemistry scheme and the run without chemistry in terms of the total atmospheric ozone. We believe this again demonstrates the importance of ozone in the cooling mechanism on the night-side of the planet, and the spectrum of simulations presented here indicates the changes in the atmosphere under increasing night-side ozone columns. As night side ozone increases, the cold traps move eastwards towards the terminator and inward towards the equator, resulting in increased polar temperatures and a much warmer night side between 90° and 180°. The sensitivity to low total ozone columns (around 40 Dobson units) seems to be larger than with large total ozone columns (Earth-like, around 300 Dobson units).

Further model runs are needed to constrain this relationship and determine its sensitivity. Model runs with smaller total ozone columns (than our control case) may result in points in the atmosphere that are cold enough to initiate CO_2 condensation, which can results in a dramatic snowball feedback through the severely reduced atmospheric greenhouse effect (though the UM cannot currently simulate CO_2 condensation).

4.2.3 Varying initial tracer fields

Given that the three key initial reactants in the model are photons, O_2 and H_2O, we have assumed that with enough model time any simulation will eventually reach the same final state. It is not inconceivable, however, that sufficiently different initial conditions could cause a dramatic change in (for example) the atmospheric humidity and resulting in a different equilibrium state between O_3 and the HO_x species. To test this hypothesis further, we ran the simulations with 1000-fold enhanced OH and HO_2 concentrations and 1000-fold reduced O_3, $O(^1D)$ and $O(^3P)$ concentrations (that is, MMRs of 10^{-6} and 10^{-12} respectively, compared with the universal 10^{-9} in the control).

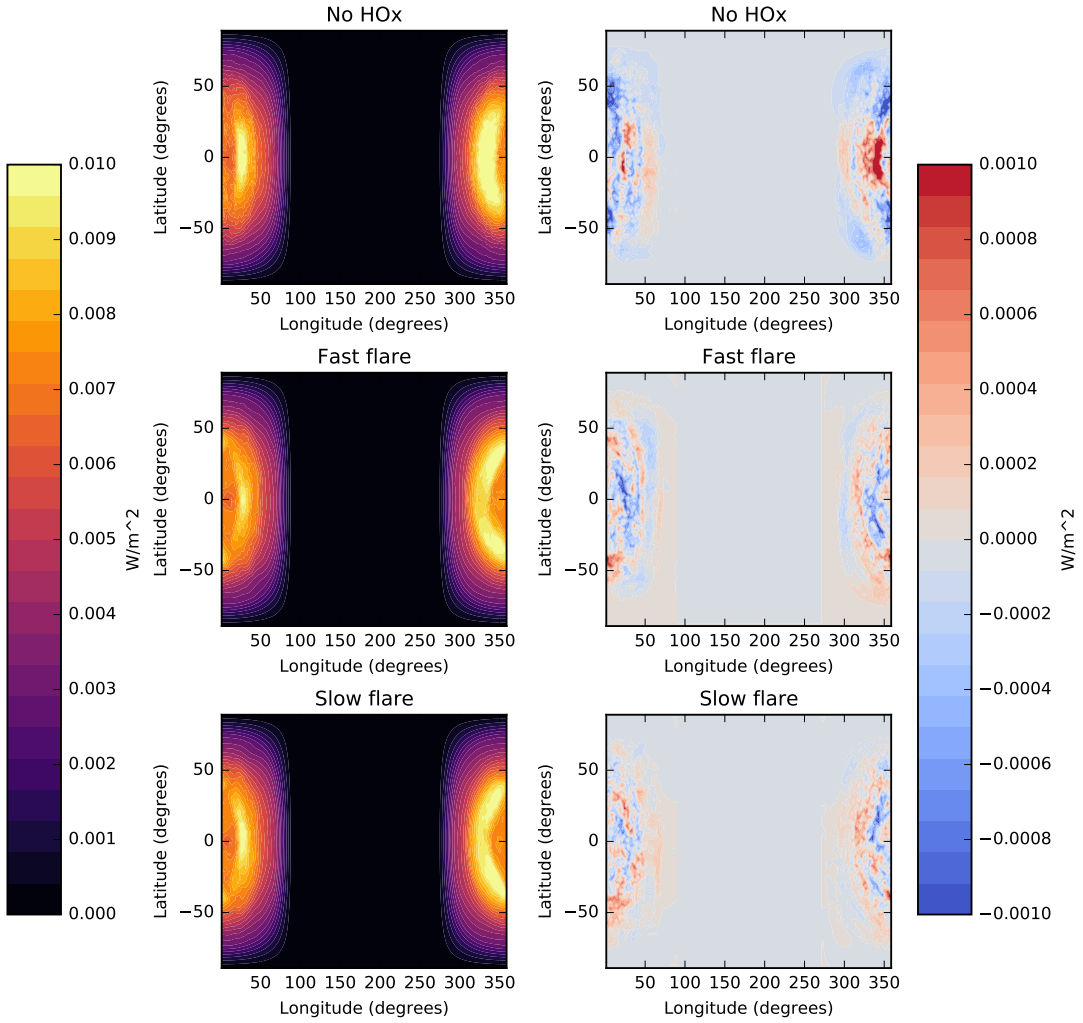

Figure 4.6: Differences in surface UV in tidally-locked runs. On the left we show the values from the model and on the right we show the change compared to the control run (i.e. a positive value shows an increase over the control run).

We show the mean atmospheric ozone column over the spin up period in Figure 4.1. In this case it is obvious that the model is clearly still evolving after 10 years of simulation time, and displays some interesting behaviour in the first 5 years. We are however confident that in this case the model is approaching the same equilibrium state as the control run. We note two things here; firstly, that all of the models (asymptotically) approach very similar mean ozone columns, all within a few Dobson units (except the Earth run), and that none of them appear to overshoot this point. This suggests that the chemical mechanism is, to some extent, self-damped, at least in the case where humidity is low and ozone concentration is high. We therefore expect that O_x/HO_x ratios between 1:1 from our control run and the 10^{-6}:1 ratio employed here will result in the same final state of the model.

However, it is conceivable that our initial conditions for this run placed it at some threshold for a regime change. This is evidenced by the severe decrease in mean O_3 column after the first 2 years; the model teeters at some point and after 2 years is perturbed such that almost all atmospheric ozone is lost. This regime change could entail the total (permanent) loss of the atmospheric ozone or some sort of oscillatory state where ozone is produced and subsequently removed over a period of years. Simulations with a range of initial chemical states and different water inventories are required to understand this further.

We do not show further results from this model run, but these simulations are ongoing.

4.2.4 Discussion

Our results from this section have shown that the model is extremely sensitive to ozone columns on the night side of the planet, and clearly demonstrate the importance of the chemistry scheme in the accurate simulation of the atmosphere. The night side cooling rate is known to be an important dynamical parameter on a tidally-locked planet (Heng and Kopparla, 2012; Yang and Abbot, 2014), and changing it is enough to significantly move the night-side cold traps and decrease the temperature at the poles of the planet. The temperature at the poles is an important parameter for planetary habitability; ice-albedo feedbacks can result in a "snowball Earth" scenario, where the increased albedo of ice causes reflects away radiation causing cooling, thereby creating more ice (see e.g. Shields et al., 2013). Whilst our planet retains a significant portion of the surface that is above 273 K, our results demonstrate that small change in the amount of ozone – as little as a 10% change in the ozone column in the case of the HO_x mechanism – is enough to change night side surface temperatures by as much as 20 K.

Further simulations are required here. Reducing the total ozone column even

further would allow us to determine how low the night side and pole temperatures can go, placing some constraints on the habitability of a tidally locked planet with an Earth-like atmospheric composition. It is of course possible that reducing the ozone column further (to 0 even) may not change the dynamics any further; at some stage the absorption due to ozone on the night side will become unimportant.

4.3 Flaring

M-dwarf stars are frequently found to be active and flaring is likely to be a critical factor in M-dwarf planet habitability; for an Earth-like planet orbiting an active star, the loss of atmospheric ozone can leave the surface exposed to deadly levels of UV (Shields et al., 2016). Simulations have shown that the ozone column should be relatively insensitive to electromagnetic radiation, with ozone loss being driven by particle flux more so than radiation (Segura et al., 2010; Tilley et al., 2017; Howard et al., 2018).

To investigate this, we run our model with a simple parameterised flaring routine. We use the default model configuration of a tidally-locked M-dwarf planet from Chapter 3. However, we additionally subject the planet to a periodic flare from the star. Our model does not simulate charged particles or X-ray and gamma ray radiation by default, so we limit this initial study to an electromagnetic-only flare that is parameterised through an increased TOA flux in the chemistry scheme, but we discuss this further in subsection 5.2.1.

Note that, as described in subsection 3.2.2, the normal model radiation and radiation for chemistry are separate parts of the model; hence the increased radiation in the chemistry scheme has no direct effect on the dynamics through heating etc. However, a decrease in (for example) O_3 abundance will ultimately result in increased UV transmission in the dynamical part of the model, impacting the heating and ultimately feeding back into atmospheric transport, cloud formation and other important dynamical systems. This is an important mechanism that requires an online chemistry scheme; an offline chemistry scheme cannot describe these feedbacks due to the chemical composition of the atmosphere and the radiation scheme being disconnected. Our earlier results in section 4.2 have clearly demonstrated the importance of total ozone column on the night-side radiative cooling rate, which is a critical factor in the model dynamics. A simulation of a stellar flare is therefore a useful demonstration of the utility of this model.

The flaring routine is adapted from solar cycle code. A banded 1 AU flux (at the same wavelengths as the standard UKCA wavebands; see Table 3.2), which we call the flare flux $f_{\text{flare}}(\lambda)$, is multiplied by a scaling factor, $x(t)$, defined at an hourly cadence over 1 Earth year. This is then added to the standard 1 AU flux, $f_{\text{UKCA}}(\lambda)$ (defined in Table 3.2):

$$f_{\text{net}}(\lambda, t) = f_{\text{UKCA}}(\lambda) + x(t) \times f_{\text{flare}}(\lambda) \tag{4.1}$$

$f_{\text{net}}(\lambda, t)$ is then scaled to orbital distance to find TOA flux before the photolysis runs.

In our case we simply set $f_{\text{flare}}(\lambda) = f_{\text{UKCA}}(\lambda)$ such that:

$$f_{\text{net}}(\lambda, t) = (1 + x(t)) \times f_{\text{UKCA}}(\lambda) \tag{4.2}$$

Thus, we can simulate an overall increase in insolation on an hourly cadence. We simulate a "fast" flare and a "slow" flare:

a) $x(t) = 5$ for 1 hour, once annually, 0 at other times

b) $x(t) = 0.5$ for 24 hours, once annually, 0 at other times

The fast flare is intended to replicate the total flux of an observed superflare, which reached is estimated to have peaked at around 68× the normal flux from the star for a short period of time, followed by a decay phase where flux returns to normal levels (Howard et al., 2018). We approximately scale the total flux to a period of one hour, which is our minimum flare duration. This short flare is intended to allow us to investigate the impact of the flare on the chemistry, should any occur. The slow flare is intended as a sensitivity test, to determine whether or not the flare duration has any impact on the chemistry through some feedback mechanism. As noted above, our radiation timestep is fixed at one hour, thus it is not possible to simulate a realistic flare that has a duration of only a few minutes. We note that the total irradiation from the two flares is different: the slow flare inputs the same amount of energy as 12 hours of stellar radiation whilst the fast flare inputs only 5 hours. We choose to initiate the flare only once annually so that it is possible to study the recovery time of the ozone chemistry.

4.3.1 Results

In both cases, we find that there is almost no change in the total ozone column during and after the flare. In the reaction fluxes during a flare, we see an increase proportional to the increase in stellar radiation, but as the flare ends the reaction fluxes quickly return to normal values. Our findings align with those of Segura et al. (2010) and Tilley et al. (2017), who also find that there is little to no change in total ozone column for an electromagnetic flare. Overall, final mean ozone columns are slightly increased in the two flaring runs, but the increase is much smaller than the variation in total ozone exhibited by all of the runs. Much more model time is needed to quantify the change in total ozone column with any confidence.

We do note some differences between the two simulations and the control run. We present ozone columns in the model output in Figure 4.4, surface temperatures in Figure 4.5 and surface UV in Figure 4.6.

We note first of all that there is little change in surface UV, which has been shown in the previous sections and Figure 4.2 to be mainly controlled by the ozone column, which shows no real variation on the planet's day side between the three models.

On the night-side however we do see some changes. Our fast flare run has a much higher ozone column at the cold traps compared with the other two models, and the slow flare has a lower ozone column in the Southern hemisphere at the cold trap and a higher ozone column at the nothern pole. Interestingly, despite the increased ozone column, our fast flare simulation has lower temperatures at the cold traps and higher temperatures on the day side, in contrast with the results from the earlier simulations without the chemistry scheme or HO_x mechanism, which appear to suggest that the ozone column controls the night-side cooling rate. Here the increased ozone column is paired with lower night side temperatures. Our slow flare also displays higher temperatures at the anti-stellar longitudes either side of the jet.

We show the change in ozone concentration between these two runs and the control run in Figure 4.7 and Figure 4.8. In both of these figures it is clear that ozone concentration changes at the poles above 20 km, with increased ozone concentration lower down and decreased ozone above. This change is driven by the increased UV flux in the upper atmosphere.

Tilley et al. (2017) found that their model was more sensitive to flaring during the spin up. With our model being so sensitive to night side ozone columns, and changes in initial chemical composition resulting in a drastically increased spin-up time, we take this as an indication that the models are still evolving. This is evidenced by the fact that even though total atmospheric ozone is constant and similar between the two models, the columns are very different. We suspect that our standard 10-year spin up is insufficient for the case where we are adding a recurring chemical shock to the system in the form of increased stellar radiation. These model runs are ongoing and much longer run times will allow us to find out when and how the models will reach a steady state. Furthermore, model runs are being conducted where the flaring is only initiated after at least a 10-year spin-up. This will avoid any effects that arise from the sensitivity of the model to initial conditions.

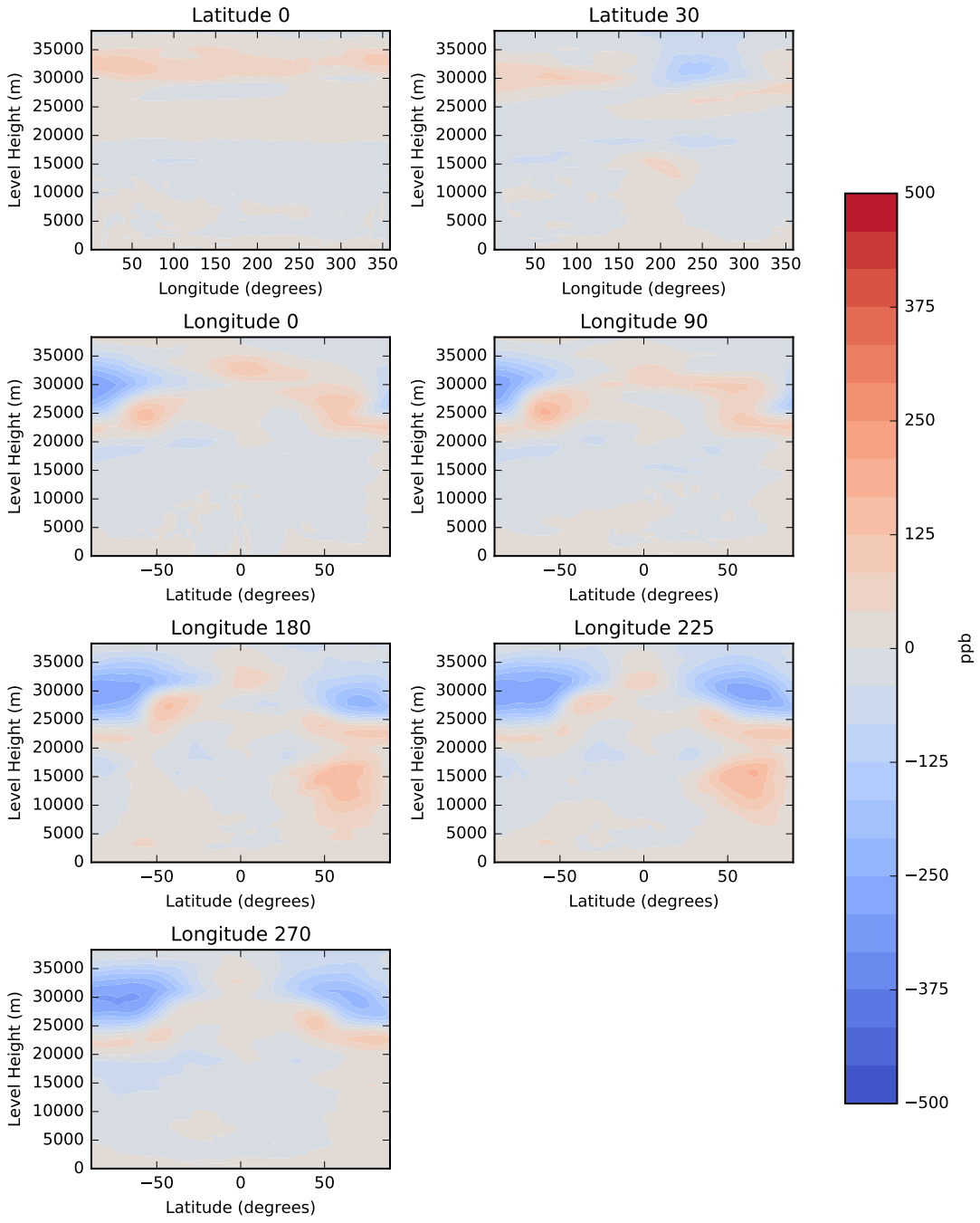

Figure 4.7: Differences O_3 concentrations in the fast flaring simulation. We show the change compared to the control run (i.e. a positive value shows an increase in O_3 concentration over the control run).

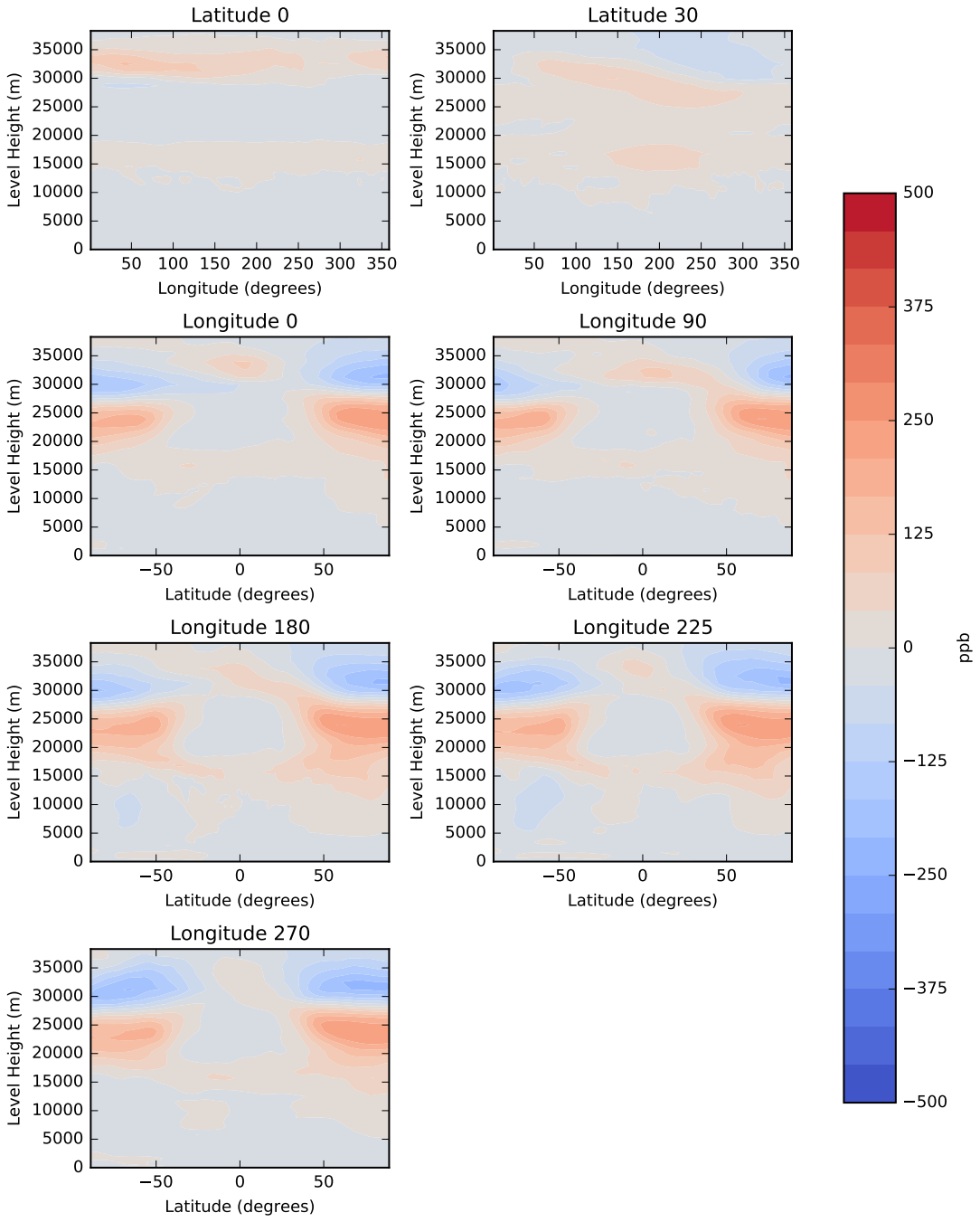

Figure 4.8: Differences O_3 concentrations in the slow flaring simulation. We show the change compared to the control run (i.e. a positive value shows an increase in O_3 concentration over the control run).

4.4 Comparison of planetary orbits

4.4.1 Earth orbit

We simulate the same planet as in the previous chapter, except placed in Earth's orbit to present a simplistic comparison between Earth and an M-dwarf planet. We do not intend to conduct a full analysis of the climate of an exoplanet in an Earth-like orbit in this work – many studies of this type have been conducted in the literature, and such simulations could easily fill several more chapters (see e.g. Showman et al., 2009; Showman et al., 2013; Kaspi and Showman, 2015). Our results are presented to place our M-dwarf simulations in context, giving a point of reference for ozone columns, surface temperatures and surface UV radiation on a waterworld with a simple ozone-based chemistry scheme in an Earth-like orbit.

For these simulations, we use the UKCA default stellar (i.e. solar) spectrum and Earth's planetary and orbital parameters. These are provided for comparison in Table 4.2. As the Earth's rotational axis is inclined relative to its orbit and the orbital period is long, the results here are presented as annual means rather than our typical 120 day means shown in the other simulation results.

We examine first the key atmospheric parameters presented in Figure 4.9, which shows the same atmospheric parameters as Figure 3.2 from the previous chapter. In this case, since there is no permanent day and night side we simply show mean profiles over the entire atmosphere, and note that the axes are different from those in the previous figure. Beginning with the temperature profile, we find that in the Earth simulation there is a strong thermal inversion above 15 km, which is not present in the other simulations. The upper atmosphere is warmed by the much more significant high-energy photon flux from the star, which is absorbed by the ozone layer. Comparing the UV flux and temperature profile, we see that the increasing temperatures are associated with falling UV flux. This does not occur in the tidally-locked and 3:2 orbits; in these

Parameter	Value
Semi-major axis /AU	1
Stellar irradiance /W m^{-2} ($S_\oplus$)	1360 (1)
Orbital period /Earth days	365.25
Ω /rad s^{-1}	7.292116 $\times 10^{-5}$
Eccentricity	1.671 $\times 10^{-2}$
Obliquity	0.4091 (23.44°)
Radius /km ($R_\oplus$)	6371 (1)
g /m s^{-1}	9.807

Table 4.2: Planetary parameters for the planet in the Earth orbit.

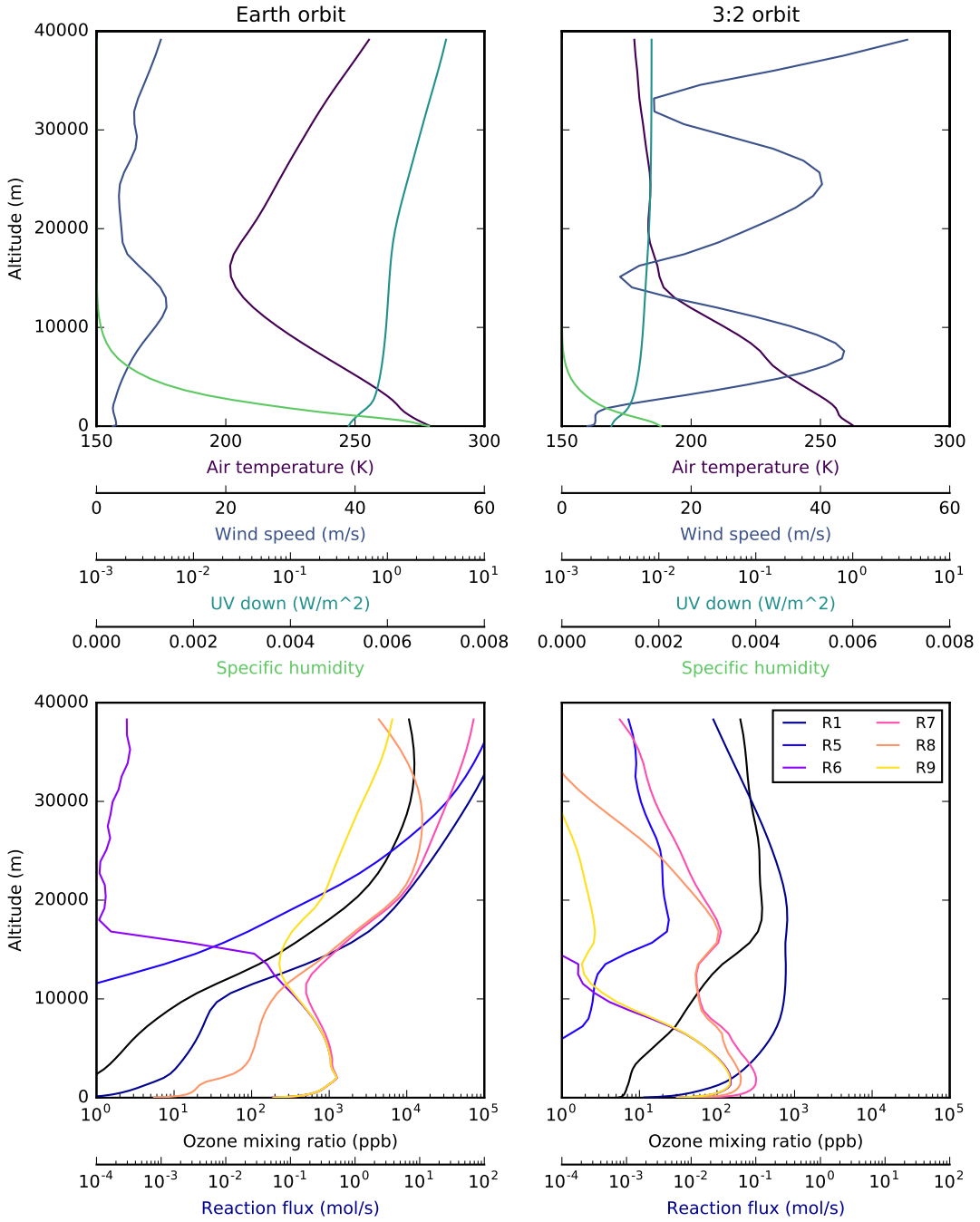

Figure 4.9: Atmospheric properties in the 3:2 and Earth orbits, as compared with Figure 3.2. We note that the axes are different between the these plots and the former, though we maintain the same axes between the two simulations presented here. Since these orbital configurations do not have a permanent day and night side we show whole-atmosphere means rather than the day- and night-side profiles shown in Figure 3.2.

cases we see less UV absorption at higher altitudes and a colder upper atmosphere. For these cases we see less attenuation at high altitudes and a more significant decrease in UV intensity at lower altitudes. Our simulations with the chemistry switched off (and therefore an Earth-like ozone layer) also show increased upper-atmosphere temperatures due to this heating. The absorption of UV at high altitudes is also indicated in the reaction fluxes in the lower panels.

At the surface, we find much higher temperatures in the Earth simulation, driven by the greatly increased insolation. We show the longitudinally averaged surface temperatures in Figure 4.10 along with surface temperatures for the 3:2 and tidally-locked simulations. We find surface temperatures ranging from 260 K at the poles to over 280 K at latitude 0. Comparing with the other two runs, we see the effects of the planetary obliquity, resulting in a flattened surface temperature profile and smaller equator-to-pole gradients. Overall the area with a mean temperature above 273 K is greatly increased, extending out past latitude $\pm 50^{\circ}$. For a fast-rotating planet without extreme day-night temperature contrasts this indicates that these latitudes are likely to have liquid water for most of the year. Our tidally locked simulation presents a dramatic comparison; the mean surface temperature is vastly lower reflecting the extremely cold night side.

In the same figure we see the surface UV in each of the three simulations. Again we see a flattening across the equatorial latitudes caused by the planetary obliquity. Mean surface UV is $100\times$ higher in the Earth-like simulation compared with the M-dwarf simulations.

Returning to Figure 4.9, we find that the humidity is much higher in the Earth simulation. This is a direct consequence of the increased overall surface temperatures (caused by the stellar irradiation) driving convection.

We find much lower net wind speeds on the planet. With a much smaller day-night temperature contrast there is no driving force for persistent planet-wide super-rotation, such as that that appears on a tidally locked planet. However, looking at the mean zonal wind speeds throughout the atmosphere in Figure 4.12, our model suggests that there is a persistent wind structure on the planet. These winds roughly resemble annual zonal mean wind speeds on the Earth, with jet-like structures in the tropical latitudes, but differ in some ways; comparing with (for example) results from an standardised idealised case for an Earth-like planet such as those in Menou and Rauscher (2009) and Mayne et al. (2013) we find that our zonal wind structure is somewhat different. Particularly, the structure at the central latitudes in different. We see a ring of retrograde wind with a small central section that is super-rotating at an altitude of 20 km and extending only a few degrees north and south. However, our model setup is very different to that prescribed in these tests – notably, there is an enforced equator-to-pole temperature

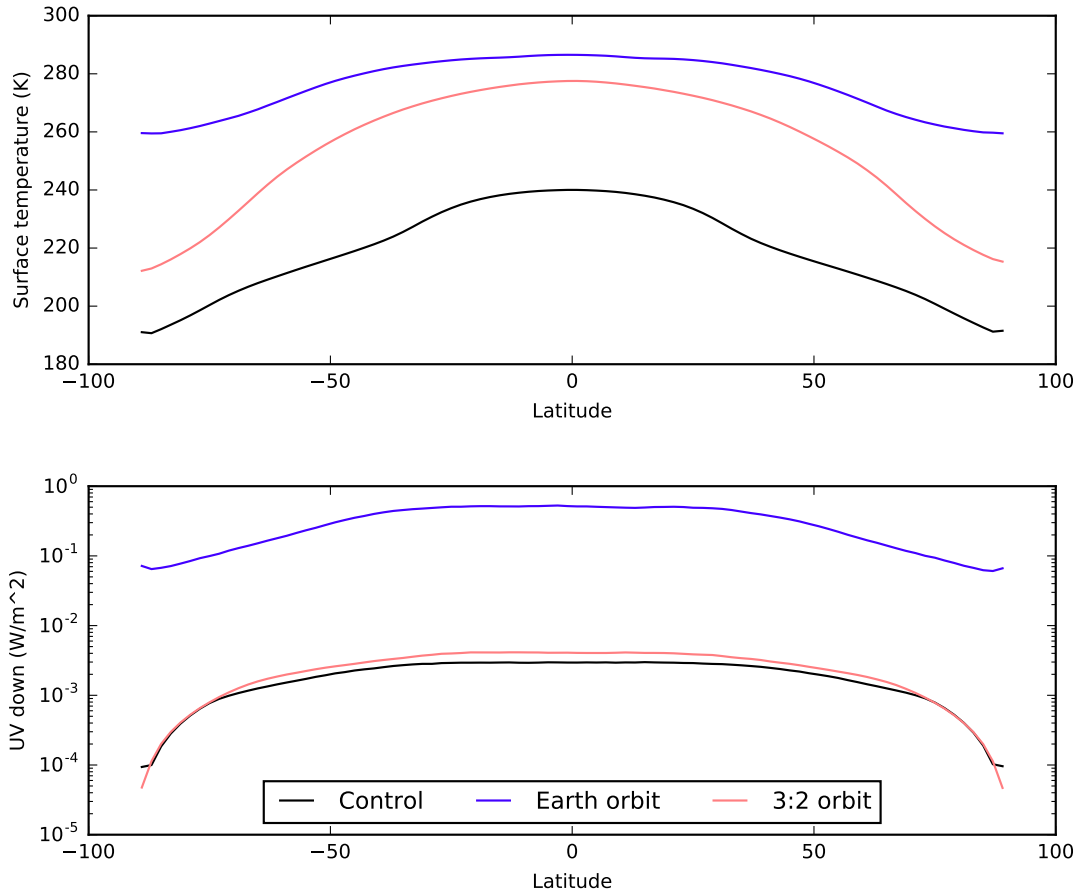

Figure 4.10: Zonal means of key habitability parameters at the surface in the 3:2 and Earth orbits.

difference, a prescribed vertical temperature relaxation profile, and other such changes which are intended to *approximate* annual mean Earth-like conditions but not describe it perfectly. We therefore expect some broad similarities in the global circulation; i.e., super-rotation at the tropics but the specifics will clearly be different.

As noted above, we refrain from a full analysis of the global circulation here. Our Earth simulations are simply intended to indicate some of the changes that occur in the planetary atmosphere as a result of the tidal locking and change in stellar spectrum, particularly with regards to the total ozone column, reaction fluxes, surface temperatures and surface UV.

We move on to discuss the lower panels in Figure 4.9. Comparing our ozone profile between this simulation and that in Figure 3.2, we find that maximum mean ozone concentration is greatly increased in the Earth case. We find a maximum mean ozone concentration of just over 10 ppm at 35 km compared with the tidally locked case where a maximum ozone concentration of 750 ppb occurs between 25 and 30 km (with

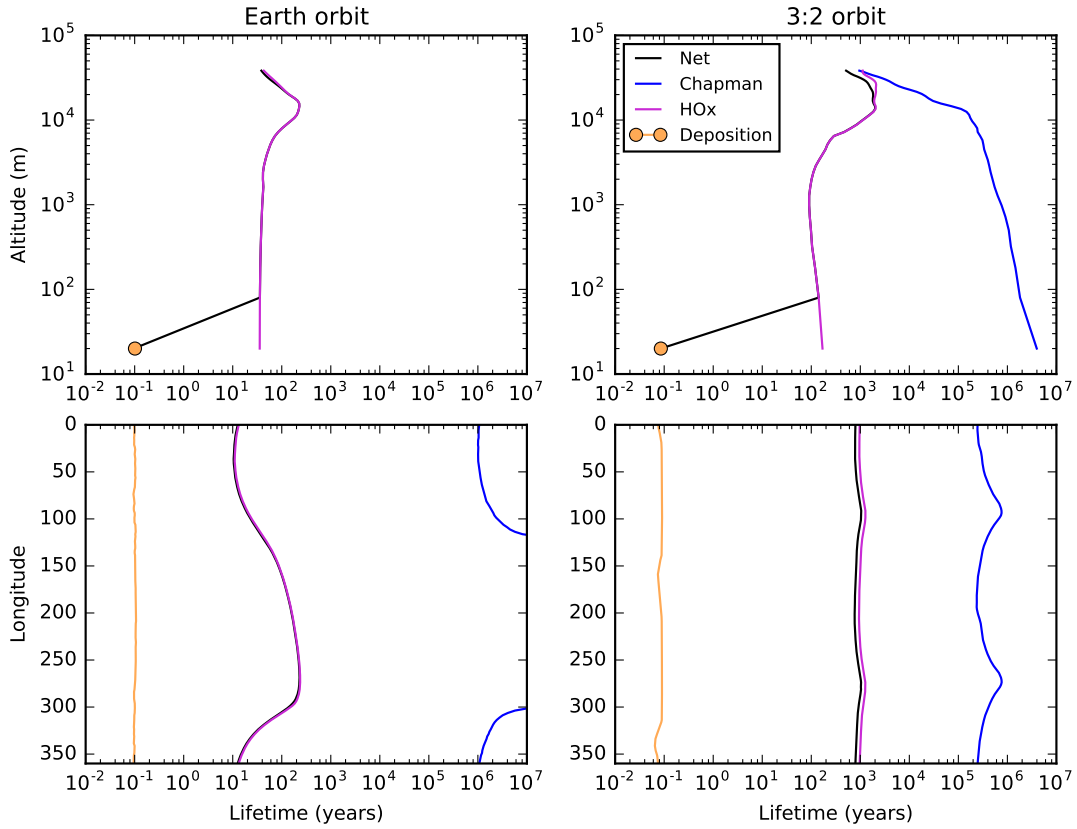

Figure 4.11: Ozone lifetime in the 3:2 and Earth orbits. For the Earth orbit, our model output is captured at the same time every day, allowing us to show the day ($-60° - 120°$) and night ($120° - 300°$ side separately.

lower altitude and mean concentration on the night side). The ozone concentration aligns neatly with reaction fluxes, with almost all of them peaking at high altitude where UV flux is high. For the Chapman mechanism reactions R1 and R5 this is as expected. The exception is the reaction flux for R6 which is limited by water vapour rather than UV intensity. R7 and R8 also show an increase in reaction flux at low altitude exactly in line with the R6 flux. The low reaction flux of R6 at high altitude, in contrast with the large fluxes of R7, R8 and R9, indicates that the OH and HO_2 must be efficiently transported to the stratosphere.

Overall reaction fluxes are much larger in these simulations by $2 - 3$ orders of magnitude. This aligns with the $100 - 1000\times$ increase in UV flux, as one expects for a set of chemical reactions that are strongly dependent on photon availability.

We look at the atmospheric ozone in more detail in Figure 4.13. We expect to see almost no longitudinal structure due to the relatively fast rotation (compared to chemical lifetime and transport rates), and this is indeed the case, with little to

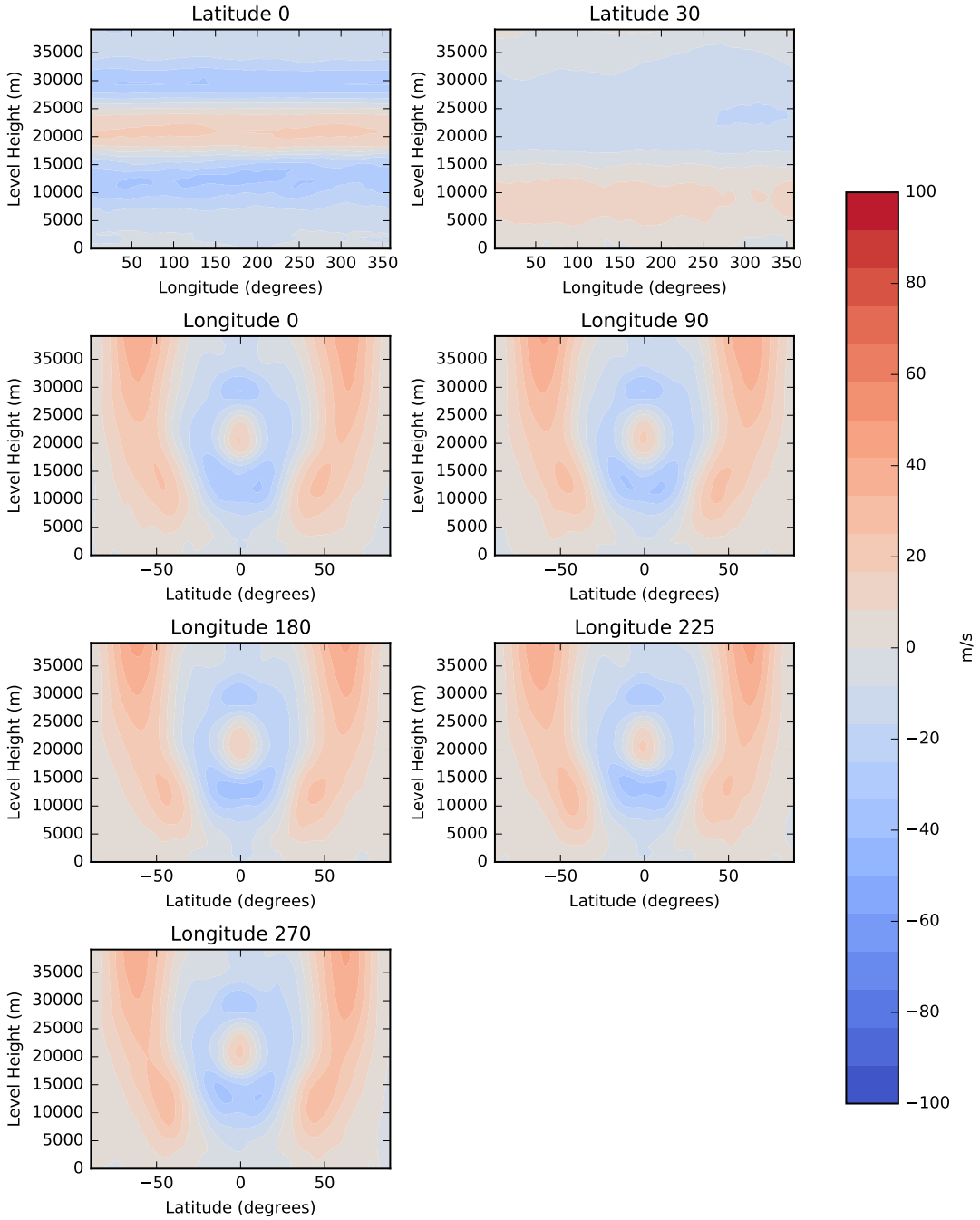

Figure 4.12: Zonal wind speeds in the Earth orbit.

no variation in the longitudinal slices and zonally uniform ozone columns. Total atmospheric ozone is much higher in this simulation, as expected, due to the change to the solar spectral energy distribution and much stronger UV flux. We find maximum ozone concentrations of $10 - 20$ ppm, as on Earth, and ozone columns of around 300 Dobson units.

We show the ozone lifetime in more detail in Figure 4.11. Note that through synchronisation of the model output timesteps and the planetary day length we capture the day and night side lifetimes for the Earth orbit.

We find that the ozone lifetime against the Chapman mechanism is actually longer in the Earth simulation by nearly a full order of magnitude. This reflects the increased ozone production and burden in the Earth case rather than a reduced loss rate. Returning to the Chapman mechanism in subsection 3.1.1 we can infer that the ratio of 240 to 320 nm photons will determine the equilibrium between O_3, O_2 and O. In the Earth simulation, the greatly increased abundance of 240 nm photons means that ozone production outstrips the loss through R3, dramatically increasing the ozone lifetime in this mechanism. On the night side the ozone lifetime against the Chapman mechanism is again extremely long (essentially infinite) due to the lack of UV photons. We find again that the HO_x mechanism is by far the more important mechanism in the atmosphere, completely dominating the net ozone lifetime with the exception of the planet's surface, where deposition dominates.

Again we see a gradual increase in ozone lifetime as we pass from the day side towards the night side, indicating the depletion of OH and HO_2 through R9. In this case the gradient is due to the rotation of the planet as opposed to transport time from the day side as in the tidally locked simulations. That is, during the day time R6 produces OH, and as the sun sets at a given longitude the flux of R6 drops off and R9 gradually depletes the OH and HO_2. As the sun rises R6 rapidly starts up again.

Our deposition rate is constant on the planet as there are no surface features, thus we find similar lifetimes against deposition in all simulations.

4.4.2 3:2 resonant orbit

The orbital parameters of Proxima Centauri b are not certain (Anglada-Escudé et al., 2016; Brown, 2017), and more generally there are range of stable planetary orbits in the CHZ of an M-dwarf star (Shields et al., 2016). Following Paper I, we therefore run the model in a 3:2 resonance. We maintain the orbital parameters from Paper I, which are given in Table 4.3. Rather than using several values of eccentricity, we use only the 0.3 value, ignoring the more circular orbits. The stellar spectrum is identical to that used in our standard tidally-locked M-dwarf planet case, given in Figure 3.1. We note

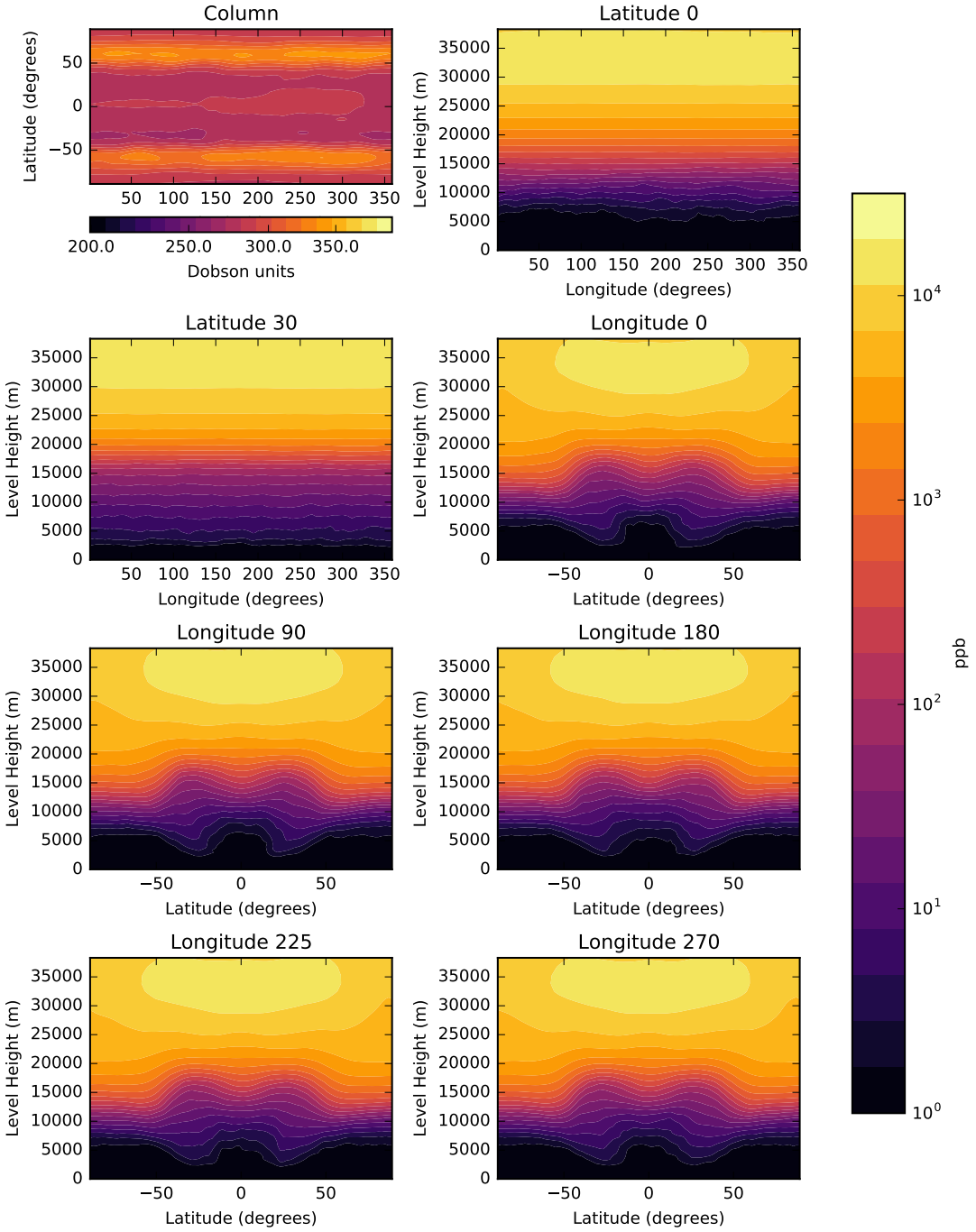

Figure 4.13: Atmospheric O_3 in the Earth orbit

Parameter	Value
Semi-major axis / AU	0.0485
Stellar irradiance / W m^{-2} ($S_\oplus$)	881.7 (0.646)
Orbital period / Earth days	11.186
Ω / rad s^{-1}	9.7517 $\times 10^{-6}$
Eccentricity	0.3
Obliquity	0
Radius / km ($R_\oplus$)	7160 (1.1)
g / m s^{-1}	10.9

Table 4.3: Planetary parameters for the planet in the 3:2 resonant orbit.

that in Paper I, the atmosphere used in the 3:2 simulations was the nitrogen dominated one, rather than the Earth-like atmosphere.

We first examine the key atmospheric parameters in the top panels of Figure 4.9. We see immediately that this simulation bears some similarities with the tidally locked control run. Air temperatures in the two models are similar, with similar upper and lower atmosphere lapse rates, but the 3:2 run has a slightly increased surface temperature. We see that in both cases there is a triple jet structure, but this is much stronger at lower altitudes in the 3:2 run and resembles the low-altitude jet on the night side of the tidally locked planet. The UV radiation in the two runs displays similar attenuation; in both cases the UV reduction at high altitudes is smaller than in the Earth-like simulation reflecting the smaller amount of high-energy UV compared with the solar radiation. Despite the differing axes in the two plots, the total humidity is similar to the day side humidity in the tidally-locked model. On the night side of the tidally locked planet there is little to no convection due to the extremely low temperatures; here temperatures are much more uniform due to the fact that the entire surface receives radiation from the star (albeit non-uniformly) resulting in uniform convection. This was also found to be the case in Paper I.

We show the zonal winds in the 3:2 simulation in more detail in Figure 4.14. To first order the winds are similar between this run and the tidally locked run; however, it is notable that there are very few areas with retrograde wind in this simulation in contrast with the tidally locked planet. This circulation resembles that of Venus, which rotates slowly (but with an orbital period of approximately 200 days compared to 11 days here) (e.g. Lebonnois et al., 2016). Even ignoring the fact that the entire surface is (at some time) exposed to the stellar radiation, this circulation will prevent the accumulation of ozone like in the tidal case. We therefore expect much better mixing of ozone.

We do not see any significant longitudinal variations in the structure of the

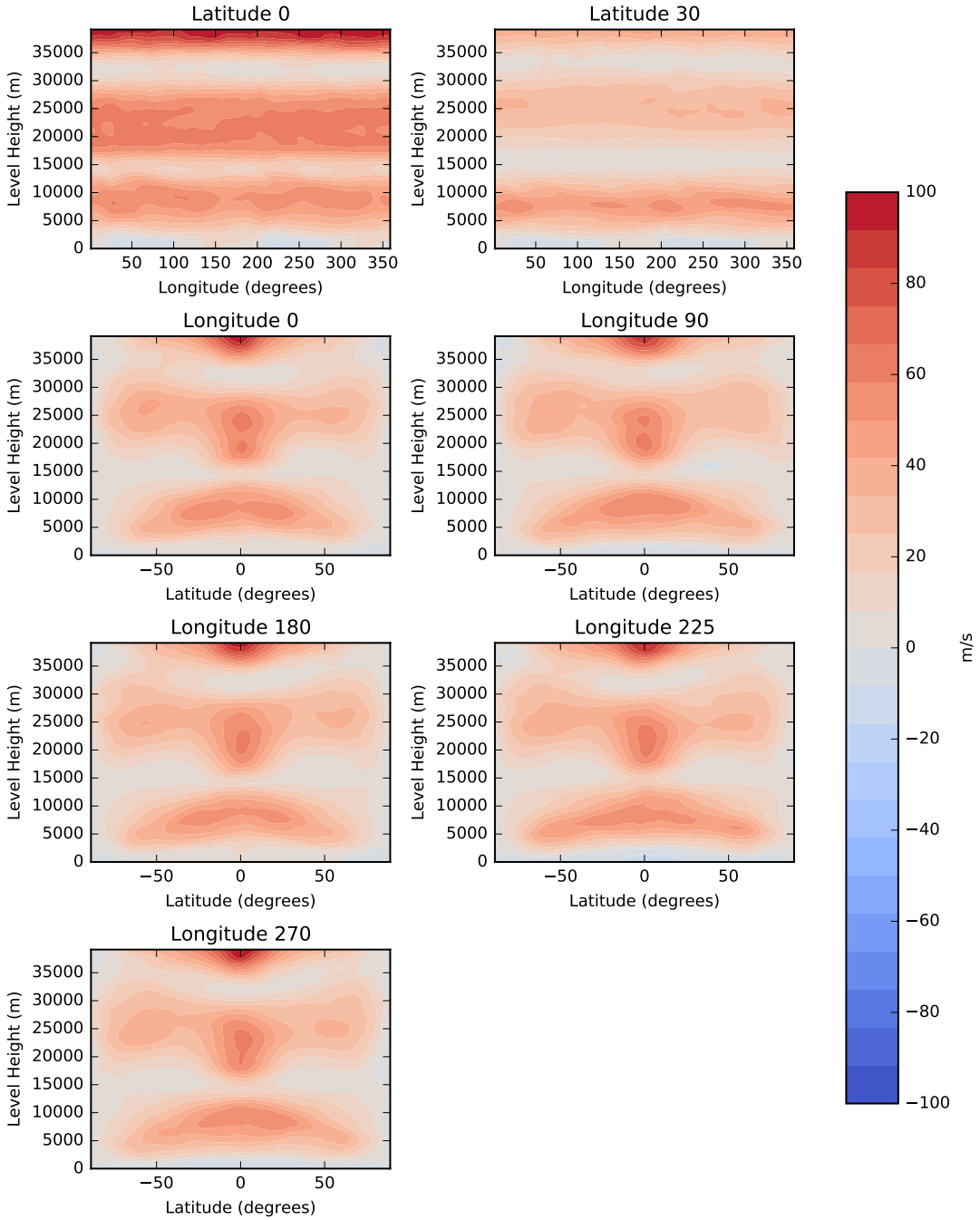

Figure 4.14: Zonal wind in the 3:2 resonant orbit.

jets, despite the slightly non-uniform surface temperatures in this model. We show the surface temperature and surface UV in more detail in Figure 4.15. Our surface temperatures show good agreement with Paper I. We find similarly low surface temperatures around the equatorial latitudes with only some parts of the surface – those that receive increased stellar flux due to the synchronisation of the orbit and rotation – staying above 273 K. Our pole temperatures also agree here, being around 215 K. This contrasts with the tidally-locked orbit where the inclusion of our chemistry results in colder poles compared with Paper I. We see in Figure 4.10 that the 3:2 orbit has much higher surface temperatures around lines of longitude compared with the tidally locked simulation; however, there is a much larger equator-to-pole temperature gradient, which an important parameter for investigation of snowball states.

Naturally we find that the longitudinal mean surface UV is extremely similar between the two M-dwarf planets. With the exception of the effects of absorption by ozone and the eccentricity of the orbit the total received radiation should be identical in the two simulations. Returning to the lower panel of Figure 4.15, we see the spatial distribution of mean UV at the surface. We find maximum (mean) surface UV flux of around 0.01 W m^{-2} at longitude 180°. We also find that the UV flux shows some granularity due to the effects of clouds, as in the tidally-locked case. (In the 3:2 case there is significant planet-wide cloud cover; see Figure 10 in Paper I.) The UV flux naturally is proportional to longer-wave incident radiation; we see that hottest parts of the atmosphere are aligned with the most illuminated parts.

Returning to Figure 4.9, we examine the profiles of the interesting chemical parameters. The similarities between the day side of the tidally-locked planet in Figure 3.2 and the 3:2 planet are again immediately noticeable. We find similar maximum mean ozone concentrations, though slightly lower on the 3:2 planet; we also find that the ozone layer is less sharply defined with more high altitude ozone. (Note that the in the 3:2 case the ozone concentration is presented on a log-scale as opposed to the linear scale for the tidally-locked planet.) Reaction fluxes are broadly similar, though fluxes are lower in the 3:2 case than on the day side of the tidally-locked planet (though of course we are taking the mean of the whole atmosphere here rather than just the day side).

We show the atmospheric ozone in Figure 4.16. From Figure 3.20 we know that when subjected to M dwarf UV flux the ozone lifetime throughout the atmosphere is much longer than the orbital period; thus we do not expect to see any real longitudinal structure in the ozone column, as the rotation of the planet (and air) is faster than the important chemical timescales. This is indeed the case, as seen in column in the top left plot. We do see a lower ozone column at the equator with increased ozone at the poles; such a situation occurs on the Earth and to some extent in our Earth-like

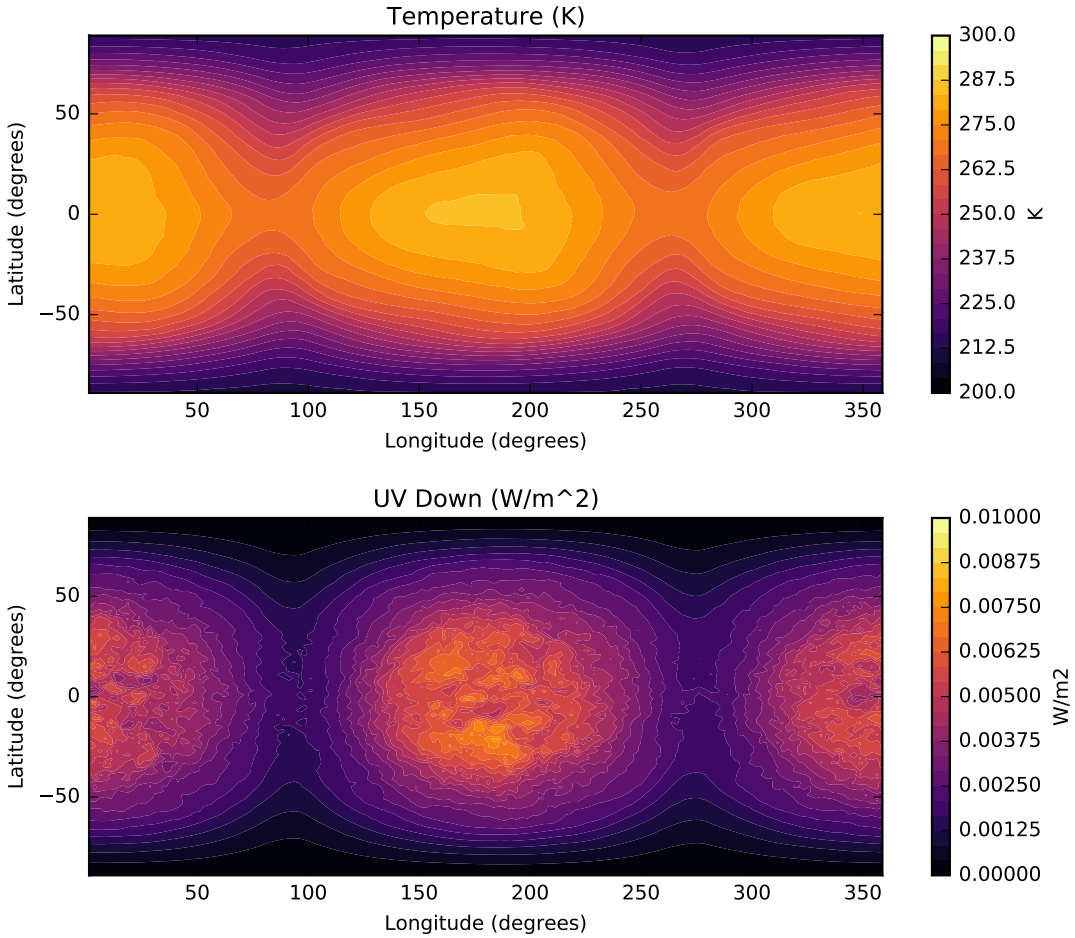

Figure 4.15: Surface conditions in the 3:2 resonant orbit

simulation described above.

Looking to the longitudinal and latitudinal slices, our ozone layer again resembles that on the Earth. However, comparing with the Earth-like simulation we find that the ozone layer is lower in the atmosphere, as in the tidally-locked case. Above 15 km the ozone layer is extremely uniform. Below this point we see an increase in ozone at the poles aligning with the ozone columns.

Finally, we return to Figure 4.11 to see the ozone lifetime against each set of reactions. We see that ozone lifetime mirrors day-side lifetime in the tidally-locked case (Figure 3.20), but overall lifetimes are shorter in the 3:2 orbit. The shorter ozone lifetimes in the 3:2 orbit reflect the more uniform chemical environment, with no areas on the surface that have extreme ozone lifetimes such as the cold traps on the night side of the tidally-locked planet. This is also reflected in the longitude plots, showing some spikes at areas of low instellation but mostly uniform. As in all other simulations we find that HO_x is the main ozone loss mechanism, dominating the ozone lifetime, with the Chapman mechanism equalising at very high altitudes and the deposition dominating at the surface.

4.4.3 Discussion

Our results demonstrate the difference between a tidally-locked M-dwarf planet and a planet like Earth in a simple fashion. The habitability of the surface is more questionable for a planet like Proxima Centauri b (assuming an Earth-like composition); the planetary orbit, the global circulation and the stellar environment result in a climate is more volatile, with extremely cold temperatures on the night side and intense wind speeds. As demonstrated in section 4.2, even small changes in total ozone column result in extreme changes on the night side of the tidally locked planet. By contrast the rapid rotation and obliquity of the Earth results in a homogenisation of the climatic features across longitude and latitude, resulting in a more temperate surface and more uniform chemistry. The same is true in the 3:2 orbit; though there is some spatial inhomogeneity the atmospheric features are broadly similar across longitudinal bands.

Based on the uniformity of the ozone layer in these simulations, we speculate that they will be less sensitive to the removal of chemistry. Certainly in the case of the Earth-like planet, with a prescribed Earth-like ozone layer, the results should not change drastically. In the 3:2 case, the temperatures around lines of longitude are more even, and the (eventual) irradiation of every point in the atmosphere should mean that dark parts of the surface do not achieve the extreme cooling or warming observed in the tidally-locked case. Our results also do not differ significantly from those in Paper I, even though their simulation did not include an interactive ozone layer, suggesting

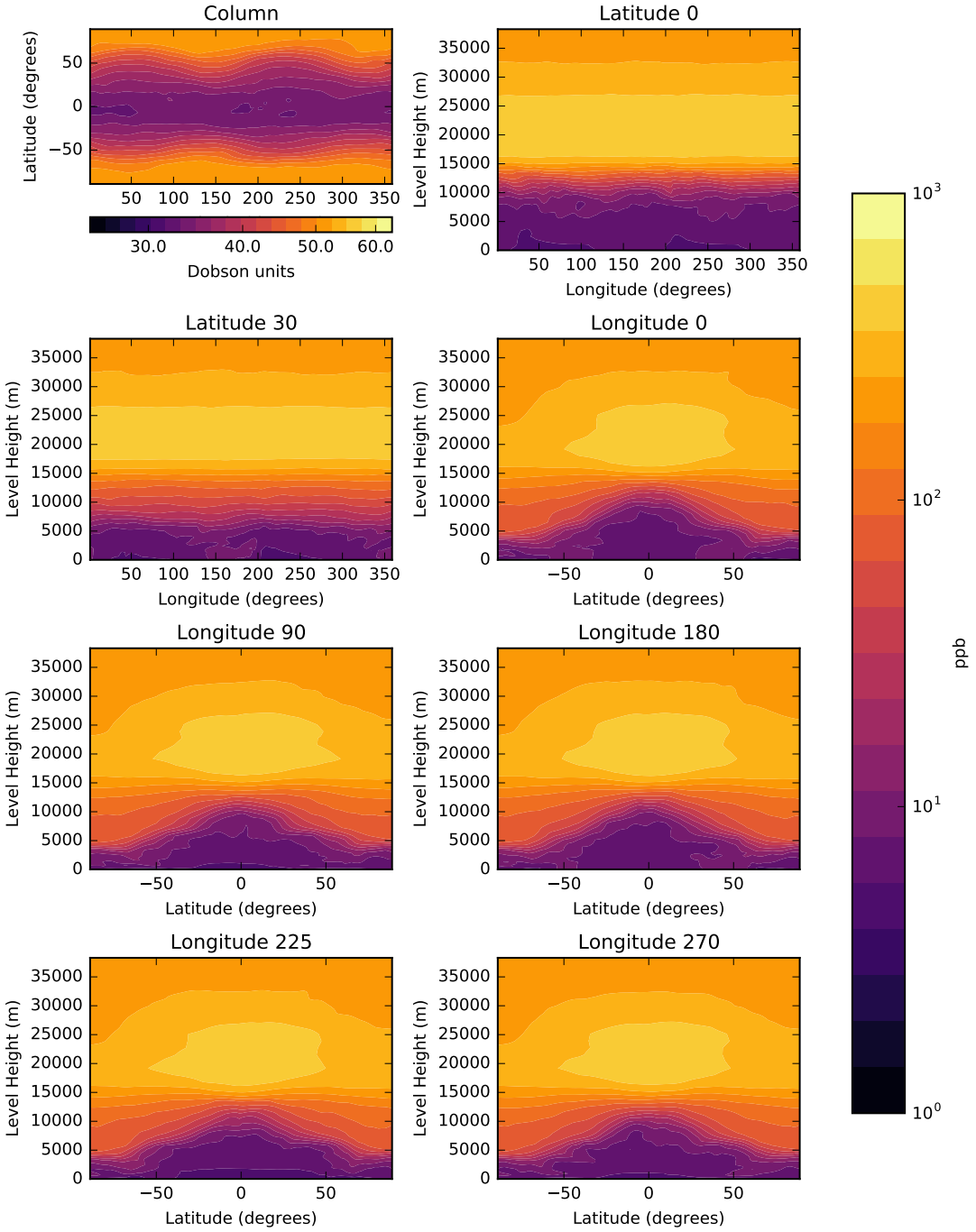

Figure 4.16: Atmospheric O_3 in the 3:2 resonant orbit.

that the effect of the chemistry on the climate is more limited here. However, further investigations with the chemistry switched off for these models would clarify this.

4.5 Conclusions

We have presented here a range of simulations that examine the impacts of certain planetary parameters on the habitability and atmospheric chemistry of our M-dwarf planet.

We started by examining the effect of including a chemistry scheme in the model in section 4.2. We found that the global circulation is extremely sensitive to the night-side radiative cooling rate, in agreement with Paper I, analytical calculations from Heng and Kopparla (2012) and the simple model of Yang and Abbot (2014). In our simulations (and in Paper I) the night side of the planet is extremely dry with very little cloud, such that the radiative cooling rate is determined by the night-side ozone columns, which is a significant infrared absorber in the atmosphere. Our inclusion of an online atmospheric chemistry scheme, and the resulting ten-fold decrease in ozone column, thus dramatically alters the global circulation. We observe several effects as the ozone column increases:

- the night side of the planet, between the terminator and the anti-stellar point (longitudes 90° to 180°), warms significantly. Warming is more than 50 K at some points on the surface in the case of a ten-fold increase in ozone column.
- the poles of the planet heat up significantly
- the cold traps move eastward towards the terminator and towards the equator.

Even a small increase in the ozone column caused by the removal of the HO_x catalytic cycle (circa 10% change in ozone column) is enough to change night-side temperatures by 20 K at some locations.

This is a clear demonstration of the value of a full, online photochemistry scheme incorporating transport; without the chemistry scheme one would have to run simulations with a range of ozone layer geometries and thicknesses in order to capture the night-side behaviour. Even then, whilst the appropriate prescribed ozone fields could describe the change occurring through the night side cooling mechanism, this ensemble approach yields no information about the chemical state of the atmosphere; our simulations produce chemistry that is consistent with the stellar radiation and planetary dynamics. It would be possible to deduce (for example) that night side ozone columns particularly at the cold traps are likely to be enhanced over the day side columns through a consideration of temperatures, wind vectors, transport time and so on and then feed this back into the model through a new prescribed ozone field, but at this stage one has simply built an extremely inefficient online chemistry scheme.

Following on from these simulations, we examined the sensitivity of the model to the initial abundances of our chemically-active tracer species. We found that a 10^6 enhancement of HO_x species over O_x species was enough to destabilise the model to the point where it did not reach equilibrium within 10 years. Model runs are ongoing but these simulations demonstrate the sensitivity of the climate to the chemistry.

We subsequently examined the effect of electromagnetic flares on our model atmosphere. In line with results from the literature, we find that the flaring has next to no effect on our total ozone column (Segura et al., 2010; Tilley et al., 2017; Howard et al., 2018). Our results tentatively suggest that the flaring results in decreased atmospheric ozone concentrations at high altitudes over the poles; if the results are robust it may indicate that 1D models cannot capture the behaviour of ozone under flaring. However, the aforementioned sensitivity to night side ozone columns, sensitivity of the model to initial chemical composition, and the fact that our flares were switched on during the model spin up mean that more model time is needed to properly understand the end state of these simulations.

Finally, we briefly examine the atmosphere in two different orbits: an eccentric 3:2 resonant orbit and an Earth-like orbit at 1 AU with a solar spectrum. For both of these simulations we find that the decreased spatial inhomogeneity results in a more uniform ozone layer with much more moderate temperatures arising from the instellation. Our Earth-like orbit illustrates the difference between the ozone layer on a planet like Earth and a planet like Proxima Centauri b – the ozone layer is much thicker on the former with ozone columns around ten times larger than on an M-dwarf planet. Total atmospheric ozone and ozone lifetime between our two M-dwarf orbits is similar; this demonstrates that the total ozone is controlled by the availability of UV photons. However, as mentioned, the ozone layer on the tidally-locked planet shows much more non-uniformity, reflecting the difference in atmospheric dynamics arising from the orbital configurations. Our planets in 3:2 and Earth-like orbits are not thought to be as sensitive to the inclusion of chemistry; further model runs will examine the impact of switching off the chemistry scheme in these runs, as in the case of the tidally-locked planet above.

CHAPTER 5

Discussion and Conclusions

In the preceding chapters we have tried to assess some of the factors affecting habitability outside of the Solar System. In Chapter 2 we looked at a new environment that had not previously been considered for its habitability qualities, namely a cool Y dwarf atmosphere. In Chapter 3 and Chapter 4, we developed a model that served two purposes: firstly, increased understanding of one factor determining planetary habitability, namely the ozone layer (which protects the surface from harmful radiation); secondly, we evaluated the importance of atmospheric chemistry in terms of feedbacks on the climate system, in order to test the validity of commonly made assumptions in atmospheric modelling studies of planetary habitability. Our results showed that atmospheric chemistry feedbacks are perhaps more important than previously thought and demonstrate the value of full coupled 3D photochemistry models that have historically not been used in habitable exoplanet atmosphere modelling. We discuss the findings from these chapters in more detail below. Following this, we suggest some changes to the model and further simulations that would mitigate some of the weaknesses of our suite of model runs and allow further investigation.

5.1 Summary of findings

5.1.1 Habitability of cool brown dwarf atmospheres

In Chapter 2 we explored the habitability of an ultra-cool brown dwarf atmosphere. We suggested that there is likely to be a region in the atmosphere of a cool Y-dwarf where temperatures and pressures are likely to be amenable to Earth-like life and there are thought to be water clouds. We denoted this region the atmospheric habitable zone (AHZ). The AHZ sits above an uninhabitable environment, in this case a hot dense atmosphere. We explored the habitability with a model organism, which was based on previous work that explored the habitability of the Jovian atmosphere.

We assumed a constant upward vertical velocity through the AHZ, which we surmise occurs in zonal jets. We modelled organisms that float in the convective updrafts. The model organisms were allowed to evolve towards an "ideal" geometry for the updraft by the removal of organisms that failed to stay aloft or rose too high and reproduction of organisms that succeeded, with organism properties being passed onto offspring with some randomness. We found that the organism geometry is most sensitive to the magnitude of the atmospheric convection. Stronger convective winds support the evolution of more massive organisms due to the change in sinking rate. We found that organisms in strong convection had dimensions on par with Earth microbes and weaker convection resulted in organisms that were similar in size to viruses.

We calculated the occurrence rate of Y-dwarfs based on the limited observational evidence, and found that there were likely to be on the order of 10^9 in the Milky Way with several within the local neighbourhood of the Sun. Assuming that such an AHZ is possible and that life can begin in such an environment, we find that similar bodies represent a large increase in the number of possible habitable environments in the galaxy. Finally, we discussed the implications and limitations of our simulations.

5.1.2 Modelling atmospheric ozone on M-dwarf planets

In Chapter 3, we described the development of an advanced simulation of atmospheric chemistry using a 3D coupled photochemistry scheme and GCM. The model was adapted version of the Met Office Unified Model. Our chemistry scheme used a simple description of the reactions that can produce an ozone layer in the Earth's stratosphere (those being the Chapman mechanism and the hydrogen oxide catalytic cycle). These mechanisms involve oxygen, water and UV photons. Our model was loosely based on observed orbital parameters for Proxima Centauri b, in line with Boutle et al. (2017).

The key result from our simulations was that a tidally-locked planet orbiting an

M-dwarf can develop an ozone layer despite the low UV fluxes. Previous simulations have demonstrated this but no studies have been conducted in 3D.

Following on from this our 3D simulations showed that atmospheric ozone is spatially non-uniform, especially between the day and night sides. We did see the typical Earth-like ozone concentration at the ozone layer altitudes, but we also saw a significant increase in ozone at low altitude on the night side above the cold traps. We found that total ozone columns were around 10 times smaller than for Earth. We suggested that spatial non-uniformity in chemical species might be an interesting feature for observers, though we did not investigate detectability.

The spatial distribution of ozone arose because of the long chemical lifetime (years) on both sides of the planet but particularly on the night side. Chemistry timescales were increased meaning that transport became more important. This is why we saw an accumulation of ozone at the cold traps; transport from these points to the day side is very slow due to the gyre structures. We found that there was more ozone loss through the hydrogen oxide catalytic loss cycle than through the Chapman mechanism.

Comparing climatological factors with Boutle et al. (2017) on which our simulation is based, we found that the simulation with the online chemistry scheme has a decreased stratosphere temperature, further reduced humidity and reduced maximum and minimum surface temperatures by 3 K. However, differences between the two model configurations, such as the adjusted model grid and removal of low-MMR greenhouse gases prevented us from directly attributing all of the observed changes in the model output to the chemistry scheme.

5.1.3 Sensitivity of ozone and climate on M-dwarf planets

Leading directly on from the preceding chapter, we investigated the effects of switching off atmospheric chemistry in the model. Without the online chemistry scheme the model defaults to an ozone layer that is Earth-like, with columns being around 10 times larger. These simulations showed that model results with and without chemistry were significantly different. The cause of this was determined to be the ozone columns. On the night side of the planet radiative cooling is highly efficient due to the lack of clouds and water vapour; the only remaining sources of opacity in the atmosphere are ozone and CO_2. The tenfold decrease in ozone columns therefore increased the night-side cooling rate, which drove the changes in the global circulation due to the importance of the day-to-night temperature gradient. The most significant changes were dramatic night side warming (more than 50 K at some locations), warming of the poles and movement of the cold traps towards the equator and eastward.

We followed these simulations with a comparison with and without the hydrogen

oxide catalytic cycle, which causes ozone loss. Removal of this cycle resulted in a small increase in ozone columns of around 10%, but this was still enough to drive the feedback described above and increase night-side temperatures by up to 20 K, warm the poles and move the cold traps. These results specifically demonstrated the importance of the 3D online photochemistry scheme in the climate system.

This was also shown in the next simulation, where we changed the initial fields of our chemically-active species. In this simulation we found that changing the relative abundances of the species in the hydrogen oxide catalytic cycle and the Chapman mechanism had a major impact on the model spin up time, such that our model run did not reach chemical equilibrium within 10 years. We are investigating this further.

Our penultimate simulations examined the effect of an electromagnetic flare on the planetary atmosphere. We subjected the planet to increased top-of-atmosphere flux on annual cadence. We found that ozone columns were very steady during and after flare, showing no significant ozone loss. Our findings here agree with those in the literature. The results from the runs were somewhat uncertain but the model runs above have indicated that the model is highly sensitive to ozone concentrations especially during the spin up period. Again we are investigating this further.

In the final set of runs presented in the chapter we looked at two orbits that were not tidally locked: an eccentric 3:2 resonant orbit around an M-dwarf and a 1 AU orbit with Earth-like obliquity, rotation rate and top-of-atmosphere flux. We maintained the same planetary configuration in these simulations, i.e. the Proxima Centauri b radius, a global ocean, atmospheric composition and so on. We found that the spatial dependence of the chemistry and climate were reduced due to the planetary rotation, and found similar total ozone columns between the two M-dwarf simulations and increased ozone column on the Earth orbit (by around 10 times). (Mean) ozone was much more homogeneous in these simulations. Our results from the first set of model runs in this chapter showed that (on a tidally-locked planet) the global circulation is sensitive to the atmospheric ozone; in further model runs we will switch off the chemistry scheme for the two orbits discussed here, allowing us to investigate the sensitivity of the global circulation to ozone when there is not such a strong day-night contrast.

5.2 Future work with M-dwarf planet simulator

The model of atmospheric chemistry on an M-dwarf planet has many further applications, being one of the first of its kind. Our analysis in the previous chapters has only scratched the surface of the parameter space that can be covered by this model. Below, we discuss some of our further research questions that arose in the course of the work presented in Chapter 3 and Chapter 4.

5.2.1 Addition of NO_x chemistry

As discussed in subsection 3.4.4, an interesting further step would be the inclusion of the NO_x catalytic cycle in our M-dwarf planet model, particularly as the precursors can be produced on the night side, unlike the reactants in the Chapman mechanism or HO_x cycle. It could therefore be a major sink of ozone on the night side and may radically alter the structure of ozone at, for example, the cold traps. We describe the key part of the mechanism below (Jacob, 1999):

$$\begin{aligned} & & \mathrm{NO} + \mathrm{O_3} \rightarrow & & \mathrm{NO_2} + \mathrm{O_2} & & \text{(R10)} \\ \textbf{Null cycle}: & & \mathrm{NO_2} + h\nu \rightarrow & \mathrm{NO} + \mathrm{O} & (\lambda \lesssim 400\mathrm{nm}) & & \text{(R11)} \\ \mathbf{O_3\ loss\ cycle}: & & \mathrm{NO_2} + \mathrm{O} \rightarrow & & \mathrm{NO} + \mathrm{O_2} & & \text{(R12)} \end{aligned}$$

The NO_x mechanism is initiated by the presence of atmospheric NO, which reacts initially with O to form NO_2. At this point there are two competing reactions; the null cycle and the O_3 loss cycle. In the null cycle the produced O and O_2 then recombine to form O_3 through the fast reaction R2 from the Chapman mechanism, resulting in no net loss of O_3. In the O_3 loss cycle, the NO_2 molecule instead reacts with an O atom that would otherwise cycle back into O_3, resulting in the net loss of two O_3 molecules (i.e. the reactant in Equation R10 and an O atom that would have combined with O_2 through R2). Here the relative abundances of NO_2, O atoms and actinic photons are critical to establish the lifetime of O_3; we note that with fewer high-energy photons, as in the case with an M dwarf planet, the O_3 loss cycle is (relatively) enhanced over the null cycle, which may result in a decreased O_3 lifetime depending on whether the reaction is limited by NO_2 or by O_3/photons.

On the Earth the removal of NO_2 from the atmosphere occurs through reaction with OH in the day time, forming HNO_3, or through reaction with O_3 in the night to produce NO_3, ultimately resulting in the production of N_2O_5. These species are removed either through precipitation or by photons but have long lifetimes in the atmosphere. Hence, given the differences in OH production and abundance, availability

of photons, lack of night-side water vapour and other factors, the mechanism is likely to work quite differently on an M-dwarf planet. In particular, if the reservoir species HNO_3 and N_2O_5 cannot be removed by precipitation or radiation, the O_3 lifetime may become much shorter.

A important uncertainty in this mechanism is the rate of NO_x production. Production through volcanism, space weather and lightning are poorly understood within the solar system, and thus the rate of NO_x production on an exoplanet may vary wildly. A range of emissions scenarios may provide constraints on tolerable emission fluxes for the O_3 layer to remain stable, and rule out some orbital or planetary configurations, such as those with significant volcanic activity driven by tidal heating.

NO is also produced through proton events during flares. The proton flux is capable of dissociating N_2 to produce two excited N atoms, which react with O_2 producing NO and O. Tilley et al. (2017) and Howard et al. (2018) found that this NO had a much greater impact on the total ozone column, reducing it by as much as 94% in 10 years. If the stellar activity rates are as high as this our modelled atmosphere will look radically different due to the sensitivity of the climate to ozone concentration.

Some work has been undertaken to attempt to quantify lightning strikes on exoplanets based on the small amount of data fromsolar system planets (Bailey et al., 2014; Ardaseva et al., 2017), and the UKCA has been used to study the interaction between lightning, NO_x and O_3 (Finney et al., 2016) in the past, so some of the framework for this study exists already.

5.2.2 Flaring

In section 4.3 we presented results from our flaring simulation. We discuss these in more detail below.

Stellar flux during a flare has a different spectrum to the quiescent stellar radiation. Typically a flare is modelled by a blackbody spectrum of higher temperature; for example, Howard et al. (2018) model an observed Proxima Centauri flare by a 9000K blackbody spectrum. Naturally, a high-temperature blackbody spectrum has proportionally more high-energy radiation than the 3000K M-dwarf spectrum, thus the (photolytic) effects on the atmosphere are significantly enhanced. Flares also are often accompanied by a stellar wind, and the constituent charged particles can have a particularly pronounced effect on the atmosphere, breaking apart molecules that are normally inert (such as N_2) (Segura et al., 2010; Tilley et al., 2017). This is one source of the NO_x species described in the previous section, and with the addition of that mechanism to the chemistry scheme we could parameterise proton events.

Hence, these simulations likely present a underestimate the impact of a flare on

the planetary atmosphere. However, they do show excellent agreement between our model and that of Tilley et al. (2017), who use a similar atmosphere with Earth-like values of O_2, CO_2 and N_2, all of which are included in their photochemical model. In that work, the authors use a 1D model with 55 species and 217 reactions; here our chemistry scheme includes only 9 reactions and 9 species, some of which do not interact chemically.

Future work should include an examination of a range of flare spectra, with parameterisations for stellar wind (e.g. through the NO_x reactions). This would allow us to understand how the flare affects the planetary dynamics, which we have already shown are very sensitive to ozone concentration, by contrasting our results with those of Tilley et al. (2017).

Furthermore, stellar activity does not strictly follow a regular cycle. In our simulations we provide an annual timeseries at a 1-hour cadence, $x(t)$, for the stellar activity. This time series is repeated, subjecting the planet to a single annual flare. A more advanced simulation might include an element of stochasticity with flare intensity and cadence given by a flare frequency distribution. For example, there is no possibility of back-to-back high energy flares in our simulations; these could have a devastating effect on the planetary surface if of sufficient energy. Based on observational data over approximately 2 years, Howard et al. (2018) defines a flare frequency distribution for Proxima Centauri as:

$$\log(\nu) = -0.98^{+0.02}_{-0.24} \log(E) + 30.6^{+0.83}_{-7.6} \tag{5.1}$$

where E is flare energy (in ergs) and ν is frequency of flares of energy greater than or equal to E per day. Simulation of flares according to a law of this type would present a more realistic view of the habitability of Proxima Centauri b.

Finally, we only run the radiation code once per hour (i.e. every fifth timestep), thus the minimum duration of our simulated flare is one hour. This is the default timescale in the model and is naturally intended for simulations of the Earth, where TOA radiation is (relatively) predictable. A more detailed simulation would perhaps use a reduced radiation (and consequently chemistry) timestep. This would mean a severe performance decrease – radiation and chemistry timesteps are long by default because the calculations are intensive – but would allow the simulation of flares as short as 12 minutes, more in line with observed flare durations.

5.2.3 Further model runs covering orbital parameters

Our findings in section 4.4 suggested that climate was less sensitive to the chemistry in the case of the 3:2 orbit and the Earth orbit, but this could not be quantified due to the lack of clear comparison cases. Further model runs will maintain the same orbital parameters but switch off the chemistry to allow us to fully understand the feedbacks from chemistry on the climate in these orbits.

Additional orbits could be also simulated. The TRAPPIST-1 planets present an excellent natural test suite, sitting at a few points in the circumstellar habitable zone (Gillon et al., 2017). Whilst many authors have used GCMs to investigate the edges of the circumstellar habitable zone, the use of online, 3D photochemical models has been limited to studies of e.g. early Earth, a snowball Earth, etc. rather than exoplanets. On Earth, small changes in radiative forcing can cause dramatic changes in the climate; these forcings are a major uncertainty in studies of climate change (Collins et al., 2013). A simple simulation of our planet at a range of orbital semi-major axes would allow us to gauge the impact of a small change in radiative input on the atmospheric chemistry and climate.

References

Abe, Y. et al. (2011). "Habitable zone limits for dry planets". In: *Astrobiology* 11 (5), pp. 443–460. DOI: 10.1089/ast.2010.0545.

Allard, F., D. Homeier, and B. Freytag (2012). "Models of very-low-mass stars, brown dwarfs and exoplanets". In: *Philosophical Transactions of the Royal Society A: Mathematical, Physical and Engineering Sciences* 370 (1968), pp. 2765–2777. DOI: 10.1098/rsta.2011.0269. arXiv: 1112.3591 [astro-ph.SR].

Anglada-Escudé, G. et al. (2016). "A terrestrial planet candidate in a temperate orbit around Proxima Centauri". In: *Nature* 536 (7617), pp. 437–440. DOI: 10.1038/nature19106. arXiv: 1609.03449.

Ardaseva, A. et al. (2017). "Lightning chemistry on Earth-like exoplanets". In: *Monthly Notices of the Royal Astronomical Society* 470 (1), pp. 187–196. DOI: 10.1093/mnras/stx1012. arXiv: 1704.07917.

Bailey, R. L. et al. (2014). "IONIZATION IN ATMOSPHERES OF BROWN DWARFS AND EXTRASOLAR PLANETS VI: PROPERTIES OF LARGE-SCALE DISCHARGE EVENTS". In: *The Astrophysical Journal* 784 (1), p. 43. DOI: 10.1088/0004-637X/784/1/43. arXiv: 1312.6789.

Baraffe, I. et al. (2003). "Evolutionary models for cool brown dwarfs and extrasolar giant planets. The case of HD 209458". In: *Astronomy and Astrophysics* 402 (2), pp. 701–712. DOI: 10.1051/0004-6361:20030252. arXiv: 0302293 [astro-ph].

Beamín, J. C. et al. (2014). "Temperature constraints on the coldest brown dwarf known: WISE 0855-0714". en. In: *Astronomy and Astrophysics* 570, p. L8. DOI: 10.1051/0004-6361/201424505.

Bochanski, J. J. et al. (2010). "The Luminosity and Mass Functions of Low-Mass Stars in the Galactic Disk: II. The Field". In: pp. 2679–2699. DOI: 10.1088/0004-6256/139/6/2679. arXiv: 1004.4002.

Borucki, W. J. (2016). "KEPLER Mission: development and overview". In: *Reports on Progress in Physics* 79 (3), p. 036901. DOI: 10.1088/0034-4885/79/3/036901.

Boutle, I. A. et al. (2017). "Exploring the climate of Proxima B with the Met Office Unified Model". In: *Astronomy & Astrophysics* 601, A120. DOI: 10.1051/0004-6361/201630020. arXiv: 1702.08463.

Bowers, R. M. et al. (2012). "Seasonal variability in airborne bacterial communities at a high-elevation site". In: *Atmospheric Environment* 50, pp. 41–49. DOI: 10.1016/j.atmosenv.2012.01.005.

Brown, R. A. (2017). "On the Eccentricity of Proxima b". In: *The Astrophysical Journal* 844 (2), p. 100. DOI: 10.3847/1538-4357/aa621a. arXiv: 1701.04063.

Burrows, A. S. (2014). "Spectra as windows into exoplanet atmospheres". en. In: *Proceedings of the National Academy of Sciences* 111 (35), pp. 12601–12609. DOI: 10.1073/pnas.1304208111.

Chalikov, D. V. et al. (1971). "Numerical experiments on the general circulation of Venus' atmosphere". In: *Tellus* 23 (6), pp. 483–488. DOI: 10.3402/tellusa.v23i6.10530. eprint: https://doi.org/10.3402/tellusa.v23i6.10530.

Charbonneau, D. and D. Deming (2007). "The Dynamics-Based Approach to Studying Terrestrial Exoplanets". In: *Exoplanet Task Force (AAAC)* (April), pp. 1–7. arXiv: 0706.1047.

Charbonneau, D. et al. (2002). "Detection of an Extrasolar Planet Atmosphere". In: *The Astrophysical Journal* 568 (1), pp. 377–384. DOI: 10.1086/338770.

Charlson, R. J. (2001). "ATMOSPHERIC SCIENCE: Reshaping the Theory of Cloud Formation". In: *Science* 292 (5524), pp. 2025–2026. DOI: 10.1126/science.1060096.

Charpinet, S. et al. (2011). "A compact system of small planets around a former red-giant star". In: *Nature* 480 (7378), pp. 496–499. DOI: 10.1038/nature10631.

Chyba, C. F. and C. B. Phillips (2001). "Possible ecosystems and the search for life on Europa". In: *Proceedings of the National Academy of Sciences* 98 (3), pp. 801–804. DOI: 10.1073/pnas.98.3.801.

Clanton, C. and B. S. Gaudi (2016). "CONSTRAINING THE FREQUENCY OF FREE-FLOATING PLANETS FROM A SYNTHESIS OF MICROLENSING, RADIAL VELOCITY, AND DIRECT IMAGING SURVEY RESULTS". In: *The Astrophysical Journal* 834 (1), p. 46. DOI: 10.3847/1538-4357/834/1/46.

Cockell, C. S. (1999). "Life on Venus". en. In: *Planetary and Space Science* 47 (12), pp. 1487–1501. DOI: 10.1016/S0032-0633(99)00036-7.

Collins, M. et al. (2013). "Long-term Climate Change: Projections, Commitments and Irreversibility". In: *Climate Change 2013: The Physical Science Basis. Contribution of Working Group I to the Fifth Assessment Report of the Intergovernmental Panel on Climate Change*, pp. 1029–1136. DOI: 10.1017/CBO9781107415324.024.

Côté, V. et al. (2008). "Microbial and "de novo" transformation of dicarboxylic acids by three airborne fungi". In: *Science of the Total Environment* 390 (2-3), pp. 530–537. DOI: 10.1016/j.scitotenv.2007.10.035.

Courant, R., K. Friedrichs, and H. Lewy (1928). "Über die partiellen Differenzengleichungen der mathematischen Physik". In: *Mathematische Annalen* 100, pp. 32–74. DOI: 10.1007/BF01448839.

Cushing, M. C. et al. (2006). "A Spitzer Infrared Spectrograph (IRS) Spectral Sequence of M, L, and T Dwarfs". In: *The Astrophysical Journal*. DOI: 10.1088/0004-637X/706/1/923. arXiv: 0605639 [astro-ph].

Cushing, M. C. et al. (2011). "The Discovery of Y Dwarfs Using Data from the Wide-field Infrared Survey Explorer (WISE)". In: *The Astrophysical Journal* 743, pp. 50–67. DOI: 10.1088/0004-637X/743/1/50. arXiv: 1108.4678.

Cushing, M. C., J. T. Rayner, and W. D. Vacca (2005). "An Infrared Spectroscopic Sequence of M, L, and T Dwarfs". In: *The Astrophysical Journal* 623 (2), pp. 1115–1140. DOI: 10.1086/428040. arXiv: 0412313 [astro-ph].

Cushing, M. C. et al. (2008). "Atmospheric Parameters of Field L and T Dwarfs1". In: *The Astrophysical Journal* 678 (2), pp. 1372–1395. DOI: 10.1086/526489. arXiv: 0711.0801.

Daniel, T. L. (1981). "Fish Mucus: In situ Measurements of Polymer Drag Reduction". In: *Biological Bulletin* 160 (3), pp. 376–382.

Dartnell, L. R. et al. (2015). "Constraints on a potential aerial biosphere on Venus: I. Cosmic rays". In: *Icarus* 257, pp. 396–405. DOI: http://dx.doi.org/10.1016/j.icarus.2015.05.006.

Davenport, J. et al. (2011). "Drag reduction by air release promotes fast ascent in jumping emperor penguins – a novel study". In: *Mar. Ecol. Prog. Ser.*

Dean, B. and B. Bhushan (2010). "Shark-skin surfaces for fluid-drag reduction in turbulent flow: a review". In: *Philosophical Transactions of the Royal Society of London A: Mathematical, Physical and Engineering Sciences* 368 (1929), pp. 4775–4806. DOI: 10.1098/rsta.2010.0201. eprint: http://rsta.royalsocietypublishing.org/content/368/1929/4775.full.pdf.

Drummond, B. et al. (2018a). "Observable signatures of wind–driven chemistry with a fully consistent three dimensional radiative hydrodynamics model of HD 209458b". In: *The Astrophysical Journal Letters* 855 (2), p. L31. DOI: 10.3847/2041-8213/aab209. arXiv: 1802.09222.

Drummond, B. et al. (2018b). "The effect of metallicity on the atmospheres of exoplanets with fully coupled 3D hydrodynamics, equilibrium chemistry, and radiative transfer". In: pp. 1–19. DOI: 10.1051/0004-6361/201732010. arXiv: 1801.01045.

Faherty, J. K. et al. (2014). "INDICATIONS OF WATER CLOUDS IN THE COLDEST KNOWN BROWN DWARF". In: *The Astrophysical Journal* 793 (1), p. L16. DOI: 10.1088/2041-8205/793/1/L16. arXiv: 1408.4671.

Finney, D. L. et al. (2016). "Response of lightning NO x emissions and ozone production to climate change: Insights from the Atmospheric Chemistry and Climate Model Intercomparison Project". In: *Geophysical Research Letters* 43 (10), pp. 5492–5500. DOI: 10.1002/2016GL068825.

Flato, G. M. (2011). "Earth system models: An overview". In: *Wiley Interdisciplinary Reviews: Climate Change* 2 (6), pp. 783–800. DOI: 10.1002/wcc.148.

Fortes, A. (2000). "Exobiological Implications of a Possible Ammonia–Water Ocean inside Titan". In: *Icarus* 146 (2), pp. 444–452. DOI: 10.1006/icar.2000.6400.

France, O. B. et al. (2013). "Clouds and Aerosols". In: *Climate Change 2013 - The Physical Science Basis*. Ed. by Intergovernmental Panel on Climate Change. Vol. 9781107057. Cambridge: Cambridge University Press, pp. 571–658. DOI: 10.1017/CBO9781107415324.016. arXiv: arXiv:1011.1669v3.

Franks, P. J. S. (2002). "NPZ models of plankton dynamics: Their construction, coupling to physics, and application". In: *Journal of Oceanography* 58, pp. 379–387. DOI: 10.1023/A:1015874028196.

Fujii, Y. et al. (2018). "Exoplanet Biosignatures: Observational Prospects". In: *Astrobiology* 18 (6), pp. 739–778. DOI: 10.1089/ast.2017.1733. arXiv: 1705.07098.

Fuzzi, S., P. Mandrioli, and A. Perfetto (1997). "Fog droplets - An atmospheric source of secondary biological aerosol particles". In: *Atmospheric Environment* 31 (2), pp. 287–290. DOI: 10.1016/1352-2310(96)00160-4.

Gandolfi, I. et al. (2013). "Unravelling the bacterial diversity in the atmosphere". In: *Applied Microbiology and Biotechnology* 97 (11), pp. 4727–4736. DOI: 10.1007/s00253-013-4901-2.

Gilichinsky, D. et al. (2008). "Bacteria in Permafrost". In: *Psychrophiles: from Biodiversity to Biotechnology*. Berlin, Heidelberg: Springer Berlin Heidelberg, pp. 83–102. DOI: 10.1007/978-3-540-74335-4_6.

Gillon, M. et al. (2017). "Seven temperate terrestrial planets around the nearby ultracool dwarf star TRAPPIST-1". In: *Nature* 542 (7642), pp. 456–460. DOI: 10.1038/nature21360. arXiv: 1703.01424.

Godolt, M. et al. (2015). "3D climate modeling of Earth-like extrasolar planets orbiting different types of host stars". In: *Planetary and Space Science* 111, pp. 62–76. DOI: http://dx.doi.org/10.1016/j.pss.2015.03.010.

Greenberg, R. et al. (2000). "Habitability of Europa's crust: The role of tidal-tectonic processes". In: *Journal of Geophysical Research: Planets* 105 (E7), pp. 17551–17562. DOI: 10.1029/1999JE001147.

Haberle, R. M., C. B. Leovy, and J. B. Pollack (1982). "Some effects of global dust storms on the atmospheric circulation of Mars". In: *Icarus* 50 (2), pp. 322–367. DOI: https://doi.org/10.1016/0019-1035(82)90129-4.

Hayashi, C. and T. Nakano (1963). "Evolution of Stars of Small Masses in the Pre-Main-Sequence Stages". In: *Progress of Theoretical Physics* 30 (4), pp. 460–474. DOI: 10.1143/PTP.30.460.

Heller, R. (2017). "Detecting and Characterizing Exomoons and Exorings". In: *Handbook of Exoplanets*. Cham: Springer International Publishing, pp. 1–17. DOI: 10.1007/978-3-319-30648-3_35-1. arXiv: 1807.05136.

Helling, C. and S. Casewell (2014). "Atmospheres of brown dwarfs". In: *The Astronomy and Astrophysics Review* 22 (1), p. 80. DOI: 10.1007/s00159-014-0080-0.

Helling, C. and A. Fomins (2013). "Modelling the formation of atmospheric dust in brown dwarfs and planetary atmospheres". In: *Philosophical Transactions of the Royal Society of London A: Mathematical, Physical and Engineering Sciences* 371 (1994). DOI: 10.1098/rsta.2011.0581. eprint: http://rsta.royalsocietypublishing.org/content/371/1994/20110581.full.pdf.

Helling, C. et al. (2008). "A comparison of chemistry and dust cloud formation in ultracool dwarf model atmospheres". In: *Monthly Notices of the Royal Astronomical Society* 391 (4), pp. 1854–1873. DOI: 10.1111/j.1365-2966.2008.13991.x. eprint: http://mnras.oxfordjournals.org/content/391/4/1854.full.pdf+html.

Heng, K. and P. Kopparla (2012). "On the stability of super-Earth atmospheres". In: *Astrophysical Journal* 754 (1). DOI: 10.1088/0004-637X/754/1/60. arXiv: 1203.1922.

Hill, G. E. (1968). "Grid Telescoping in Numerical Weather Prediction". In: *Journal of Applied Meteorology* 7 (1), pp. 29–38. DOI: 10.1175/1520-0450(1968)007<0029:GTINWP>2.0.CO;2. eprint: https://doi.org/10.1175/1520-0450(1968)007<0029:GTINWP>2.0.CO;2.

Howard, W. S. et al. (2018). "The First Naked-eye Superflare Detected from Proxima Centauri". In: *The Astrophysical Journal* 860 (2), p. L30. DOI: 10.3847/2041-8213/aacaf3. arXiv: 1804.02001.

Hu, R., S. Seager, and W. Bains (2012). "Photochemistry in terrestrial exoplanet atmospheres. I. Photochemistry model and benchmark cases". In: *Astrophysical Journal* 761 (2). DOI: 10.1088/0004-637X/761/2/166. arXiv: arXiv:1210.6885v1.

Irwin, L. N. (2018). "Exotic Forms of Life on Other Worlds". In: *Handbook of Exoplanets*. Cham: Springer International Publishing, pp. 1–13. DOI: 10.1007/978-3-319-30648-3_161-1.

Jacob, D. J. (1999). *Introduction to Atmospheric Chemistry*. ISBN 978-0*691-00185-2. Princeton University Press.

Johnson, L. et al. (2006). "Characterization of vaccinia virus particles using microscale silicon cantilever resonators and atomic force microscopy". In: *Sensors and Actuators B: Chemical* 115 (1), pp. 189–197. DOI: 10.1016/j.snb.2005.08.047.

Jones, A. M. and R. M. Harrison (2004). "The effects of meteorological factors on atmospheric bioaerosol concentrations—a review". In: *Science of The Total Environment* 326 (1–3), pp. 151–180. DOI: http://dx.doi.org/10.1016/j.scitotenv.2003.11.021.

Joshi, M., R. Haberle, and R. Reynolds (1997). "Simulations of the Atmospheres of Synchronously Rotating Terrestrial Planets Orbiting M Dwarfs: Conditions for Atmospheric Collapse and the Implications for Habitability". In: *Icarus* 129 (2), pp. 450–465. DOI: 10.1006/icar.1997.5793.

Kálnay de Rivas, E. (1975). "Further Numerical Calculations of the Circulation of the Atmosphere of Venus". In: *Journal of the Atmospheric Sciences* 32 (6), pp. 1017–1024. DOI: 10.1175/1520-0469(1975)032<1017:FNCOTC>2.0.CO;2. eprint: https://doi.org/10.1175/1520-0469(1975)032<1017:FNCOTC>2.0.CO;2.

Kaltenegger, L. (2017). "How to Characterize Habitable Worlds and Signs of Life". In: *Annual Review of Astronomy and Astrophysics* 55 (1), pp. 433–485. DOI: 10.1146/annurev-astro-082214-122238.

Kaspi, Y. and A. P. Showman (2015). "ATMOSPHERIC DYNAMICS OF TERRESTRIAL EXOPLANETS OVER A WIDE RANGE OF ORBITAL AND ATMOSPHERIC PARAMETERS". In: *The Astrophysical Journal* 804 (1), p. 60. DOI: 10.1088/0004-637X/804/1/60. arXiv: 1407.6349.

Kasting, J. F. (1988). "Runaway and moist greenhouse atmospheres and the evolution of Earth and Venus". In: *Icarus* 74 (3), pp. 472–494. DOI: 10.1016/0019-1035(88)90116-9.

Kasting, J. F., D. P. Whitmire, and R. T. Reynolds (1993). "Habitable Zones around Main Sequence Stars". In: *Icarus* 101 (1), pp. 108–128. DOI: http://dx.doi.org/10.1006/icar.1993.1010.

Kirkpatrick, J. D. et al. (1999). "Dwarfs Cooler than "M": The Definition of Spectral Type "L" Using Discoveries from the 2 Micron All Sky Survey (2MASS)". In: *The Astrophysical Journal* 519 (2), pp. 802–833. DOI: 10.1086/307414.

Kirkpatrick, J. D. et al. (2012). "FURTHER DEFINING SPECTRAL TYPE "Y" AND EXPLORING THE LOW-MASS END OF THE FIELD BROWN DWARF MASS FUNCTION". In: *The Astrophysical Journal* 753 (2), p. 156. DOI: 10.1088/0004-637X/753/2/156. arXiv: 1205.2122.

Koop, T. et al. (2000). "Water activity as the determinant for homogeneous ice nucleation in aqueous solutions". In: *Nature* 406 (6796), pp. 611–614.

Kopytova, T. G. et al. (2014). "DEEP z -BAND OBSERVATIONS OF THE COOLEST Y DWARF". In: *The Astrophysical Journal* 797, p. 3. DOI: 10.1088/0004-637X/797/1/3. arXiv: 1410.5649.

Kumar, S. S. (1963). "THE STRUCTURE OF STARS OF VERY LOW MASS". In: *The Astrophysical Journal* 137, p. 1121. DOI: 10.1086/147589.

Lawson, R. P. and A. Gettelman (2014). "Impact of Antarctic mixed-phase clouds on climate". In: *Proceedings of the National Academy of Sciences* 111 (51), pp. 18156–18161. DOI: 10.1073/pnas.1418197111. eprint: http://www.pnas.org/content/111/51/18156.full.pdf.

Lebonnois, S., N. Sugimoto, and G. Gilli (2016). "Wave analysis in the atmosphere of Venus below 100-km altitude, simulated by the LMD Venus GCM". In: *Icarus* 278, pp. 38–51. DOI: 10.1016/j.icarus.2016.06.004.

Leconte, J. et al. (2013). "Increased insolation threshold for runaway greenhouse processes on Earth-like planets." In: *Nature* 504 (7479), pp. 268–71. DOI: 10.1038/nature12827. arXiv: arXiv:1312.3337v1.

Leovy, C. and Y. Mintz (1969). "Numerical Simulation of the Atmospheric Circulation and Climate of Mars". In: *Journal of the Atmospheric Sciences* 26 (6), pp. 1167–1190. DOI: 10.1175/1520-0469(1969)026<1167:NSOTAC>2.0.CO;2. eprint: https://doi.org/10.1175/1520-0469(1969)026<1167:NSOTAC>2.0.CO;2.

Lewis, N. T. et al. (2018). "The influence of a sub-stellar continent on the climate of a tidally-locked exoplanet". In: *The Astrophysical Journal* 854 (2), p. 171. DOI: 10.3847/1538-4357/aaad0a. arXiv: 1802.00378.

Lighthart, B. (1997). "The ecology of bacteria in the alfresco atmosphere". In: *FEMS Microbiology Ecology* 23 (4), pp. 263–274. DOI: 10.1016/S0168-6496(97)00036-6.

Lighthart, B. and B. T. Shaffer (1995). "Viable bacterial aerosol particle size distributions in the midsummer atmosphere at an isolated location in the high desert chaparral". In: *Aerobiologia* 11 (1), pp. 19–25. DOI: 10.1007/BF02136140.

Lissauer, J. J. et al. (2011). "A closely packed system of low-mass, low-density planets transiting Kepler-11". In: *Nature* 470 (7332), pp. 53–58. DOI: 10.1038/nature09760. arXiv: 1008.4393.

Loewe, K. et al. (2016). "Modelling micro- and macrophysical contributors to the dissipation of an Arctic mixed-phase cloud during the Arctic Summer Cloud Ocean Study (ASCOS)". In: *Atmospheric Chemistry and Physics Discussions* 2016, pp. 1–22. DOI: 10.5194/acp-2016-917.

Lorenz, E. N. (1963). *Deterministic Nonperiodic Flow*. DOI: 10.1175/1520-0469(1963)020<0130:DNF>2.0.CO;2. arXiv: NIHMS150003.

Luhman, K. L. (2014). "DISCOVERY OF A ∼250 K BROWN DWARF AT 2 pc FROM THE SUN". In: *The Astrophysical Journal* 786 (2), p. L18. DOI: 10.1088/2041-8205/786/2/L18. arXiv: 1404.6501.

Madhusudhan, N., D. Apai, and S. Gandhi (2016). "Atmospheric compositions of three brown dwarfs and implications for their formation conditions". In: *Submitted to ApJ*.

Manabe, S. and K. Bryan (1969). "Climate Calculations with a Combined Ocean-Atmosphere Model". In: *Journal of the Atmospheric Sciences* 26 (4), pp. 786–789. DOI: 10.1175/1520-0469(1969)026<0786:CCWACO>2.0.CO;2. eprint: https://doi.org/10.1175/1520-0469(1969)026<0786:CCWACO>2.0.CO;2.

Marley, M. and T. Robinson (2015). "On the Cool Side: Modeling the Atmospheres of Brown Dwarfs and Giant Planets". In: *Annual Review of Astronomy and Astrophysics* 53 (1), pp. 279–323. DOI: 10.1146/annurev-astro-082214-122522. eprint: https://doi.org/10.1146/annurev-astro-082214-122522.

Mayne, N. J. et al. (2014). "The unified model , a fully-compressible , non-hydrostatic , deep atmosphere global circulation model , applied to hot Jupiters ENDGame for a HD 209458b test case". In: *Astronomy and Astrophysics* 561 (A1), pp. 1–24. DOI: 10.1051/0004-6361/201322174.

Mayne, N. et al. (2013). "Using the UM dynamical cores to reproduce idealised 3D flows". In: *Geoscientific Model Development Discussions* 6, pp. 3681–3741. DOI: 10.5194/gmdd-6-3681-2013. arXiv: 1310.6041.

Mayor, M. and D. Queloz (1995). *A Jupiter-mass companion to a solar-type star*. DOI: 10.1038/378355a0.

McKay, C. P. (2014). "Requirements and limits for life in the context of exoplanets". en. In: *Proceedings of the National Academy of Sciences* 111 (35), pp. 12628–12633. DOI: 10.1073/pnas.1304212111.

McKenzie, R. L. et al. (2011). "Ozone depletion and climate change: impacts on UV radiation". In: *Photochem. Photobiol. Sci.* 10 (2), pp. 182–198. DOI: 10.1039/C0PP90034F.

Md, A. et al. (2015). "Drag forice on micron-sized object with different surface morphologies in a flow with a small Reynolds number". In: *Polymer Journal*.

Meadows, V. S. and R. K. Barnes (2018). "Factors Affecting Exoplanet Habitability". In: *Handbook of Exoplanets*. Cham: Springer International Publishing, pp. 1–24. DOI: 10.1007/978-3-319-30648-3_57-1.

Meadows, V. S. et al. (2018). "The Habitability of Proxima Centauri b: Environmental States and Observational Discriminants". In: *Astrobiology* 18 (2), pp. 133–189. DOI: 10.1089/ast.2016.1589.

Mendonça, J. M. et al. (2018). "Three-Dimensional Circulation Driving Chemical Disequilibrium in WASP-43b". In: pp. 1–16. arXiv: 1808.00501.

Menou, K. and E. Rauscher (2009). "ATMOSPHERIC CIRCULATION OF HOT JUPITERS: A SHALLOW THREE-DIMENSIONAL MODEL". In: *The Astrophysical Journal* 700 (1), pp. 887–897. DOI: 10.1088/0004-637X/700/1/887. arXiv: arXiv:0809.1671v2.

Miller-Ricci Kempton, E., K. Zahnle, and J. J. Fortney (2012). "The atmospheric chemistry of GJ 1214b: Photochemistry and clouds". In: *Astrophysical Journal* 745 (1). DOI: 10.1088/0004-637X/745/1/3. arXiv: 1104.5477.

Morley, C. V. et al. (2014a). "SPECTRAL VARIABILITY FROM THE PATCHY ATMOSPHERES OF T AND Y DWARFS". In: *The Astrophysical Journal* 789 (1), p. L14. DOI: 10.1088/2041-8205/789/1/L14.

Morley, C. V. et al. (2014b). "WATER CLOUDS IN Y DWARFS AND EXOPLANETS". In: *The Astrophysical Journal* 787 (1), p. 78. DOI: 10.1088/0004-637X/787/1/78.

Morrison, H. et al. (2012). "Resilience of persistent Arctic mixed-phase clouds". In: *Nature Geosci* 5 (1), pp. 11–17.

Morton, T. D. et al. (2016). "False positive probabilties for all Kepler Objects of Interest: 1284 newly validated planets and 428 likely false positives". In: *The Astrophysical Journal* 822 (2), pp. 1–15. DOI: 10.3847/0004-637X/822/2/86. arXiv: 1605.02825.

Moses, J. I. (2014). "Chemical kinetics on extrasolar planets". In: *Philosophical Transactions of the Royal Society A: Mathematical, Physical and Engineering Sciences* 372 (2014), pp. 20130073–20130073. DOI: 10.1098/rsta.2013.0073.

Muñoz Caro, G. M. et al. (2002). "Amino acids from ultraviolet irradiation of interstellar ice analogues". In: *Nature* 416 (6879), pp. 403–406. DOI: 10.1038/416403a.

Nakajima, T. et al. (1995). *Discovery of a cool brown dwarf*. DOI: 10.1038/378463a0.

O'Malley-James, J. T. and L. Kaltenegger (2017). "UV surface habitability of the TRAPPIST-1 system". In: *Monthly Notices of the Royal Astronomical Society: Letters* 469 (1), pp. L26–L30. DOI: 10.1093/mnrasl/slx047. arXiv: 1702.06936.

Palmer, T. N. (2012). "Towards the probabilistic Earth-system simulator: a vision for the future of climate and weather prediction". In: *Quarterly Journal of the Royal Meteorological Society* 138 (665), pp. 841–861. DOI: 10.1002/qj.1923. arXiv: arXiv:1208.5721.

Paradise, A. and K. Menou (2017). "GCM Simulations of Unstable Climates in the Habitable Zone". In: *The Astrophysical Journal* 848 (1), p. 33. DOI: 10.3847/1538-4357/aa8b1c. arXiv: 1704.04535.

Parkinson, C. D. et al. (2008). "Habitability of Enceladus: Planetary Conditions for Life". In: *Origins of Life and Evolution of Biospheres* 38 (4), pp. 355–369. DOI: 10.1007/s11084-008-9135-4.

Phillips, N. A. (1956). "The general circulation of the atmosphere: A numerical experiment". In: *Quarterly Journal of the Royal Meteorological Society* 82 (352), pp. 123–164. DOI: 10.1002/qj.49708235202. eprint: https://rmets.onlinelibrary.wiley.com/doi/pdf/10.1002/qj.49708235202.

Pierrehumbert, R. T. (1995). "Thermostats, Radiator Fins, and the Local Runaway Greenhouse". In: *Journal of the Atmospheric Sciences* 52 (10), pp. 1784–1806. DOI: 10.1175/1520-0469(1995)052<1784:TRFATL>2.0.CO;2.

Postberg, F. et al. (2011). "A salt-water reservoir as the source of a compositionally stratified plume on Enceladus". In: *Nature* 474 (7353), pp. 620–622. DOI: 10.1038/nature10175.

Proedrou, E. and K. Hocke (2016). "Characterising the three-dimensional ozone distribution of a tidally locked Earth-like planet". In: *Earth, Planets and Space* 68 (1), p. 96. DOI: 10.1186/s40623-016-0461-x.

Rajpurohit, A. S. et al. (2013). "The effective temperature scale of M dwarfs". In: *Astronomy & Astrophysics* 556, A15. DOI: 10.1051/0004-6361/201321346. arXiv: 1304.4072.

Rebolo, R. et al. (1996). "Brown Dwarfs in the Pleiades Cluster Confirmed by the Lithium Test". In: *The Astrophysical Journal* 469, pp. L53–L56. DOI: 10.1086/310263. arXiv: 9607002 [astro-ph].

Rogers, R. R. and M. K. Yau (1995). *A short course in cloud physics*. ISBC 0-7506-3215-1. Elsevier.

Sadourny, R., A. Arakawa, and Y. Mintz (1968). "INTEGRATION OF THE NONDIVERGENT BAROTROPIC VORTICITY EQUATION WITH AN ICOSAHEDRAL-HEXAGONAL GRID FOR THE SPHERE". In: *Monthly Weather Review* 96 (6), pp. 351–356. DOI: 10.1175/1520-0493(1968)096<0351:IOTNBV>2.0.CO;2. eprint: https://doi.org/10.1175/1520-0493(1968)096<0351:IOTNBV>2.0.CO;2.

Sagan, C. and E. E. Salpeter (1976). "Particles, environments, and possible ecologies in the Jovian atmosphere". In: *The Astrophysical Journal Supplement Series* 32, pp. 737–755. DOI: 10.1086/190414.

Said, S. E. and D. A. Dickey (1984). "Testing for unit roots in autoregressive-moving average models of unknown order". In: *Biometrika* 71 (3), pp. 599–607. DOI: 10.1093/biomet/71.3.599. eprint: http://biomet.oxfordjournals.org/content/71/3/599.full.pdf+html.

Sattler, B., H. Puxbaum, and R. Psenner (2001). "Bacterial growth in supercooled cloud droplets". In: *Geophysical Research Letters* 28 (2), p. 239. DOI: 10.1029/2000GL011684.

Saur, J. et al. (2015). "The search for a subsurface ocean in Ganymede with Hubble Space Telescope observations of its auroral ovals". In: *Journal of Geophysical Research: Space Physics* 120 (3), pp. 1715–1737. DOI: 10.1002/2014JA020778.

Schmidt, B. E. et al. (2011). "Active formation of 'chaos terrain' over shallow subsurface water on Europa". In: *Nature* 479 (7374), pp. 502–505. DOI: 10.1038/nature10608.

Schulze-Makuch, D. et al. (2004). "A sulfur-based survival strategy for putative phototrophic life in the venusian atmosphere." In: *Astrobiology* 4 (1), pp. 11–18. DOI: 10.1089/153110704773600203.

Schwieterman, E. W. et al. (2018). "Exoplanet Biosignatures: A Review of Remotely Detectable Signs of Life". In: *Astrobiology* 18 (6), pp. 663–708. DOI: 10.1089/ast.2017.1729. arXiv: 1705.05791.

Seager, S. (2013). "Exoplanet Habitability". In: *Science* 340 (6132), pp. 577–581. DOI: 10.1126/science.1232226.

— (2014). "The future of spectroscopic life detection on exoplanets". en. In: *Proceedings of the National Academy of Sciences* 111 (35), pp. 12634–12640. DOI: 10.1073/pnas.1304213111.

Segura, A. et al. (2003). "Ozone concentrations and ultraviolet fluxes on Earth-like planets around other stars". In: *Astrobiology* 3 (4).

Segura, A. et al. (2010). "The Effect of a Strong Stellar Flare on the Atmospheric Chemistry of an Earth-like Planet Orbiting an M Dwarf". In: *Astrobiology* 10 (7), pp. 751–771. DOI: 10.1089/ast.2009.0376. arXiv: 1006.0022.

Seinfeld and Pandis (2006). *Atmospheric Chemistry and Physics: From Air Pollution to Climate Change, 2nd Edition*. Wiley.

Shields, A. L., S. Ballard, and J. A. Johnson (2016). "The habitability of planets orbiting M-dwarf stars". In: *Physics Reports* 663, pp. 1–38. DOI: 10.1016/j.physrep.2016.10.003. arXiv: 1610.05765.

Shields, A. L. et al. (2013). "The Effect of Host Star Spectral Energy Distribution and Ice-Albedo Feedback on the Climate of Extrasolar Planets". In: *Astrobiology* 13 (8), pp. 715–739. DOI: 10.1089/ast.2012.0961. arXiv: 1305.6926.

Showman, A. P., J. Y.-K. Cho, and K. Menou (2009). "Atmospheric Circulation of Exoplanets". In: arXiv: 0911.3170.

Showman, A. P. and Y. Kaspi (2013). "Atmospheric Dynamics of Brown Dwarfs and Directly Imaged Giant Planets". In: *The Astrophysical Journal* 776 (2), p. 85. DOI: 10.1088/0004-637X/776/2/85.

Showman, A. P. and L. M. Polvani (2011). "EQUATORIAL SUPERROTATION ON TIDALLY LOCKED EXOPLANETS". In: *The Astrophysical Journal* 738 (1), p. 71. DOI: 10.1088/0004-637X/738/1/71. arXiv: 1103.3101.

Showman, A. P. et al. (2013). "Atmospheric Circulation of Terrestrial Exoplanets". In: DOI: 10.2458/azu_uapress_9780816530595-ch12. arXiv: 1306.2418.

Silberman, I. (1954). "PLANETARY WAVES IN THE ATMOSPHERE". In: *Journal of Meteorology* 11 (1), pp. 27–34. DOI: 10.1175/1520-0469(1954)011<0027:PWITA>2.0.CO;2. eprint: https://doi.org/10.1175/1520-0469(1954)011<0027:PWITA>2.0.CO;2.

Skemer, A. J. et al. (2016). "THE FIRST SPECTRUM OF THE COLDEST BROWN DWARF". In: *The Astrophysical Journal* 826 (2), p. L17. DOI: 10.3847/2041-8205/826/2/L17. arXiv: arXiv:1605.04902v1.

Stark, C. R. et al. (2014). "Electrostatic activation of prebiotic chemistry in substellar atmospheres". In: *International Journal of Astrobiology* 13 (02), pp. 165–172. DOI: 10.1017/S1473550413000475.

Tarter, J. C. et al. (2007). "A Reappraisal of The Habitability of Planets around M Dwarf Stars". In: *Astrobiology* 7 (1), pp. 30–65. DOI: 10.1089/ast.2006.0124. arXiv: 0609799 [astro-ph].

Thomas, P. et al. (2016). "Enceladus's measured physical libration requires a global subsurface ocean". In: *Icarus* 264, pp. 37–47. DOI: 10.1016/j.icarus.2015.08.037. arXiv: 1509.07555.

Thompson, S. E. et al. (2018). "Planetary Candidates Observed by Kepler . VIII. A Fully Automated Catalog with Measured Completeness and Reliability Based on Data Release 25". In: *The Astrophysical Journal Supplement Series* 235 (2), p. 38. DOI: 10.3847/1538-4365/aab4f9. arXiv: 1710.06758.

Tilley, M. A. et al. (2017). "Modeling Repeated M-dwarf Flaring at an Earth-like Planet in the Habitable Zone: I. Atmospheric Effects for an Unmagnetized Planet". In: pp. 1–65. arXiv: 1711.08484.

Tinney, C. G. et al. (2014). "THE LUMINOSITIES OF THE COLDEST BROWN DWARFS". In: *The Astrophysical Journal* 796 (1), p. 39. DOI: 10.1088/0004-637X/796/1/39.

Tompkins, A. M. (2000). "The Impact of Dimensionality on Long-Term Cloud-Resolving Model Simulations". In: *Monthly Weather Review* 128 (5), pp. 1521–1535. DOI: 10.1175/1520-0493(2000)128<1521:TIODOL>2.0.CO;2.

Tsuji, T. (2005). "Dust in the Photospheric Environment. III. A Fundamental Element in the Characterization of Ultracool Dwarfs". en. In: *The Astrophysical Journal* 621 (2), pp. 1033–1048. DOI: 10.1086/427747.

Turbet, M. et al. (2017). "3D modelling of the climatic impact of outflow channel formation events on early Mars". In: *Icarus* 288, pp. 10–36. DOI: 10.1016/j.icarus.2017.01.024. arXiv: 1701.07886.

Vance, S. et al. (2014). "Ganymede's internal structure including thermodynamics of magnesium sulfate oceans in contact with ice". In: *Planetary and Space Science* 96, pp. 62–70. DOI: 10.1016/j.pss.2014.03.011.

Venot, O. and M. Agúndez (2015). "Chemical modeling of exoplanet atmospheres". In: *Experimental Astronomy* 40 (2-3), pp. 469–480. DOI: 10.1007/s10686-014-9406-1. arXiv: 1406.6566.

Welsh, W. F. and J. A. Orosz (2017). "Two Suns in the Sky: The Kepler Circumbinary Planets". In: *Handbook of Exoplanets*. Ed. by H. J. Deeg and J. A. Belmonte. Cham: Springer International Publishing, pp. 1–21. DOI: 10.1007/978-3-319-30648-3_34-1. arXiv: 1807.05136.

Williams, G. P. and J. L. Holloway (1982). "The range and unity of planetary circulations". In: *Nature* 297 (5864), pp. 295–299. DOI: 10.1038/297295a0.

Witte, S. et al. (2011). "Dust in brown dwarfs and extra-solar planets". en. In: *Astronomy and Astrophysics* 529, A44. DOI: 10.1051/0004-6361/201014105.

WMO (2007). "Scientific Assessment of Ozone Depletion: 2006". In: *Global Ozone Research and Monitoring Project - Report No. 50*, p. 572.

Wolf, E. T. et al. (2017). "Constraints on Climate and Habitability for Earth-like Exoplanets Determined from a General Circulation Model". In: *The Astrophysical Journal* 837 (2), p. 107. DOI: 10.3847/1538-4357/aa5ffc. arXiv: 1702.03315.

Wölk, J. and R. Strey (2001). "Homogeneous Nucleation of H2O and D2O in Comparison: The Isotope Effect". In: *The Journal of Physical Chemistry B* 105 (47), pp. 11683–11701. DOI: 10.1021/jp0115805. eprint: http://dx.doi.org/10.1021/jp0115805.

Wolszczan, A. and D. A. Frail (1992). "A planetary system around the millisecond pulsar PSR1257 + 12". In: *Nature* 355 (6356), pp. 145–147. DOI: 10.1038/355145a0.

Womack, A. M., B. J. M. Bohannan, and J. L. Green (2010). "Biodiversity and biogeography of the atmosphere". In: *Philosophical transactions of the Royal Society of London. Series B, Biological sciences* 365 (1558), pp. 3645–3653. DOI: 10.1098/rstb.2010.0283.

Yang, J. and D. S. Abbot (2014). "A LOW-ORDER MODEL OF WATER VAPOR, CLOUDS, AND THERMAL EMISSION FOR TIDALLY LOCKED TERRESTRIAL PLANETS". In: *The Astrophysical Journal* 784 (2), p. 155. DOI: 10.1088/0004-637X/784/2/155. arXiv: 1403.0905.

Yang, J., N. B. Cowan, and D. S. Abbot (2013). "Stabilizing Cloud Feedback Dramatically Expands the Habitable Zone of Tidally Locked Planets". In: *The Astrophysical Journal* 771 (2), p. L45. DOI: 10.1088/2041-8205/771/2/L45.

Yang, J. et al. (2014). "STRONG DEPENDENCE OF THE INNER EDGE OF THE HABITABLE ZONE ON PLANETARY ROTATION RATE". In: *The Astrophysical Journal* 787 (1), p. L2. DOI: 10.1088/2041-8205/787/1/L2.

Yates, J. S. et al. (2017). "Atmospheric Habitable Zones in Y Dwarf Atmospheres". In: *The Astrophysical Journal* 836 (2), p. 184. DOI: 10.3847/1538-4357/836/2/184.

Young, R. E. and J. B. Pollack (1977). "A Three–Dimensional Model of Dynamical Processes in the Venus Atmosphere". In: *Journal of the Atmospheric Sciences* 34 (9), pp. 1315–1351. DOI: 10.1175/1520-0469(1977)034<1315:ATMODP>2.0.CO;2. eprint: https://doi.org/10.1175/1520-0469(1977)034<1315:ATMODP>2.0.CO;2.

Zahnle, K. et al. (2009). "Atmospheric sulfur photochemistry on hot jupiters". In: *Astrophysical Journal* 701 (1 PART 2), pp. 20–24. DOI: 10.1088/0004-637X/701/1/L20. arXiv: 0903.1663.